Mechanical responses of laser ablated axons of neuronal cells

by

Ashish Kumar Mishra

A thesis submitted to the Jawaharlal Nehru University for the degree of DOCTOR OF PHILOSOPHY

June 2025

DECLARATION

I, Ashish Kumar Mishra, hereby declare that this thesis is composed independently by me at Raman Research Institute, Bangalore, India, under the supervision of Prof. Pramod A Pullarkat. The subject matter presented in this thesis has not previously formed the basis of the award of any degree, diploma, associateship, fellowship or any other similar title in any other University. I also declare that I have run it through the Drillbit plagiarism software.

Prof. Pramod A Pullarkat
Raman Research Institute

Ashish Kumar Mishra
Raman Research Institute

CERTIFICATE

This is to certify that the thesis entitled **Mechanical responses of laser ablated axons of neuronal cells** submitted by Ashish Kumar Mishra for the award of the degree of DOCTOR OF PHILOSOPHY of Jawaharlal Nehru University is his original work. This has not been published or submitted to any other University for any other degree or diploma.

Prof. Tarun Souradeep	Prof. Pramod A Pullarkat
Director	Thesis Supervisor
Raman Research Institute	Raman Research Institute

To my family

ACKNOWLEDGEMENTS

The PhD experience has included a variety of challenges and successes, but numerous individuals have significantly contributed to making this thesis possible. I would like to take this moment to thank and express my gratitude to them.

I want to express my sincere thanks to my PhD supervisor, Prof. Pramod Pullarkat, who led me into the fascinating field of biophysics. He showed extraordinary patience over these years. Without his constant encouragement and support, this thesis would not have come into existence. I am thankful for the freedom he gave me as well. I really appreciate his kindness and humility.

I am grateful to Prof. V. A. Raghunathan and Prof. Gautam Menon for regularly reviewing my progress and providing valuable feedback every year. I also appreciate the discussions and insights from Prof. Ranjini Bandyopadhyay, Dr. Arun Roy, Dr. Gautam Soni and Dr. Sayantan Majumdaar. Their guidance has been invaluable.

I sincerely thank my collaborator, Prof. Aurnab Ghose, for his valuable discussions and support. I also want to acknowledge Jaisha, Nishita, and Serene for their support during the early days in the lab, teaching me dissection and cell culture and helping me understand the protocols used in the lab.

I extend my thanks to our group secretaries, Radhakrishna, Amudha, Chaitanya, Gayathri and the staff members Ishaq, Murali, Vasudha,

and Raja for their support. I am also grateful to the RRI Administration for handling the official and formal procedures throughout my time here. I also appreciate C.S.R. Murthy, Naresh, Vidya, Radha, Shailaja, Harini and Marisa for their assistance.

My heartfelt thanks to Ibrahim, Anand, and others from the mechanical workshop for their assistance in fabricating parts useful for my experimental setups. I am also grateful to Yatheendran for his assistance with confocal microscopy. I thank Rishin and others from the electronics workshop for their technical expertise.

I deeply appreciate the support of the library staff, especially Meera, Manjunath, and Nagaraj. I also thank the computer department members, Jacob, Sridhar, and others, for their technical assistance. My gratitude extends to the Purchase and Accounts sections, as well as GB Suresh, Sachin, Muneeswaran, and the civil and electrical department staff for their help.

I feel fortunate to have had such wonderful lab mates. A special thanks to Arsalan for the tracking code, to Sukhveer for his friendship, support, and wonderful discussions on various topics, and to Pooja for helping me with EB3 experiments. I am also thankful to previous as well as present lab members, including Sushil, Suriya, Prashanti, Khitija, Abhigyaan, Sayooj, Praveen, Madhu, Rahul, Divyang, Binsha, Hari, Deepak, Preteesh, Antarang and Gayathri for helping me.

I appreciate the engaging discussions and fun moments shared with Vishnu, Anand, Pradosh, Chandeshawar, Rajkumar, Dipak Patra, Swarnak, Vaibhav, Makrand, Susovan and Sayantan. My gratitude also goes to Mari, Swami, Sreeja, Subhodeep, Raj Prince, and Irla for various help.

I would like to acknowledge my teachers, Diwakar Panday, Narendra Jaisawal and Ramesh Chandra, for their encouragement and inspiration.

I am grateful to my dear friends Abhishek, Amit, Khemu and Dheeraj for their unconditional support and friendship. I also appreciate the encouragement from Deepak, Brijesh and Priyanka.

I also thank the RRI medical facility and doctors, including Dr Baliga, Dr Prasaad and Dr Archana. I also extend my appreciation to Nurses R. Shanthamma and Preethi H.P.

Lastly, I want to thank my late father for his love, blessings, and encouragement. I am forever grateful to my mother, brother-in-law, and my wife Pooja for their endless support and love. I also appreciate all my friends and extended family who have stood by me throughout this journey.

Ashish Kumar Mishra
Bangalore
June, 2025

SYNOPSIS

Introduction

Neurons, the cells that form the nervous system, are unique in their morphology, functionality and composition. Typically, a protrusion known as an axon grows on one side of an initially spherical cell body (soma), and other regions develop branched extensions called dendrites. In the case of humans, axons can extend from a few millimetres to about a meter in length (from the spinal cord to the toe) and about a micron in diameter. They maintain their shape and integrity over such long ranges to affect signal transmission throughout their lifetime. This is aided by a network of cytoskeletal components along with motor proteins and various organelles. During development, axons and dendrites grow via the action of a palm-like motile structure at their extremities. This structure called the growth cone, generates filopodia and lamellipodia like most motile eukaryotic cells. The axonal cytoskeleton has mainly three types of components–microtubules, actin filaments and neurofilaments[1][2]. All cytoskeletal components play a role in maintaining axons' stability. Axons are polarized structures in terms of function and structure, established and maintained by cytoskeletal components. Any breakage or injury to axons results in disruption and loss of cytoskeletal components, leading to obstacles to various neuronal processes that help cells maintain homeostasis. The loss of continuity in axons affects transport and signal transmission as well as which is a

known cause of many neurodegenerative diseases. Along with neurogenerative diseases, injury may lead to discontinuity in the axonal cytoskeleton. So, it is important to understand how cytoskeletal components respond after neuronal injury.

Neuronal cells obtained from 8—9 days of chick embryos and grown in culture for 4 days are used for the experiments. Using a laser ablation setup, we try to mimic axonal injury by ablating axons either fully or partially. Full ablation produces two separate axonal segments, whereas partial ablation damages the cytoskeleton while keeping the membrane intact. For both methods, the axons are ablated at the mid-point. Depending on the ablation method, different kinds of retraction responses are observed. For the full ablation method, axonal segments exhibit retraction and buckling. In the partial ablation, materials inside the axon retract towards the axonal extremities. Here, we have studied these dynamics by measuring the retraction responses in the presence of various pharmacological agents. Imaging of axons or their cytoskeletal components after ablation is performed using a phase contrast or fluorescence microscope system.

Apart from injury-related atrophy, axons also undergo frequent retraction events during development in order to prune unwanted branches. To check the response under similar conditions, and also to check if the retraction process is dependent on the method of inducing it, we also tried inducing retraction by detaching the axonal tip from

the substrate. This was done using a micropipette to locally apply Trypsin—an adhesion destabilising enzyme—to the growth cone alone.

The research work presented in this thesis is divided broadly into two parts:
(i) Investigation of laser-induced axonal retraction responses in the presence of various pharmacological agents
(ii) Resealing of partially ablated axons via recovery of cytoskeletal components in calcium-chelated media

Investigation of laser-induced axonal retraction responses in the presence of various pharmacological agents

The axonal cytoskeleton shows responses when an injury perturbs axons. Previous studies have shown that when axons are cut using a needle or AFM tip, or using a laser, they retract and show different responses [3][4]. However, how the retraction process is affected by the stability of various cytoskeletal components is not well understood. In this part of the thesis, we have investigated the role of various cytoskeletal components and myosin motor protein in axonal retraction when axons are treated with cytoskeleton stabilizing and destabilizing drugs. The Laser ablation setup is used to ablate the axons fully and partially to see the retraction responses.

The Laser ablation setup

The home-built laser ablation setup consists of a high-energy, picosecond, UV-pulsed laser, a confocal microscope, a polarizer, a quarter-wave plate and a beam expander. The UV-pulsed laser is controlled using a trigger to deliver a single shot to a sample, and a computer-controlled function generator is used to fire multiple pulses. The polarizer and quarter wave plate are used together as an intensity attenuator and optical isolator. The Beam expander is used to expand the laser beam to fill the back aperture of the microscope's objective lens. The laser beam is directed into the side port of an inverted microscope using steering mirrors. A dichroic plate is used to reflect the laser beam to sample and transmit the imaging light. The laser beam is focused on the axon using a microscope objective for ablation experiments. The setup can be used to do ablation experiments on various cell types while simultaneously imaging the cells using confocal or phase contrast microscopy methods. The setup is characterised using various methods to get axonal ablation at minimum energy.

Retraction responses of Axons after full and partial ablation

The laser ablation setup is used to ablate the straight segment of the axon pinned down to the substrate at the two ends. After full ablation, axons split into two segments and retract towards the cell body and growth cone. But in partial ablation, the axonal membrane remains intact but all intracellular components retract from

the ablation point towards fixed points. The retraction responses of axonal segments are observed after treating the cells with various pharmacological agents that perturb specific cytoskeletal components by destabilizing or stabilising them. The contour length of the retracting axonal segments is calculated as a function of time. The contour lengths for different treatments are compared to evaluate the role of each component in the retraction dynamics.

Trypsin induced axonal retraction response and comparison with full ablated control axons

The ablation of axons using a pulsed laser at the midpoint of the axons, along with their retraction responses, is explained in the earlier section. We have used an invasive method to induce retraction. So, it would be interesting to check what retraction responses will be when a noninvasive method is used to induce retraction. Also, it shows that the retraction responses are independent of the method used to induce injury. It is also interesting to compare the retraction responses by both methods because axons show retraction dynamics in both cases (laser ablation and trypsin). We induced retraction by detaching the growth cone using trypsin to see the response of the retracting axon in normal culture. Here, cells are grown in culture for 2 days and are used for the experiment. We have analysed the contour length of retracting axons as a function of time. Comparing the contour length data for both cases, we found that the trypsin-induced retraction responses are slower than the laser-induced responses of axonal segments.

Imaging of actin and microtubules in retracting axons

The responses of retracting axonal segments have been seen using various treatments as explained in the earlier section. However, it is still unclear how microtubules and actin respond during retraction. The microtubule or actin filaments may depolymerise or slide or do both during axonal retraction. To investigate this, we used fluorescent probes to image of actin and microtubules during the retraction process.

Resealing of axons in calcium-chelated media after partial ablation

After partial ablation, the axonal segments continuously retract to their fixed extremities in normal culture. But when similar experiments were performed in Ca^{++} chelated media, a fraction of axons initially retracts, and then intracellular material recovers towards the ablation point, showing the resealing of the axon. When axons retract after partial ablation, axonal diameter is thinning down, but when resealing happens, recovery of axonal diameter to its pre-ablation state is seen. Previous Studies have shown that a transection leads to Ca^{++} entry via mechanosensitive calcium channels in the plasma membrane. It has also been shown that a large influx of Ca^{++} results in proteolysis over a significant length of the axon and this may increase axonal degeneration after ablation (or induced injury)[5][6]. However, it is unknown whether this degeneration or

retraction is reversible. This part of the thesis shows that it is reversible in partially ablated in Ca^{++} chelated media. However, it is not clear how axons reseal in calcium-chelated. So it is interesting to explore the axonal resealing mechanism and how actin and microtubules play a role in the resealing process.

Axon resealing after partial ablation in calcium chelated media

when axons are partially ablated in normal media containing calcium, a large elevation of internal Ca^{++} is observed. However, when extracellular or intracellular calcium is chelated, there is almost no Ca^{++} elevation after axonal ablation. This suggests that entry of extra-cellular Ca^{++} is required for this response, and part of the elevated levels may be due to the release of Ca^{++} from internal stores.

After partial ablation, axons retract completely when axons are ablated in normal media, but two types of responses are seen when extracellular calcium is chelated. Some fraction of axons initially retract and stop at some point or continue to retract slowly compared to control axons. Remarkably, the remaining fraction of axons stop retracting and undergo a resealing process by which it completely recovers the uniform diameter. Despite the axonal structure being polar, primarily due to the polar arrangement of microtubules, the resealing has been observed from both sides (cell body and growth cone). The quantitative analysis of resealing has been done by analysing the contour length of regrowing ends of axons as a function of time.

Recovery of cytoskeletal components during axonal resealing

Here we have investigated the roles played by microtubules and actin during axonal resealing. Labelling with fluorescent dyes that label only the polymerised filaments shows that in the control case, both microtubules and actin filaments retract away from the ablation point. But when extracellular calcium is chelated, we observe that, in a fraction of axons, this retraction gets arrested and is then followed by a repolymerisation process. The extent of recovery is studied using intensity analysis of the recorded timelapse images. This shows that the recovery of fluorescence intensity is almost complete or, in the case of actin filaments, sometimes even exceeds the initial intensity.

Correlating the intensity recovery with the recovery of diameter after partial ablation reveals some additional interesting features. Recovery of microtubule intensity is always correlated with a recovery in axonal diameter. However, recovery of actin filaments in the previously retracted region does not necessarily lead to a recovery in diameter. We discuss possible reasons for this observation.

Microtubule polarity during axonal resealing

It has been established from previous studies that microtubules are polarised filaments with +end and −end, and most of the microtubules in vertebrate axons have +ends towards the growth cone. The microtubule polarity can be revealed by the +tip binding protein EB3. So when microtubules polymerise and grow, the +tip binding

protein EB3 binds to microtubules in the growth direction[7]. when microtubules regrow, how do they maintain the polarity? Normally, microtubule growth predominantly happens at the +end, but surprisingly we observe that the recovery of microtubule intensity can occur in either direction (both sides). This leads to the question of whether the recovery is happening via the growth of existing filaments or via the nucleation of fresh tubules, which may or may not be randomly polarised. This is investigated using the EB3 tip marker.

Summary

This thesis focuses on the retraction and resealing of axons after laser ablation. In the first part of the thesis, the retraction responses of axons are analysed in the presence of various pharmacological agents to understand the roles of various cytoskeletal components. Trypsin-induced retraction response is also investigated and compared with laser induced transection. In the second part of the thesis, it is shown that partially ablated axons can undergo resealing. The dynamics of actin filaments and microtubules during this process are investigated using fluorescence imaging of the polymerisation process and using a microtubule tip-marker.

Publications

- Anagha Datar, Jaishabanu Ameeramja, Alka Bhat, Roli Srivastava, **Ashish Mishra**, Roberto Bernal, Jacques Prost, Andrew Callan-Jones, Pramod A Pullarkat. The Roles of Microtubules and Membrane Tension in Axonal Beading, Retraction, and Atrophy. *Biophysical Journal*, 117, 880-891, 2019.

- Neha Paddillaya, **Ashish Mishra**, Paturu Kondaiah, Pramod Pullarkat, Gautam I. Menon and Namrata Gundiah. Biophysics of Cell-Substrate Interactions Under Shear. *Front. Cell Dev. Biol.*, 7:251, 2019.

- Shivani Bodas, **Ashish Mishra**, Pramod Pullarkat, Aurnab Ghose. Initiation and maturation of the early axonal βII-spectrin membrane-associated periodic skeleton requires active cytoskeletal remodelling. BioRxiv 2025.02.19.639207.

Contents

Chapter 1

Introduction

1.1 Introduction

The nervous system, which consists of the brain, spinal cord, and complex web of nerves, plays an essential role in controlling, directing, and facilitating communication among different body parts. The human nervous system is predominantly classified into two parts, i.e., the Central Nervous System (CNS) and Peripheral Nervous System (PNS). The former includes the neuronal networks and other supportive cells found in the brain and spinal cord, and the latter includes the nerves extending to the rest of the body. The CNS mainly processes and interprets signals, while the PNS transmits these signals to and from the CNS to maintain homeostasis in the body and also controls muscle activity. Any disconnection in the signal transmission due to injury or neurodegenerative diseases in either the PNS or CNS can severely affect the proper functioning of the nervous system.

Every day, thousands of new neurons are generated through neurogenesis in the adult hippocampus (a part of the CNS), but most of these new cells do not survive [8]. So, a large percentage of neurons in PNS and CNS, which are created at the embryonic stage, have to be maintained in the organism throughout its lifespan.

During an organism's lifetime, axons experience significant stretch deformations under various normal and abnormal circumstances. There is no cell injury in normal conditions; for example, the limbic movement of a rat results in the extension and flexion of sciatic nerves [9]. However, abnormal conditions such as head trauma or crush injury to PNS neurons can cause both local and global disruption of the nervous system, potentially resulting in progressive degeneration and leading to debilitating conditions. The CNS and PNS in humans are depicted in the figure 1.1.

1.2 Neurons

Neurons, the cells that form the nervous system, are unique in their morphology, functionality and composition. Typically, a protrusion known as an axon grows on one side of an initially spherical cell body (soma), and other regions develop branched extensions called dendrites. In the case of humans, axons can extend from a few millimetres to about a meter in length (from the spinal cord to the toe) and are about a micron in diameter. They maintain their shape and integrity over such long ranges to ensure signal transmission

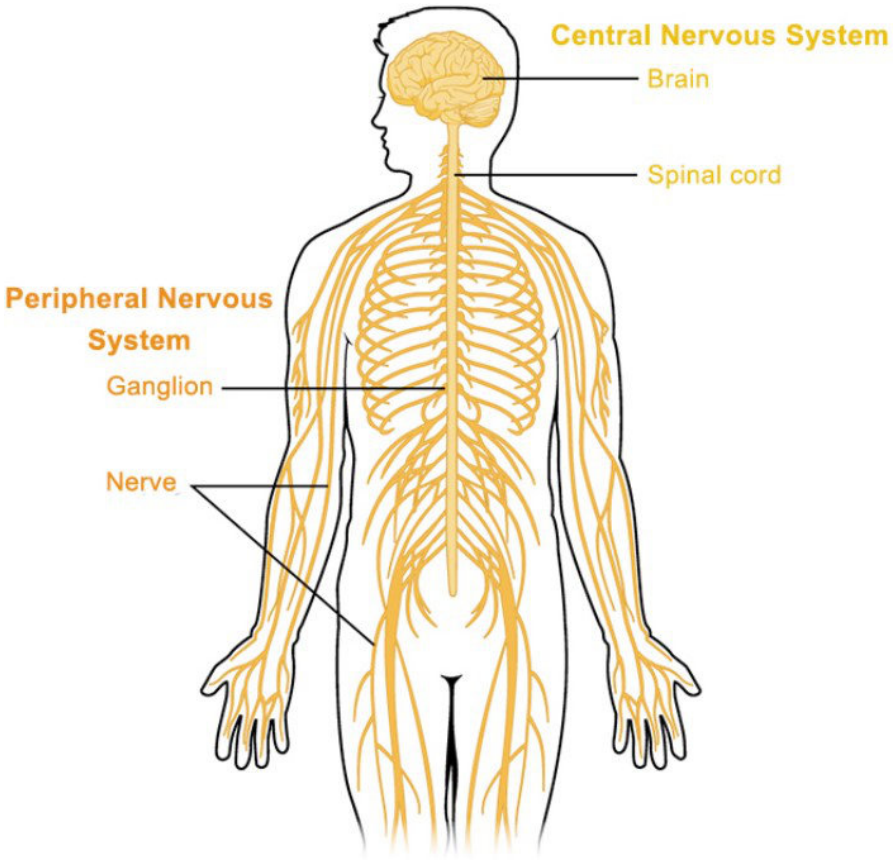

FIGURE 1.1: **The human nervous system.** The CNS and PNS together form the nervous system of humans. The brain and spinal cord are part of the CNS, and the PNS includes the nerves outside, reaching each and every organ of the body. The CNS and PNS function together to coordinate and regulate physiological processes. (Image credit- https://qbi.uq.edu.au/brain/brain-anatomy/peripheral-nervous-system)

throughout their lifetime. This is aided by a network of cytoskeletal components and the membrane, along with motor proteins and various organelles. During development, axons and dendrites grow via the action of a palm-like motile structure at their extremities (away from the soma). This structure, called the growth cone, has filopodia acting as sensors for detecting extracellular cues and lamellipodia that apply traction force for movement [10]. The schematic of a neuron is shown in the figure 1.2.

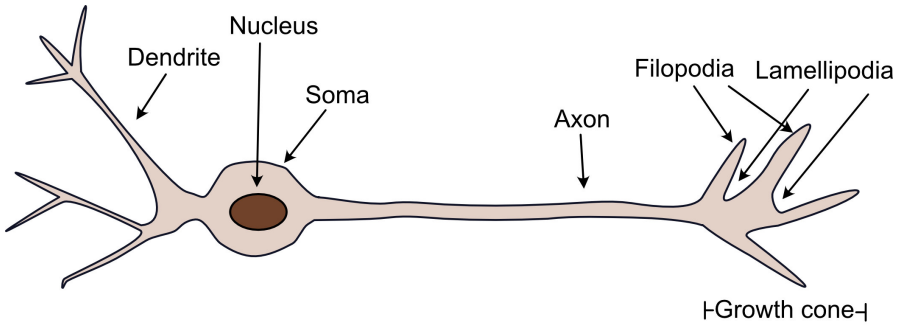

FIGURE 1.2: **Neuronal cell structure.** Neurons possess unique morphology, having cell bodies (soma) with dendrites at one end and an axon at the other. During development, both axons and dendrites possess dynamic structures called growth cones, which guide their outgrowth and navigation. The long tubular protrusion connecting the soma and growth cone is called the axon, whose length may vary from a hundred microns to a meter in humans. In a neuronal network, the dendrites collect all the information from other neurons and transmit it through the axon to the target neuron. The growth cone detects the extracellular milieu while navigating pathways during growth.

Neurons are classified structurally into four types and functionally into three categories.

1.2.1 Structural Classification of Neurons

A schematic illustrating the different structural types of neurons is shown in the figure 1.3.

Unipolar Neurons - These neurons have a single process extending from the cell body, which subsequently branches into dendrites or an axon. They are uncommon in humans but are found in the cochlea, a spiral-shaped organ in the inner ear that detects sound vibrations and converts them into electrical signals.

Bipolar Neurons - These neurons have one axon and one dendrite extending from the cell body; these neurons are found in sensory organs such as the retina and the olfactory system.

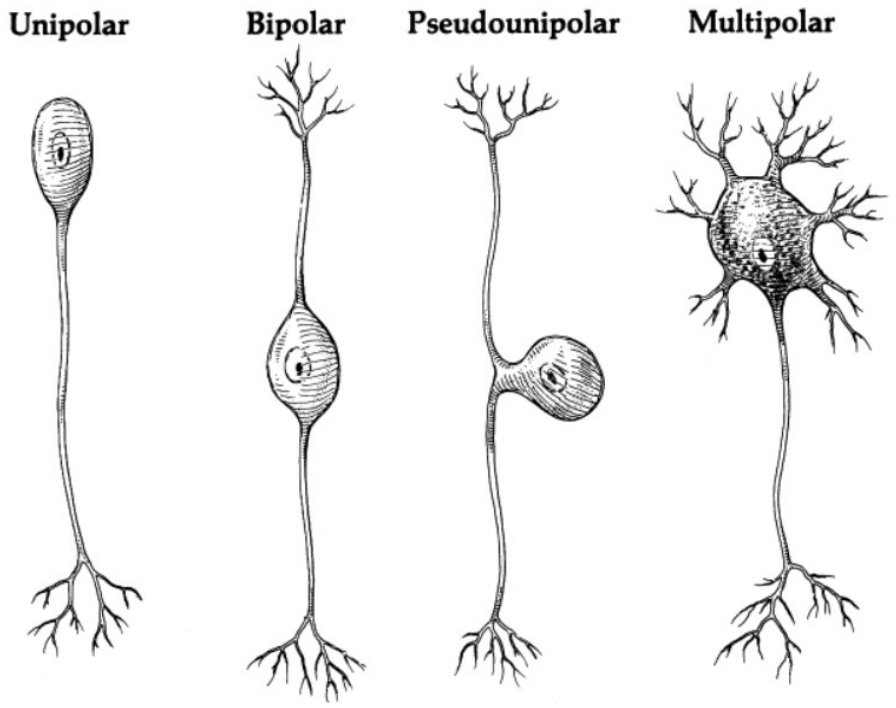

FIGURE 1.3: **Types of neurons based on structure.** True unipolar neurons do not exist in the nervous system of adult vertebrates. Bipolar neurons, along with their variant as pseudounipolar neurons, constitute all primary sensory neurons in the PNS. Multipolar neurons possess many branched processes extending in multiple directions, mostly found in the CNS. Image is taken from [11]
.

Pseudounipolar neurons - These neurons are modified forms of bipolar neurons. Both opposing protrusions move around the cell body during development and combine into one, where one process leads to the PNS and the other to the CNS, similar to bipolar. This kind of structure bypasses the cell body for fast signal transmission, which is necessary for pain and other sensations. Dorsal Root Ganglion (DRG) neurons are pseudounipolar, with the cell body located outside the CNS. One branch of the axon innervates the peripheral nervous system (PNS), while the other branch enters the spinal cord to transmit sensory information.

Multipolar Neurons - The most common type, these neurons have

one axon and multiple dendrites from the soma and are prevalent in the brain and spinal cord [11].

1.2.2 Functional Classification of Neurons

Sensory Neurons (Afferent Neurons) - These neurons transmit sensory information from the external environment via PNS to the CNS. They are responsible for sensing stimuli like touch, pain, temperature and light.

Motor Neurons (Efferent Neurons) - These neurons transmit action potentials from the CNS to muscles or glands, facilitating movement or physiological responses.

Interneurons - These neurons are connectors between sensory and motor neurons [11].

1.3 Neuronal cytoskeleton and structure

Neurons possess a distinctly compartmentalised structure, with dendrites and axons, each supported by cytoskeletal components. This cytoskeleton has mainly three types of components–microtubules, actin filaments and neurofilaments [1]. Many molecular motors and other related proteins are crucial for the organisation and dynamics of these filamentous structures [12].

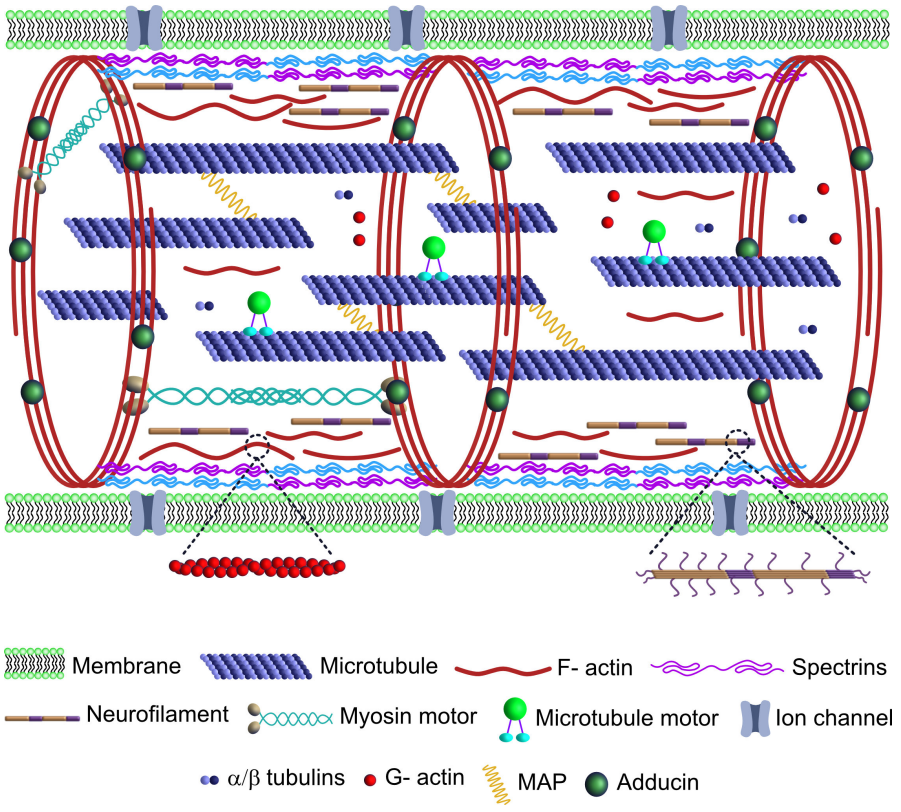

FIGURE 1.4: **Ultrastructure of axons.** Axon is roughly one micron thick in vertebrates, and various biopolymers are decorated inside this thin tube. The axonal core is mostly comprised of microtubules linked with microtubule-associated proteins. Molecular motors use microtubules as rail tracks to transport cargo. Neurofilaments are apolar biopolymer filaments that surround the core. F-actin forms periodic rings composed of several long, intertwined filaments. These rings are connected by spectrin tetramers, associated with myosin motors, and capped by adducin. Other F-actin structures are also present in the axon. The axonal membrane is made up of phospholipid molecules that work as a barrier between the extracellular and intracellular environments. It has many ion channels and pumps that play a crucial role in generating and propagating action potentials, as well as in regulating other neuronal functions.

The structure of the neuronal cytoskeleton differs notably between vertebrates and invertebrates. Studies comparing a range of model organisms such as *Drosophila melanogaster*, *Caenorhabditis elegans*, *Xenopus laevis*, chick, zebrafish, and rodents have provided important insights into the arrangements that are shared across species as well as those that are unique to specific organisms [13].

In vertebrates, axonal microtubules are primarily arranged in a coaxially aligned fashion, with their +ends pointing away from the soma (explained in detail in subsection 1.3.1). These microtubules are surrounded by a dense matrix of neurofilaments, which are critical for maintaining axonal diameter and ensuring high conduction velocity [14, 15]. In contrast, dendrites contain microtubules with mixed polarity—both + and −ends oriented in either direction [16, 17]. This difference in microtubule orientation is a key cytoskeletal feature distinguishing axons from dendrites in vertebrate neurons.

In invertebrates such as C. elegans and Drosophila, axonal microtubules are uniformly oriented, similar to vertebrate axons. Dendritic microtubules are predominantly minus-end-out, differing from the mixed polarity seen in vertebrates and serving as a defining cytoskeletal characteristic [13]. Moreover, while neurofilaments are abundant in vertebrate axons, they are absent in C. elegans and Drosophila [15]. These invertebrates rely instead on microtubules and microtubule-associated proteins (MAPs) to maintain their structure and function [13].

Filamentous actin (F-actin) is found in the cortical layer located immediately beneath the axonal membrane. Other than recently discovered actin structures, explained in subsection1.3.3, actin filaments are also found in the growth cone of developing neurons in high concentration and are more dynamic compared to other parts of the axon [18]. In both invertebrates and vertebrates, the axonal

cytoskeleton shares conserved elements, including central longitudinal F-actin trails and periodic cortical F-actin rings organised by spectrin proteins [19, 20].

The ultrastructure of an axon is shown in the figure 1.4.

1.3.1 Microtubules

Microtubules are a crucial part of the neuronal cytoskeleton and are important for maintaining cell structure as well as for serving as tracks for intracellular transport and neuron function. These are composed of heterodimers of α- and β-tubulin that polymerise in a head-to-tail fashion to form protofilaments. These protofilaments assemble into hollow tubes via lateral association with inner and outer diameters of around 17 nm and 25 nm, respectively. In nature, microtubules with 13 protofilaments are found in abundance [1, 2, 17, 21]. The schematic of microtubules and tubulin dimers is shown in the figure 1.5.

Every microtubule is structurally different at two ends; one end, known as the $-$ end, is occupied by α-tubulin, whereas β-tubulin is located at the other end, called the $+$ end. Axons are polarised structures with microtubule +ends oriented towards the growth cone, whereas mixed MTs polarity is observed in dendrites of vertebrates [17]. There are two domains, stable and labile, found on individual microtubules. The stable domain is towards the minus end, while the labile domain is found at the plus end of the microtubules [22].

Axonal microtubules are typically arranged in parallel bundles, which is facilitated by various cross-linking proteins like plakons and microtubule-associated proteins (MAPs), such as tau, which are thought to stabilise microtubules and prevent their disassembly [17, 23]. The number of microtubules in axonal cross-sections varies, typically ranging from 10 to 100 microtubules, depending on the axonal type and the function [17]. Also, Neuronal microtubules are generally more stable than those in dividing cells, possessing both stable and labile fractions, each playing distinct functional roles [23].

Disruptions of microtubule stability are implicated in several neurodegenerative diseases. For example, hyperphosphorylation of tau may result in microtubule destabilization, contributing to the development of disorders like Alzheimer's disease [17, 23]. Additionally, under rapid stretching conditions, axons show a progressive loss of microtubules. This indicates that sudden mechanical strain can lead to the disassembly of microtubules and a weakening of axonal structure [24]. Consequently, understanding the mechanisms that govern microtubule stability is essential for developing therapeutic strategies for these conditions.

1.3.2 Neurofilaments

Neurofilaments (NFs) with a diameter of 10 nm, another key component of the axonal cytoskeleton, are the most flexible among cytoskeletal elements. They are non-polarised biopolymers, unlike

microtubules and actin filaments. The neurofilament is depicted schematically in Figure 1.5. NFs are essential biopolymers comprising multiple types of subunit proteins and further assembled into long and dense filamentous networks. In mammals, the five subunit proteins include Neurofilament-Light (NF-L), -Medium (NF-M), -Heavy (NF-H), α-internexin, and peripherin. These subunits come together in proportions that vary based on species, developmental phase, neurodegenerative disease, age, neuron location, and type of neuron. Moreover, cytoskeletal cross-linking proteins such as plectins and BPAG1-n interconnect neurofilaments with microtubules and actin filaments, contributing to a stable yet dynamic scaffold within the axon [2, 14, 25]. Microtubule–neurofilament (MT–NF) cross-bridges were also observed, and these have been suggested to consist of microtubule-associated proteins (MAPs) or MAP-like factors, such as tau, MAP2, or MAP6, and may also include motor proteins [13]. Neurofilaments are thought to form hydrogel-like networks [26] and behave as inert molecules in a dilute solution, remaining relatively free to move independently and occupy the available space within the axon [13].

Unlike microtubules, which primarily facilitate cargo transport, neurofilaments along with microtubules are responsible for determining axonal diameter, which is crucial for regulating nerve impulse conduction velocity [12, 25]. They interact with microtubules to form a supportive scaffold, providing tensile strength to axons [14]. However, not all neurons possess neurofilaments. For example, neurons

in the invertebrate organism Drosophila melanogaster (fruit fly) lack neurofilaments. This absence of neurofilaments highlights a fundamental difference in cytoskeletal organisation between vertebrate and invertebrate neurons [13].

Disruptions in neurofilament organization are linked to various neurodegenerative disorders, including Amyotrophic Lateral Sclerosis (ALS) and Parkinson's disease [27]. In ALS, for example, the accumulation and clustering of neurofilaments in motor neurons lead to axonal degeneration and impaired motor function [27].

1.3.3 Actin filaments

Actin is an essential cytoskeletal component in neurons, playing a critical role in cell shape, intracellular transport and growth cone motility. Filamentous actin is a semi-flexible, structurally polar biopolymer having a persistence length of $\sim$10 μm and a diameter of $\sim$4–5 nm. The soluble globular actin (G-actin), the basic monomeric subunit having two ends, polymerises to form double-stranded helical filamentous actin [2, 12]. At the barbed end (growing end) of F-actin, G-actin goes through a subunit addition process, while a monomer detachment process occurs at the pointed end. However, the weak interactions between actin monomers lead to fast polymerized to depolymerized transitions [12, 28]. A schematic of F-actin and G-actin is presented in the figure 1.5.

Actin dynamics can be regulated by various actin-binding proteins (ABPs) through different mechanisms. G-actin can be sequestered by β-thymosin, preventing filament formation. The initiation of filament formation can occur through the actions of Formins and the Arp2/3 complex. At the barbed end of actin filaments, the protein capZ inhibits polymerization, while ena (in Drosophila) promotes it. Conversely, at the pointed end, tropomodulin prevents depolymerization, and actin depolymerizing factor (ADF)/cofilin facilitates depolymerization. Additionally, various actin-binding proteins (ABPs) play significant roles: Filamin crosslinks actin filaments, α-actinin bundles them, tropomyosin stabilizes them, and cofilin is involved in severing them. Furthermore, vinculin helps to link F-actin to integrin-mediated adhesion sites on the substrate [12, 18].

Earlier, F-actin was reported to act as a cortical scaffold for the plasma membrane. Recent studies have revealed that different actin structures (e.g., actin rings, actin trails, actin waves, actin hotspots) play different roles in regulating neuronal function [29]. Super-resolution microscopy has revealed that F-actin rings connected with spectrin tetramers assemble at spatially periodic distances (180–190 nm) along the axon to generate a lattice-like scaffold beneath the membrane circumferentially [19]. These rings are primarily composed of braided-like stable actin filaments organized by spectrin and ankyrin, providing resistance to mechanical stress on the axon [30, 31]. Adducin is a capping protein that caps the barbed end of actin filaments and promotes actin-to-spectrin binding [19]. The

myosin motors connect with actin rings and act as regulators of axial and circumferential tension [32, 33]. These details are illustrated in the Fig 1.4.

Actin hotspots are the locations in axons, approximately 3–4 µm apart, where actin undergoes continuous processes of polymerization and depolymerization. These hotspots serve as a centre for rapid F-actin formation, with elongated actin filaments extending in both directions along the axonal shaft, which are called actin trails. These dynamic actin trails may act as tracks for short-range myosin-dependent movement [34].

Actin waves are transient, moving actin structures that travel along the axonal shaft. They play a critical role in neuronal growth, polarization, and regeneration. These waves start along the proximal axon and move forward along the axon, encouraging actin polymerization. Actin waves have been observed predominantly in developing neurons [29, 35, 36].

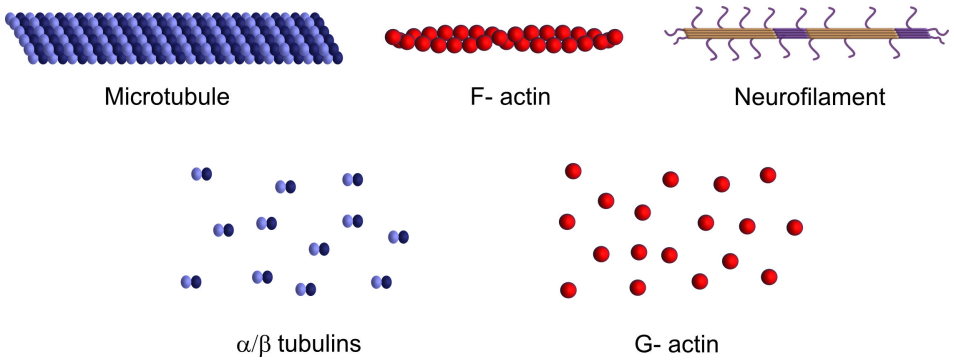

FIGURE 1.5: **Cytoskeletal elements.** Microtubules are heterodimeric bipolymers made up of α- and β- tubulin dimers. Actin filament, showing helical structure, consists of G-actin. Neurofilaments are made up of many protein subunits having side arms.

1.4 Axonal transport

Axons are lengthy extensions, stretching from several hundred microns to meters in humans, and they may extend as far as 30 meters in blue whales [37]. This impressive axonal length presents a significant challenge for neurons in maintaining homeostasis. Most of the macromolecule synthesis takes place in the cell body, which is a requirement for axonal and synaptic function. Also, the macromolecules and organelles are moved from the presynaptic terminal to the cell body for degradation or recycling. So, passive diffusion alone would take several hours to direct the materials to the appropriate location along micrometre-scale distances in the axon. For eaxmaple, a vesicle would take t = 10^5 seconds (or $\approx$ 27.8 hours) to diffuse 1000 μm. To overcome this issue, axons use active transport driven by motor proteins [1, 38, 39].

The transport system includes the axonal cytoskeleton and three families of molecular motor proteins: kinesin, cytoplasmic dynein and myosin. Although there is a wide range of motor proteins, they possess several common features. Motor proteins have highly conserved domains that bind to the cytoskeleton and ATP (the molecule that stores the energy needed for movement), as well as a more variable tail region that binds specific cargoes for transport [2, 12]. The microtubule cytoskeleton acts as tracks for kinesin and dynein to

facilitate long-range transport, and myosin moves along actin filaments, which is typically associated with contractile forces and short-range transport [12].

Microtubule-based motors, kinesin and dynein, travel in opposite directions; dynein travels toward the minus-end of MTs, while most kinesins travel toward the plus-end. Due to the polar microtubule organisation in axons, kinesins carry out the anterograde (away from the cell body) transport of axonal proteins, and dynein mediates retrograde (towards the cell body) transport [1, 12]. Moreover, MAPs are also known for their role in regulating transport through the modulation of motor interactions with the MTs [40]. Post-translational modifications (PTMs) further influence transport by altering motor protein activity and modifying microtubule tracks, thereby affecting cargo binding and overall transport efficiency [41].

Actin filaments are short, typically only a few microns in length, and lack consistent polar organisation over longer distances, which limits their role to short-range transport [42].

Axonal transport can be categorised into two based on speed - fast ($\sim$ 50-200 mm/day) and slow ($\sim$ 0.2 - 10 mm/day) axonal transport. Differences in axonal transport speeds mainly depend on how long cargoes stay actively moving. In slow transport, cargoes move in quick bursts followed by long pauses, leading to a slower overall speed [38]. Fast transport is responsible for carrying vesicular cargoes (neurotransmitters, lysosomes) and mitochondria, whereas

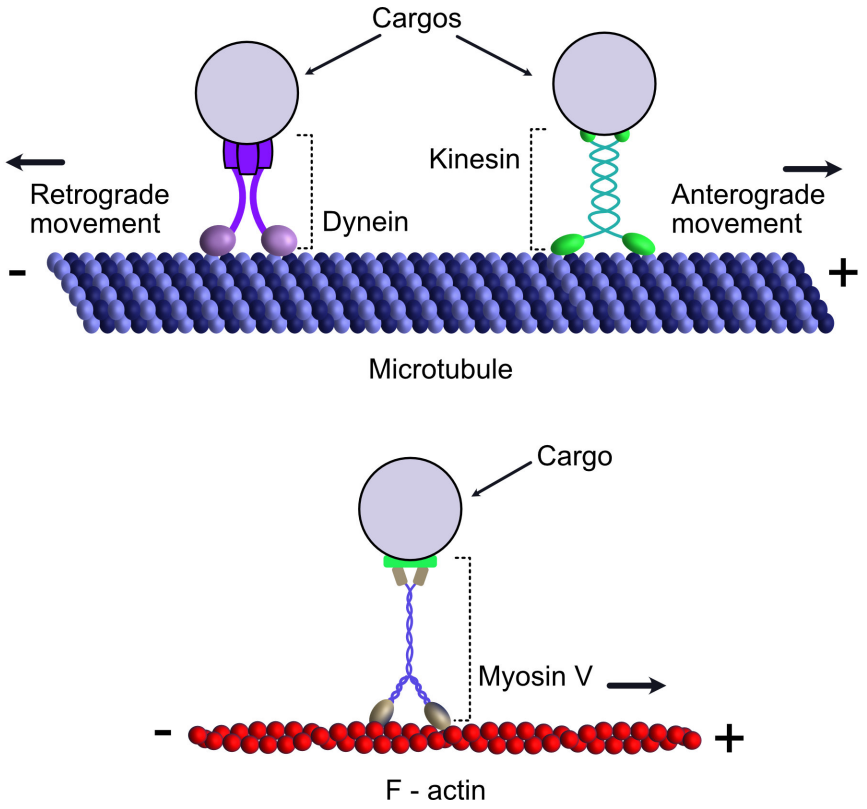

FIGURE 1.6: **Molecular motors on the cytoskeleton.** The kinesin and dynein motors carrying cargo move in the + and − directions on the microtubule, respectively. The kinesin-driven transport towards the growth cone is known as an anterograde movement, and dynein-driven transport towards the cell body, a retrograde movement. Myosin V is a motor protein attached to actin, transporting cargo from the pointed end (−) to the barbed end (+). The bold arrows show the direction of transport.

slow transport delivers cytoskeletal and cytosolic (or soluble) proteins [43]. A schematic showing vesicle transport along microtubules and F-actin by motor proteins is presented in the figure 1.6.

1.5 Axonal polarity

At the developmental stage, axon polarization involves the process of symmetry breaking in a developing neuron, resulting in a polarized neuron with distinct axons and dendrites. The dendrites receive and integrate all the incoming information from other neurons and

transmit it through the axon to another target neuron, ensuring one-way signal transmission [44].

During development, neuronal cells break their symmetry via extrinsic (extracellular cues) and intrinsic signalling and regulatory pathways that regulate actin and microtubule dynamics. The actin cytoskeleton regulators also play a crucial role in neuronal polarization, with the Rho family of small GTPases [45]. Many other signalling molecules like Cdc42, Rac, or PAR proteins also lead to disruption of symmetry by increasing their concentration locally in specific areas of the plasma membrane. These molecules may initiate the recruitment of other signalling molecules that direct symmetry breaking [46]. Figure 1.7 illustrates the stages of neuronal polarity.

Microtubules and actin filaments are inherently polar cytoskeletal structures [47]. The microtubule's polarity is present not just at its two ends but throughout its entire structure length. When neurites develop into axons, there is the possibility that preassembled, +end directed microtubules are transported towards the growth cone. This oriented microtubule polarization is preserved in the axon of the mature neuron, whereas dendritic microtubules in vertebrates show mixed polarity, having both + and − ends present in different orientations [23, 45].

Microtubule plus-end tracking proteins or +TIPs are associated with the +ends of microtubules during their assembly. They are mostly found near +ends, and the association of +TIPs is transient with

+ends. As the microtubule polymerises, the +TIPs detach from the older region of the microtubule while continuing to associate with the +ends [48]. The microtubule polarity can be revealed by artificially expressing the fluorescent +TIP protein EB3-GFP. So when microtubules polymerise and grow, the +TIP protein EB3 binds to their +ends and shows comet-shaped fluorescence in the growth direction [7, 17].

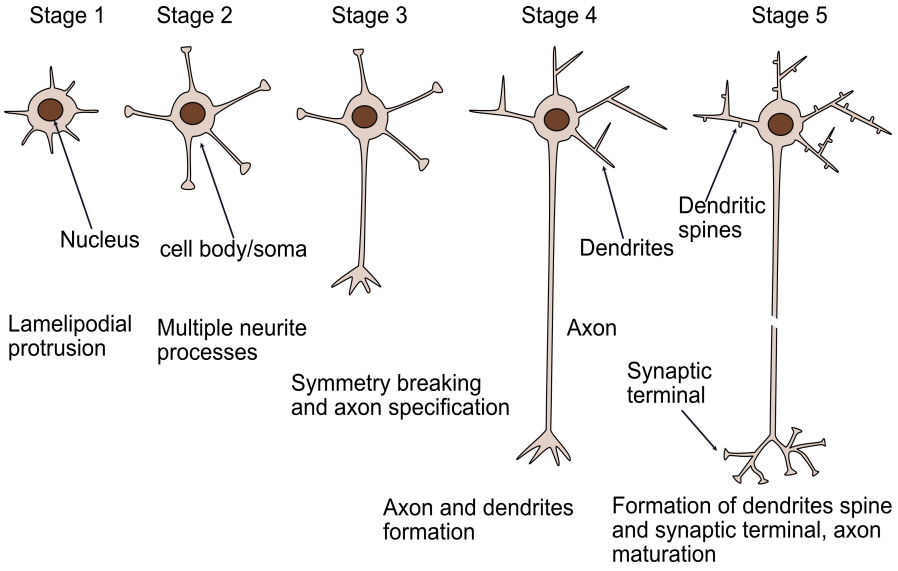

FIGURE 1.7: **Stages of neuronal polarity.** In vitro, the round cells exhibit active lamellopodia in stage 1, shortly after seeding. In stage 2, they grow several immature neurites. During stage 3, one of these neurites begins to break symmetry and try to form an axon with a growth cone. The remaining small neurites develop into dendrites while the axon elongates further in stage 4. Stage 5 shows the maturation of the axons and the formation of dendritic spines and synaptic terminals.

Axonal polarity sorting is a mechanism in which microtubules achieve and preserve the +end orientation in the axon away from the soma. The molecular motor proteins, such as cytoplasmic dynein, might be crucial in polarity sorting. It has also been reported that crosslinking proteins are needed to restrict microtubule movement and enable polarity sorting via dynein efficiently. The proposed mechanism might

be where dynein motors spatially separate microtubules with opposite orientations, the −end out microtubules are transported back to the cell body, and the +end out moves towards the growth cone to establish and maintain the polarity [49, 50].

1.6 Previous work on axonal mechanics

Axonal mechanics contribute significantly to the healthy development and upkeeping of the nervous system and axons' vulnerability to injury and neurodegenerative conditions. The axon's longer tubular structure enables it to convey action potentials, and this requires transport materials across extensive distances. The axon exhibits different passive and active responses to preserve its form and function, particularly when facing biochemical and/or mechanical perturbations [51].

The axons are in a state of mechanical force balance mediated by cytoskeletal components and their membrane at the physiological level. Actomyosin contractility generates tensile forces along the axon shaft. Microtubules, which are rigid polymers with high persistence length, provide internal compressive resistance through polymerisation cross-linking and motor-driven sliding. Disruptions to the mechanical equilibrium within the cytoskeletal elements lead to axonal retraction involving actin and microtubule-associated molecular motors, the dynamics of polymerisation, and the passive mechanics of the cytoskeleton [51–55].

Apart from disease-related alterations in biochemical pathways, mechanical perturbations such as stretching or cutting can perturb the mechanical balance. The most studied perturbation to study axonal mechanics is the stretching of axons using a microneedle or actuator-based cantilever. Early experiments conducted by groups of Steven Heidmann and Dennis Bray have used the calibrated glass micro-needles to exert pull on either PC12 neurites or chick Dorsal Root Ganglia (DRG) axons in culture. They showed that axons behave like viscoelastic materials under low forces, are capable of producing active tension, and can display tension-driven growth when subjected to higher stretching forces [56–58]. Using a coated glass micro-needle attached to a neuronal growth cone, the linear relationship of axial tension and induced length variation of axons was demonstrated in cultured PC-12 neurites [57]. When axons are stretched by applying a step-like shift to the microneedle base, the resulting excess tension on the axon and the strain in the axon relax over time. It was also observed that within <100 microdynes applied force limit, stretched PC12 neurites displayed an initial sudden jump in strain, which was followed by a gradual progression of the strain towards a plateau value with a response time of approximately 10 minutes [58]. Moreover, the tension decreases from a peak value right after the stretch to a stable non-zero level, referred to as rest tension, which is around 30 microdynes (0.3 nN). Upon being freed from the needle, the neurites returned to their original length in approximately 1 minute [51].

Tahir Saif's group performed in vivo stretching experiments on Drosophila

neurons using micro-machined force sensors and reported that axons behave like elastic springs, exhibiting a linear force deformation relationship. Following deformation, the force reaches a steady state value. Moreover, axons sustain a resting tension of 1-13 nN and actively regulate their tension when released from a stretched condition [59].

Miriam Goodman's group conducted experiments on C. elegans using Fluorescence Resonance Energy Transfer (FRET) based genetically-encoded molecular force sensors into β-II spectrin and reported that the spectrin molecules that link actin rings are held under tension. Measurements of axonal recoil further support this after laser axotomy performed in the same study.[60]. Recently, using an optical fibre-based force apparatus, a quantitative evaluation of the mechanical role of the actin-spectrin scaffold in stretching deformation is reported. This research revealed that actin and spectrin played significant roles in axonal elastic modulus under stretch. Moreover, they reported when axons are stretched, the axonal actin-spectrin scaffold might function as a shock absorber by permitting spectrin domains to unfold and thus release tension to protect the axon against stretch induced damage [31].

To evaluate axonal contractility, a technique based on trypsin-mediated de-adhesion was employed to detach curved axonal segments from the substrate. This approach demonstrated that actomyosin contractility drives the axon to shorten toward its minimal length (making it straight) [61]. In another experiment, Tahir Saif's group used a

microfluidic device to locally treat a segment of an axon with cytoskeletal disruption drugs targeting F-actin, myosin motors, and microtubules. Disruption of F-actin or myosin caused a complete loss of intrinsic tension, suggesting interconnected actomyosin contractile units. On the opposite end of the spectrum, microtubule destabilisation decreased local bending stiffness and had no effect on intrinsic tension, indicating that microtubules passively resist contractile forces and do not actively generate them [62]. So, actin and myosin II play a role in producing longitudinal tension. Saif's group showed that the axonal actomyosin machinery plays a role in producing circumferential tension [32]. The study done by Monica Sousa's group demonstrated that myosin II is found in the membrane periodic skeleton (MPS) and is responsible for axonal diameter expansion and contraction [33]. These studies indicate that actomyosin machinery is primarily involved in axonal contractility, leading to axon tension generation.

1.7 Physical Models of Axonal Mechanics

Following the foundational work by Heidemann and Bray's group [56–58], which proposed that axons behave as viscoelastic structures. Dennerll et al. [58] proposed a mechanical model to explain the passive, viscoelastic behaviour of axons. The model consists of a stiff spring in series with a Kelvin–Voigt element, the latter comprising a less stiff spring in parallel with a dashpot. The former relates to

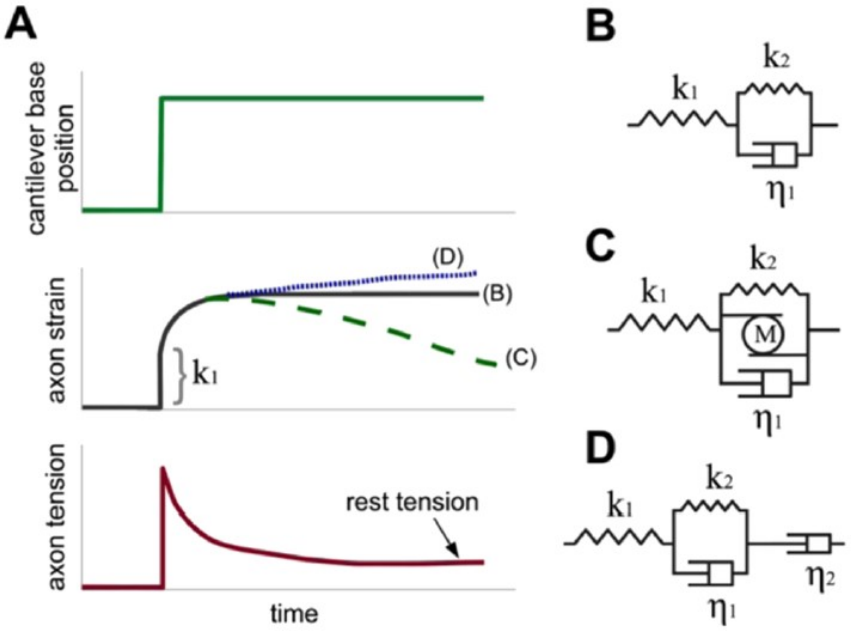

FIGURE 1.8: (A) Illustration of axonal deformation in response to a step-stretch, applied by displacing the base of a micro-needle, along with the resulting strain evolution predicted by different viscoelastic models (B–D). The strain behaviour for the model in (B) is represented by a solid black line, while the model in (C) is shown with a green long-dashed line, and the model in (D) is represented by a fine blue dotted line. Additionally, the tension response corresponding to model (B) is plotted, demonstrating that axons relax to a non-zero baseline tension over long durations. (B) A spring-dashpot representation introduced in early studies to describe viscoelastic behaviour observed in micro-needle stretching experiments. The spring k_1 captures immediate elastic response, whereas the Voigt element (spring k_2 in parallel with dashpot η_1) accounts for time-dependent relaxation in both strain and tension [58]. (C) A model proposed to capture active contractility at the scale of the entire axon. The nonlinear component M, arranged in parallel with a Voigt element, incorporates motor protein activity, rendering the axon contractile at low deformation rates [63]. (D) Over extended periods, stretched axons may exhibit elongation resembling a flow-like response. To account for this, a second dashpot η_2 is added to the passive framework, capturing three distinct regimes: immediate elastic response, intermediate viscoelastic relaxation, and longer-term growth-induced extension [58]. Schematic adapted from [51].

the quick elastic reaction, while the latter pertains to a prolonged viscoelastic solid-like behaviour

Bernal et al. [63] reported that PC-12 neurites exhibit both passive and active mechanical responses. To explain the active contractile behaviour observed in their experiments, they extended Dennerll's

model by incorporating a contractile element representing the activity of molecular motors, such as myosins. This modified model effectively explains the active tension generated in axons. The mechanical behaviour of PC-12 neurites has been investigated using fluid drag forces applied within a flow chamber, revealing not only viscoelastic and active contractile responses but also oscillatory dynamics, as shown by Bernal's group in their study [64].

The growth phase (towed growth phase) starts when the applied tension reaches or exceeds a critical threshold, leading to axonal elongation. Dennerll et al. [58] proposed the first model to explain this growth phase. In this model, an additional dashpot is placed in series with the spring and the Kelvin–Voigt element. Further, O'Toole et al. [65, 66] proposed that the mode of elongation depends on factors such as the force generated at the growth cone, the axonal viscosity, and the strength of adhesions along the axon. They extended the viscoelastic model originally proposed by Dennerll's group [58]. This extended model represents the entire axon as a viscoelastic fluid. In this model, contractile forces at the growth cone are partially dissipated by adhesions to the extracellular substrate along the axon. This framework explains how mechanical tension not only drives tip advancement but also contributes to uniform stretching along the axonal length [65, 66]. Some of the models and their responses are summarised and shown in the figure 1.8.

1.8 Importance of the current research to axonal mechanics

To investigate axonal mechanics, various experimental approaches have been employed, including methods for axon transection. However, many of these techniques also unintentionally stretch the axons during the cutting process (discussed in chapter 3), which can confound the interpretation of mechanical responses. To overcome this limitation, we developed a custom-built laser ablation setup that enables localised disruption of axons, allowing us to precisely mimic injury.

Laser ablation primarily enables detailed investigation of the mechanical and biochemical responses of axons, particularly during the retraction phase following cytoskeletal disruption. While it has often been used in the context of axonal regeneration, its application in studying the responses to injury remains underexplored. Using our LA setup, we focus on dissecting the roles of various cytoskeletal components during retraction, while also leveraging the system to mimic axonal injury. Furthermore, we have examined the influence of calcium in the injury response and monitored the regrowth of cytoskeletal components during axonal resealing, providing insights into the axonal recovery process.

In addition, laser ablation allows for the decoupling of different processes underlying axonal retraction. For instance, the retraction response after ablation is influenced not only by mechanical factors

such as relaxation of prestress and active contractility, but also by biochemical effects like filament depolymerisation. These contributions often act on distinct timescales, providing an opportunity to delineate their individual roles. Pharmacological manipulation using drugs that stabilise or destabilise cytoskeletal components or inhibit motor activity further aids in isolating these effects and understanding their specific contributions to the injury response.

Chapter 2

The Laser ablation setup

2.1 Introduction

A Laser is an abbreviation for Light Amplification by Stimulated Emission of Radiation. It is a high-intensity electromagnetic radiation-emitting device that uses a process of optical amplification mediated by stimulated emission. In 1917, the conceptual idea of the laser was given by Albert Einstein and later, in 1960, American physicist Theodore H. Maiman developed the first laser. The laser beam is highly collimated, monochromatic and coherent, making it useful for various industrial, biomedical and scientific applications. Laser applications in industrial material processing include welding, high-precision drilling, cutting, and etching [67]. Moreover, the laser is also used in optical communication using fibre optics to transmit data over long distances with minimum signal loss [68].

Lasers have been proven invaluable in the medical field because of their accuracy and non-invasive characteristics, which provide solutions for diagnosis, imaging and surgery [69, 70]. The laser lithotripsy technique is used to fragment urinary and biliary stones [69]. In ophthalmology, laser is used to treat myopia and cataracts to regain clear vision. In Neurosurgery, lasers are used for the treatment of hemorrhagic tumours, tumours in deep skull bases and deep ventricles tumours [70]. For biomedical photoacoustic imaging, short pulses irradiate tissues and induce ultrasound waves that are detected on the detector to get high spatial resolution ultrasound images. This is an improvement compared to normal optical imaging, where resolution and contrast are limited by multiple scattering [71].

For biology research, lasers are applied in various fields for imaging or to perturb biological samples for further study of their properties. In fluorescence microscopy, lasers are used to excite the fluorescent molecules tagged in biological samples, which gives information about the sample by emitting fluorescence light. Along with the imaging with laser, various perturbation methods by laser such as optical tweezers, laser catapulting and laser ablation are also used.

Optical tweezers are a non-invasive manipulation technique used to explore the mechanical properties of biological samples. This technique uses laser light to generate highly localised forces on cells, cellular organelles, or synthetic particles (used as handles or probes), enabling the assessment of properties such as mechanical stiffness and viscoelasticity of cells and their surroundings [72].

Laser catapulting is a non-contact technique that employs an intensive shock wave induced by a short-duration laser pulse directed at the cell-substrate interface. This shock wave causes the detachment of selected cells from the surface for further genetic studies. The force exerted on a cell by the pressure wave can also be used to determine the adhesion strength between cells and substrate [73, 74].

Laser ablation (LA) is the technique to remove material precisely from a substance using short pulses of a high-energy laser. In this tool, the laser light interacts with the substance, leading to vaporisation or removal of some part of it. The LA process typically occurs when a substance absorbs enough energy to form plasma. This localised damaging effect on the material can be exploited to infer mechanical stresses in living material like tissue or cellular structures. When subcellular, cellular, or supracellular structures are cut, the responses triggered by the ablation event are used to evaluate the forces experienced by the ablated structures [75–77]. As a result, laser cutting allows for the assessment of cell and tissue mechanics with minimal disruption to the surrounding environment. Moreover, LA is also used for cellular regeneration studies [78].

Along with the properties of targeted materials, laser ablation depends on a few other key factors, including laser energy (pulse energy), wavelength and pulse width. When laser energy exceeds the ablation threshold of the material, it may cause localised removal of material (detailed explanation in upcoming sections). The wavelength of the laser used for ablation is a critical parameter, typically

chosen based on how efficiently the target material absorbs light. The energy of a single photon is given by $E = hc/\lambda$ where E is the photon energy, h is Planck's constant, c is the speed of light, and λ is the wavelength. This inverse relationship means that shorter wavelengths correspond to higher photon energies, which are more effective at disrupting molecular or electronic structures. In biological samples, which are mainly composed of water and organic molecules like proteins, lipids, and DNA, ablation depends on how these constituents absorb light. These molecules have discrete electronic energy levels, and absorption occurs when photon energy matches the energy required to excite electrons or activate molecular vibrations. In the ultraviolet (UV) range, photons have sufficient energy to excite electronic transitions in biomolecules such as nucleic acids and aromatic amino acids, enabling precise and localised ablation with minimal heat diffusion. In contrast, the infrared (IR) region, including both mid-IR and near-IR wavelengths, primarily interacts with water, the dominant component of biological tissue. In the mid-IR, strong water absorption leads to thermal ablation through vibrational excitation and heating. Near-IR lasers offer deeper tissue penetration but are less strongly absorbed [79, 80]. Also, pulse width is the parameter directly influencing the ablation mechanism and the material's response to the laser. The nanosecond (ns), picosecond (ps) and femtosecond (fs) lasers are classified based on pulse width in the order of 10^{-9} sec, 10^{-12} sec and 10^{-15} sec, respectively. A

detailed discussion of laser classification based on pulse width comparison is provided in the next section.

2.2 Comparison of nanosecond (ns), picosecond (ps) and femtosecond (fs) laser ablation

In nanosecond lasers, irradiation with a relatively longer pulse duration in the 1- 100 ns range on the materials is responsible for continuously heating the target. Due to longer (compared to ps and fs lasers) interactions, the laser pulse energy will be spread by heat conduction to an area outside the laser spot size, causing the irradiated target to boil and evaporate. In this case, thermal and mechanical (shockwave and cavitation bubble) effects dominate the laser and sample interaction [79], which is further explained in subsection 2.3.5.

In picosecond lasers, the short laser pulse interacts with the material primarily through multiphoton absorption and avalanche ionisation (cascade ionisation), which generates free electrons. These free electrons can then absorb additional laser energy through inverse Bremsstrahlung, eventually leading to plasma formation [80]. The pulse duration is short enough that there is less heat spread compared to ns lasers. Some thermal effects still occur, but they are reduced, leading to less collateral damage.

In femtosecond lasers, the pulse duration is so short that the material does not have time to heat up before it is removed. Material is

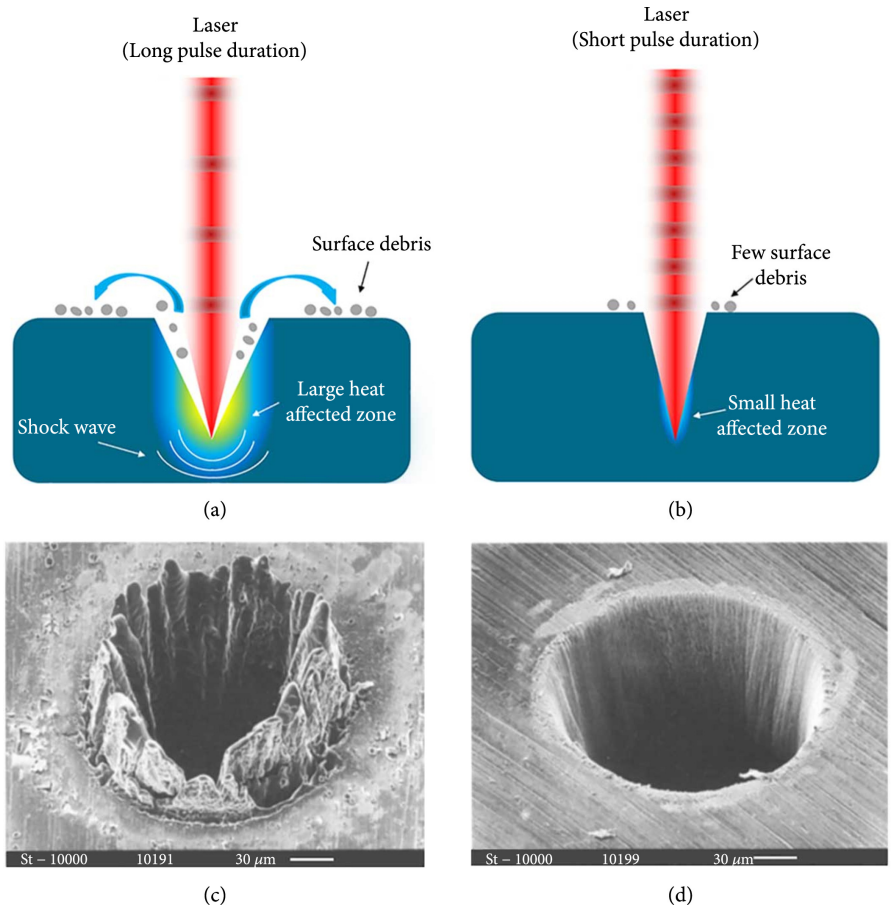

FIGURE 2.1: Schematic of laser material interaction at different pulse widths (a) long pulse width (b) short pulse width. Scanning electron microscope (SEM) images of laser ablated holes made on a steel foil (100 μm) by (c) nanosecond laser (3.3 ns) (d) femtosecond laser (200 fs). Image taken from [81]

.

directly ionised and removed via multiphoton ionisation rather than melting. This results in ultra-precise ablation with no thermal damage, which is ideal for biological tissues and high-precision applications. The interaction of materials with nanosecond and femtosecond lasers is shown in the figure 2.1 and is summarised in table 3.1.

Laser type	Thermal effect	Precision	Applications
Nanosecond	High (causes collateral damage, tissue necrosis)	Low	tumor ablation, dental laser therapy, tissue dissection
Picosecond	Moderate	Moderate	surgery, dermatology, nerve tissue ablation
Femtosecond	very low	High	tumor ablation, dental laser therapy, tissue dissection

TABLE 2.1: Laser types and their effect on material along with applications.

2.3 Mechanism of laser-tissue interaction

Laser tissue interaction refers to the complex interactions occurring when laser light is directed at biological tissues. Tissue response to laser light varies with wavelength, power density (power per unit area), exposure time (pulse duration), and type of tissue exposed. The variety of interaction mechanisms that may occur based on power density and exposure time (figure 2.2) is given as follows-

(1) Photochemical interaction

(2) Thermal interaction

(3) Photoablation

(4) Plasma-induced ablation

(5) Photodisruption

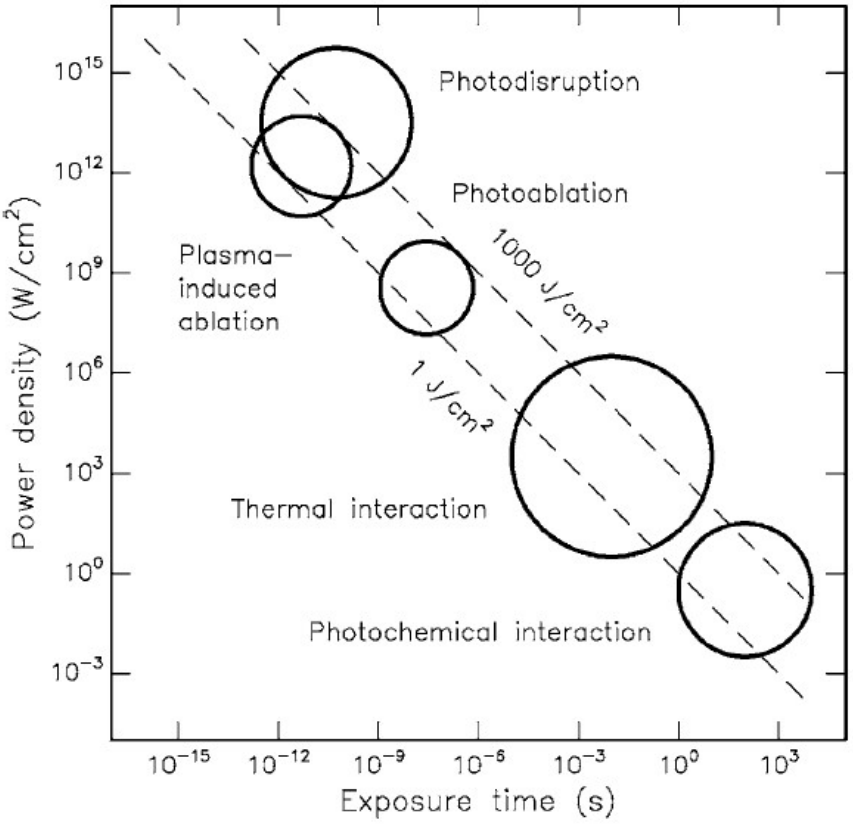

FIGURE 2.2: Map of laser-tissue interactions. The circles give only a rough estimation of the associated laser parameters. Taken from [80]

.

2.3.1 Photochemical interaction

These photochemical interactions occur at very low power densities, approximately 1 W/cm², with exposure times ranging from seconds (> 1 sec) to continuous waves. Such interactions do not lead to any visible changes in the tissue. The well-known process of photosynthesis is an example of photochemical interaction, which demonstrates that light can trigger chemical effects and reactions in macromolecules and tissues [80]. However, similar photochemical processes can also lead to damage. For instance, photo-oxidation, a form of light-induced oxidative stress, can cause localised damage to

axons. Even low to moderate light exposure can generate reactive oxygen species that disrupt the cytoskeleton and compromise axonal integrity [82].

2.3.2 Thermal interaction

Thermal interaction refers to an increase in local temperature in the tissue caused by a laser. A continuous wave or pulsed laser may induce this thermal effect depending on the power density (10 to 10^6 W/cm^2) and pulse duration (1μs to 1min). The heating may result in different effects, such as coagulation, vaporisation, melting, or thermal breakdown of the tissue [80].

2.3.3 Photoablation

Photoablation is a UV laser process that disrupts molecular bonds by delivering high-energy photons. Upon absorption of UV photons, molecules of the target material are energized beyond their bond energy and result in instant dissociation. Effective ablation requires laser intensity above a certain threshold, with the intensity and material absorption properties determining the depth of ablation. At this point, the process is accompanied by audible sounds and visible fluorescence at the laser impact site. The process normally requires power densities of 10^7-10^{10} W/cm^2 and pulse durations in the range of 10 to 100 ns [80].

2.3.4 Plasma-induced ablation

When laser beams have power densities in the range of 10^{11} to 10^{13} W/cm^2 and pulse durations in the range of 100 fs to 500 ps, optical breakdown occurs leading to plasma formation. This process enables plasma-induced ablation, allowing for precise and clean material removal with minimal thermal or mechanical damage, provided laser settings are controlled. The plasma generation depends on the local electric field strength (10^7 V/cm for ps pulses, a value comparable to intramolecular Coulomb fields), which can ionize atoms or molecules. In Q-switched lasers (ns pulses), ionization is mainly due to thermionic emission from thermal energy, whereas ps or fs pulses primarily utilize multiphoton ionization, requiring extremely high peak intensities. Once the initial electrons are freed, either through thermal ionization or multi-photon ionization. They can trigger an avalanche ionization process. In this cascade, a free electron absorbs a photon (via inverse Bremsstrahlung), gains energy, and collides with another atom, ionizing it and releasing more electrons. This cycle repeats and rapidly increases the number of free charges. The avalanche results in the formation of plasma. The plasma absorption coefficient is much higher than that of the material, leading to more efficient energy deposition and enhanced ablation. As plasma develops, it absorbs incoming laser photons and creates a plasma shield that can limit further energy delivery to neighbouring regions of the material. Despite this, plasma generation allows for highly localized and intense energy deposition, making ablation very efficient [80].

2.3.5 Photodisruption

At high power densities, optical breakdown results in additional effects such as shockwave generation and cavitation bubbles along with plasma formation. These effects are influenced by the energy and duration of the laser pulse. Higher pulse energies create more energetic plasma, enhancing mechanical effects like shock waves that significantly affect tissue responses. Cavitation occurs when the laser focuses beneath the tissue, generating bubbles that dissolve into the surrounding tissue.

Plasma formation occurs during the pulse and lasts a few nanoseconds, expanding and triggering shock waves that evolve into acoustic waves after 30–50 nanoseconds. Cavitation typically starts 50–150 nanoseconds post-pulse, with bubbles expanding and collapsing in cycles over a few hundred microseconds.

During photodisruption, a focused laser creates a localised plasma leading to tissue ablation. This is often accompanied by shock waves and cavitation, which can affect nearby regions. Nanosecond pulses require higher energies and longer interaction times to reach the ionisation threshold, resulting in significant thermal spread and mechanical effects like shock waves. In contrast, picosecond and femtosecond pulses deliver high peak power with lower energies enabling plasma formation (via multiphoton and avalanche ionisation). These ultrashort pulses minimise heat diffusion and mechanical damage, making them ideal for precise ablation [80].

Understanding the laser tissue interaction is crucial for designing an efficient laser ablation setup. It also helps in selecting the appropriate laser to achieve precise ablation with minimal disruption and thermal effects. We developed a laser ablation setup with a ps laser having high spatial accuracy and less mechanical disruption, making it particularly suitable for biological samples, such as neuronal cells. Here, the ps laser is used, which produces less thermal effect than the ns laser and is more affordable than the fs laser. This makes the ps laser a suitable option for the ablation of extended objects.

2.4 Laser System and Ablation Setup

2.4.1 Laser system details

The custom-designed passively Q-switched, third harmonic Nd:YAG picosecond pulse laser (PowerChip PNV-M02510-100; Teem Photonics, Meylan, France) with wavelength 355 nm is used for the ablation. The compact and robust solid-state laser is designed to deliver high energy pulses of 25 μJ with a pulse duration of 350 ps. It can deliver pulses with a peak power of 70 kilowatts and a high repetition rate of up to 1 kHz. Nd:YAG laser head is mainly composed of a diode laser, laser cavity (saturable absorber, gain medium and mirrors), second harmonic generation (SHG) crystal, sum frequency generation (SFG) crystal and separators to isolate different generated wavelengths.

Neodymium (Nd) and chromium ion (Cr^{4+}) doped Yttrium Aluminum Garnet (YAG) crystals are the gain (lasing) medium and saturable absorber of the laser cavity [83]. The cavity is closed by mirrors at both ends and acts as an optical resonator. It bounces light back and forth to amplify the laser beam through stimulated emission. Optical pumping of the laser cavity is done through an 808 nm diode laser. Pump light is concentrated on the Nd:YAG crystal, where electrons of the gain medium are pumped from the ground state to the excited state through absorption. The electrons transfer from the excited level to a metastable state by the non-radiative process, building population inversion. The transition of electrons from the metastable state to the lower state is initiated by stimulated or spontaneous emission, leading to the emission of 1064 nm photons, equivalent to the energy gap [83]. A schematic of the laser used for ablation is shown in figure 2.3

The UV pulse laser is utilized for ablation, so it is essential to understand how these short, high-energy pulses are generated using Q-switching. Additionally, we will explore how the 355 nm wavelength is achieved through nonlinear optics. This will be discussed in the subsequent subsections.

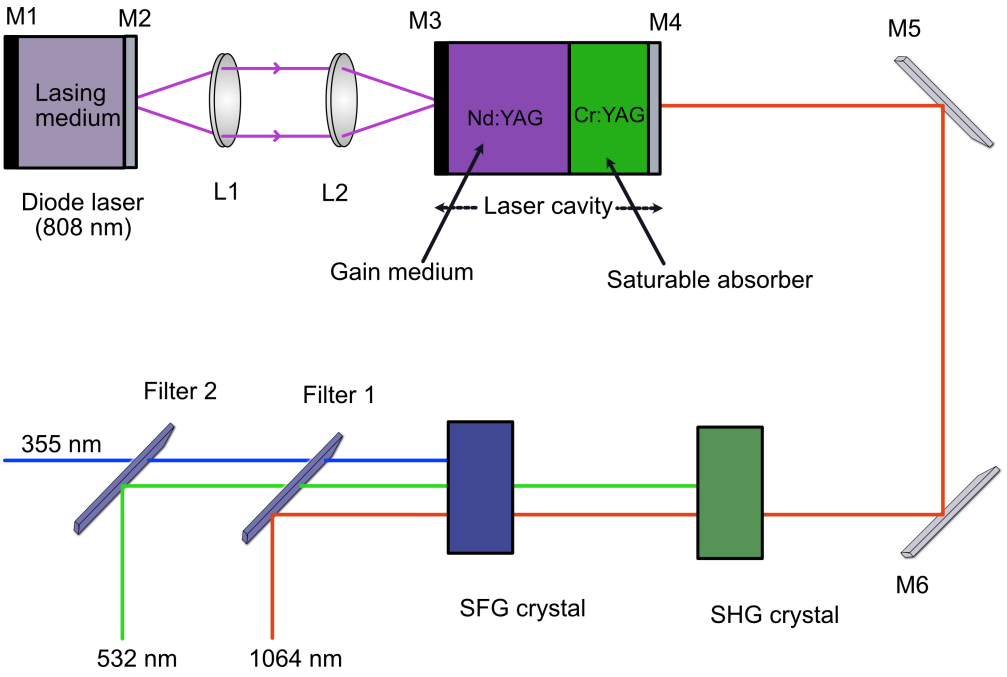

FIGURE 2.3: **Schematic of Laser used for ablation.** A diode laser is used for optical pumping of the Nd:YAG gain medium, with lenses L1 and L2 focusing the beam onto the Nd:YAG laser. Cr:YAG is used as a saturable absorber to produce laser pulses. The primary beam from the Nd:YAG laser has a wavelength of 1024 nm. Which further produces 532 nm and 355 nm using the second harmonic generation (SHG) crystal and the sum frequency generation (SFG) crystal. The two filters (separators) are used to get separate output for each wavelength.

2.4.2 Q-switching and pulse generation

In the case of continuous wave lasers, uniform power output is achieved whenever the gain becomes greater than the cavity losses. In contrast, a pulsed laser generates high-energy bursts of light in a very short time period. Q-switching (or Q-switch) is a laser operation mode that produces short duration, high energy pulses, one of the most effective methods of producing these types of pulses. It operates by modulating the quality factor (Q-factor) of the laser cavity, which is defined as the ratio of the energy stored in the laser cavity and the energy lost per cycle. Thus, a larger Q-factor corresponds to smaller

energy losses, leading to higher energy storage. In Q-switching, laser emission is suppressed at first, keeping the Q-factor low (high losses), and energy is allowed to accumulate in the gain medium. When the stored energy reaches a sufficiently high value, a sudden increase in the Q-factor leads to the emission of high-intensity laser pulses.

Q-switching can be classified mainly into two types-
(i) Active Q-switching. (ii) Passive Q-switching

(i) Active Q-Switching - In this method, an externally controlled modulator is employed in the laser cavity (resonator) to adjust the Q-factor. The modulator inhibits lasing by introducing losses, and at the appropriate moment, it is deactivated, resulting in a sudden release of energy. An example of an active Q-switch that can be tuned using external electronics is the electro-optical shutter.

(ii) Passive Q-Switching - In a passive Q-switch, the switching action is generated automatically by the optical nonlinearity of the utilized element. Saturable absorber such as Cr^{4+}:YAG is an example of passive Q-switch. No external components or electronics are needed to operate the passive Q-switch [84].

2.4.2.1 Saturable absorber

A saturable absorber (SA) is a nonlinear optical device that absorbs light below a threshold value but transmits light above it. When a cavity is pumped, a saturable absorber selectively absorbs low-intensity light initially, inhibiting photons from circulating in the

laser cavity. This inhibition blocks the light amplification by stimulated emission needed for laser output, resulting in an increase in energy stored in the gain medium. As energy builds up in the gain medium, there are increasingly more electrons in the higher energy level, and hence, the intensity of spontaneous emission increases. The doping concentration of Cr^{4+} ions is selected such that the saturation intensity threshold matches the intensity generated by spontaneous emission at the maximum energy capacity of the gain medium. Once the maximum gain is reached, saturation of the saturable absorber occurs, enabling photon oscillation within the cavity. This subsequently results in the rapid amplification of laser light through stimulated emission, causing a high peak intensity pulse of coherent infrared light (1064 nm) to be released through the partially transmitting mirror at the output of the laser. Following the pulse emission, the intensity within the cavity decreases, the absorber returns to its opaque state, and the energy accumulation in the gain medium resumes.

The intensity-dependent absorption coefficient α(I) is given by -

$$\alpha(I) = \frac{\alpha(0)}{1 + I/I_{sat}} \tag{2.1}$$

where $\alpha(0)$ is the low-intensity (small signal) absorption coefficient, I_{sat} is a saturation intensity (intensity at which absorption reduces significantly), and I is incident light intensity.

At low intensity (I $<<$ I_{sat}), the absorption is close to $\alpha(0)$, so most

of the light gets absorbed by the SA. As the intensity increases, more absorber molecules become excited, which reduces the overall absorption. At very high intensity (I >> I_{sat}), I/I_{sat} becomes large, reducing the term $\alpha(0)/(1 + I/I_{sat})$ making absorber transparent by reaching saturation [84, 85].

The passive Q-switch such as a saturable absorber is convenient to use because no complex electronics or control system is required from outside of the cavity.

2.4.3 Nonlinear optics

Nonlinear optics is the study of the interaction of light in nonlinear media, where the response of the material to an external electromagnetic field is nonlinear. In such situations, the polarization of the material is not linearly dependent on the electric field of incident light. These phenomena can only be observed at high intensities of light, such as produced by lasers.

In linear optics[1], the polarization $\vec{P}$ of a medium is directly proportional to the electric field $\vec{E}$ of the incident light -

$$\vec{P} = \epsilon_0 \chi^{(1)} \vec{E} \tag{2.2}$$

where ϵ_0 is the permittivity of free space and $\chi^{(1)}$ is the linear susceptibility of the medium.

[1]When a dielectric medium is subjected to an electric field, there will be a separation of bound charges that leads to induced dipoles. In the case of an electromagnetic field, an electric field oscillates rapidly, making dipoles oscillate in a harmonic range.

In nonlinear optics, when the interacting light reaches a certain intensity, such as from a laser source, the dipole oscillations will show anharmonic characteristics. The polarization (P) will depend on the electric field in a nonlinear manner resulting in higher-order terms.

$$\vec{P} = \epsilon_0 \chi^{(1)} \vec{E} + \epsilon_0 \chi^{(2)} \vec{E}^2 + \epsilon_0 \chi^{(3)} \vec{E}^3 + ... \tag{2.3}$$

$$\equiv \vec{P}^{(1)} + \vec{P}^{(2)} + \vec{P}^{(3)} + ... \tag{2.4}$$

The quantities $\chi^{(2)}$ and $\chi^{(3)}$ are known as the second- and third-order nonlinear optical susceptibilities, respectively.

From the above equation, $\vec{P}^{(2)} = \epsilon_0 \chi^{(2)} \vec{E}^2$ can be referred to as second-order non-linear polarization, which leads to effects like second-harmonic generation (SHG), difference-frequency generation (DFG), and sum-frequency generation (SFG). $\vec{P}^{(3)} = \epsilon_0 \chi^{(3)} \vec{E}^3$ represents third-order nonlinear polarization [86, 87].

2.4.3.1 Nonlinear optical processes for frequency generation

Second-order nonlinear optical interactions can only occur in non-centrosymmetric crystals, which do not exhibit inversion symmetry. Consider two light beams of frequencies ω_1 and ω_2, having field amplitudes $E_1 = E_{01} cos\omega_1 t$ and $E_2 = E_{02} cos\omega_2 t$. When they pass through a nonlinear medium, the resultant field will be

$$E_1 E_2 = E_{01} E_{02} cos(\omega_1 t) cos(\omega_1 t) \tag{2.5}$$

after solving,

$$E_1 E_2 = (1/2) E_{01} E_{02} [cos(\omega_1 + \omega_2 t)] + cos(\omega_1 - \omega_2 t)] \tag{2.6}$$

and from equations 2.3 and 2.4

$$\vec{P}^{(2)} \propto \vec{E}^2 \tag{2.7}$$

For SHG, two photons of the same frequency combine to form a new photon with double the frequency. So the conditions can be assumed as $\omega_1 = \omega_2$, and $E_0 = E_{01} = E_{02}$ and $E = E_1 = E_2$, then resultant will be $E^2 = \frac{{E_0}^2}{2}(1 + cos2\omega t)$. Here, it shows the generation of light with a frequency of twice of fundamental frequency. For example, in terms of wavelength, when light has a wavelength of 1064 nm passes through an LBO crystal, two photons of it combine to form a photon of 532nm.

For SFG, from equation 2.6, the term $(\omega_1 + \omega_2)$ deontes the sum of ω_1 and ω_1 of two different beams. When photons with wavelengths of 1064nm and 532nm pass through LBO crystal, produces photons with a wavelength of 355 nm in the ultraviolet range [86, 87].

2.4.4 Laser ablation setup

A schematic illustration and photograph of the laser ablation setup are displayed in figure (2.4) and (2.5), respectively. A Nd:YAG pulsed laser with a wavelength of 355 nm is used in our setup to

perform precise ablation of axons. The laser operates in the fundamental transverse electromagnetic mode (TEM_{00}), which produces a symmetrical Gaussian beam profile. This well-defined beam concentrates energy at a tiny focal point (at the centre), making it ideal for ablation applications. The output beam from the laser is linearly polarized and first passes through a polarizer followed by a quarter-wave plate (QWP). The QWP is oriented at 45° relative to the polarizer and this arrangement works as an optical isolator. The polarizer passes linearly polarized light, and the quarter-wave plate converts it into circularly polarized light. Upon reflecting from mirrors, the light changes its handedness and becomes circularly polarized in the opposite direction. When it passes back through the quarter-wave plate, it becomes linearly polarized but now aligned perpendicular to the polarizer. Thus, it is blocked, preventing back-reflected light from re-entering the laser cavity.

The polariser acts as an intensity attenuator. The attenuation is governed by Malus's Law ($I = I_0 cos^2\theta$), which states that the transmitted intensity (I) depends on the angle (θ) between the direction of polarization of light and the transmission axis of a polarizer. The precise control of the laser intensity is crucial because different biological samples, ranging from individual cells to tissues, have varying thresholds for ablation.

After passing through the attenuator, the laser beam is steered using mirrors—either a silver-coated mirror on a fused silica substrate

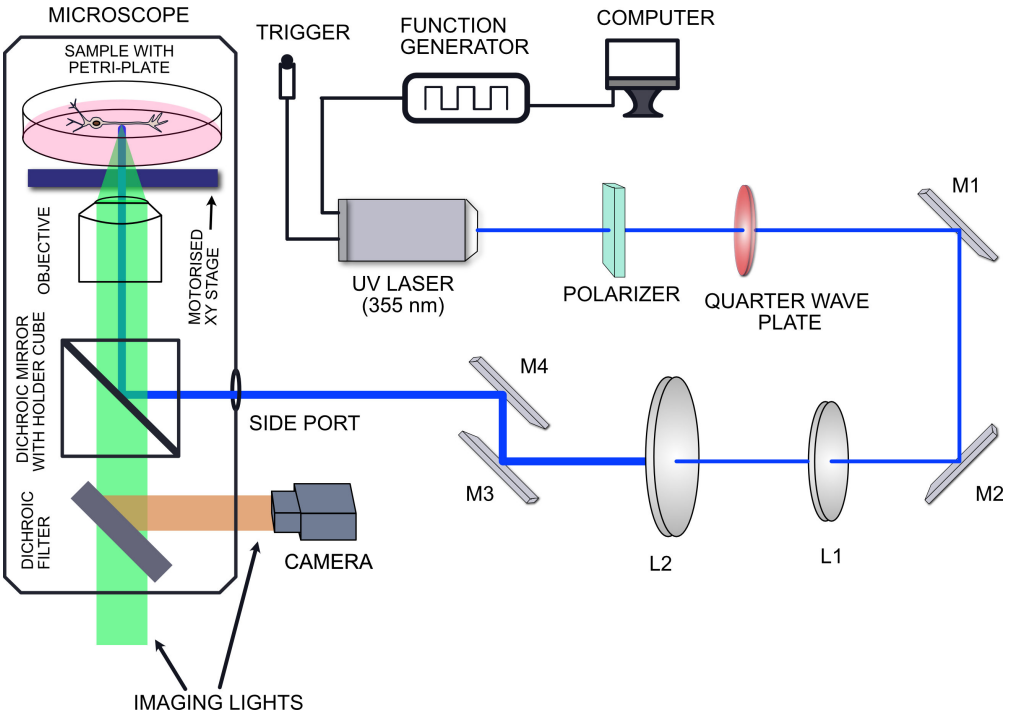

FIGURE 2.4: **Schematic of laser ablation setup.** UV pulsed laser can be operated either with a hand trigger or a function generator connected to a computer. As one unit, the polariser and quarter-wave plate act as an optical isolator and intensity attenuator. M1, M2, M3, and M4 are mirrors that direct the laser light to the sample through the side port of the microscope. L1 and L2 are lenses that act as a beam expander. The dichroic mirror is mounted in the microscope fluorescence turret using a custom designed 90° rotated holder that reflects the laser light to the sample. The microscope illumination path (when used in fluorescence mode) is shown in green, representing the incident light directed toward the sample. The reflected light from the sample is shown in yellow and is collected using a camera. A dichroic filter separates transmitted and reflected light based on the wavelength. Phase contrast imaging is also possible by using a phase ring in the bright field illumination path and a phase objective.

(PF10-03-P01, Thorlabs) or a UV-enhanced aluminium-coated mirror on fused silica (#39-209, Edmund Optics). The beam then enters a Keplerian beam expander, which is made up of two lenses with positive focal lengths (f_1 = 50 mm and f_2 =200 mm). The lenses L1 (LA1131-A, Thorlabs) and L2 (LA1708-A, Thorlabs) are plano-convex and have an anti-reflection coating optimised for 350–700nm. The distance between the lenses is equal to the sum of their focal

lengths, which allows for the desired magnification (M = 4x) of the beam. This expansion ensures that the beam fills the back aperture of the objective lens, resulting in a sharp focus on the sample. The expanded beam then enters a beam steering system consisting of two mirrors that can steer the laser beam along both horizontal and vertical axes. After the steering system, the beam enters the side port of a SP8 confocal microscope (DMI6000, Leica), where it is reflected at a 90° angle by a dichroic mirror (T387lp-UF3, Chroma) mounted at 45° in a custom-made filter cube. The dichroic mirror is designed to reflect UV laser light while transmitting visible light, enabling simultaneous imaging and ablation for real-time visualization.

Laser focusing and sample magnification are achieved through objective lenses. Depending on the application, a 40× dry objective (NA 0.75, Leica or Olympus) and a 63× oil immersion objective (NA 1.3, Leica) are used to perform ablation experiments. The objective tightly focuses the laser beam on the sample, creating a high power density required for localized ablation.

The microscope is equipped with a motorized stage controlled via a joystick using LASX software. This allows precise positioning of the sample, typically a plastic petri plate with a glass-bottom coverslip containing neurons. To maintain physiological conditions, the sample is kept at 37 ± 0.1°C using a microscope incubation chamber (Okolab).

A computer-operated external function generator via PC-LAB2000

software (Velleman Instruments) is used to control the pulse repetition rate, waveform, amplitude, and duty cycle of the laser, providing further flexibility and optimization for ablation parameters. Additionally, a handheld trigger can also be used to generate a single pulse. With this setup, ablation can be performed using widefield, phase contrast and confocal microscopy.

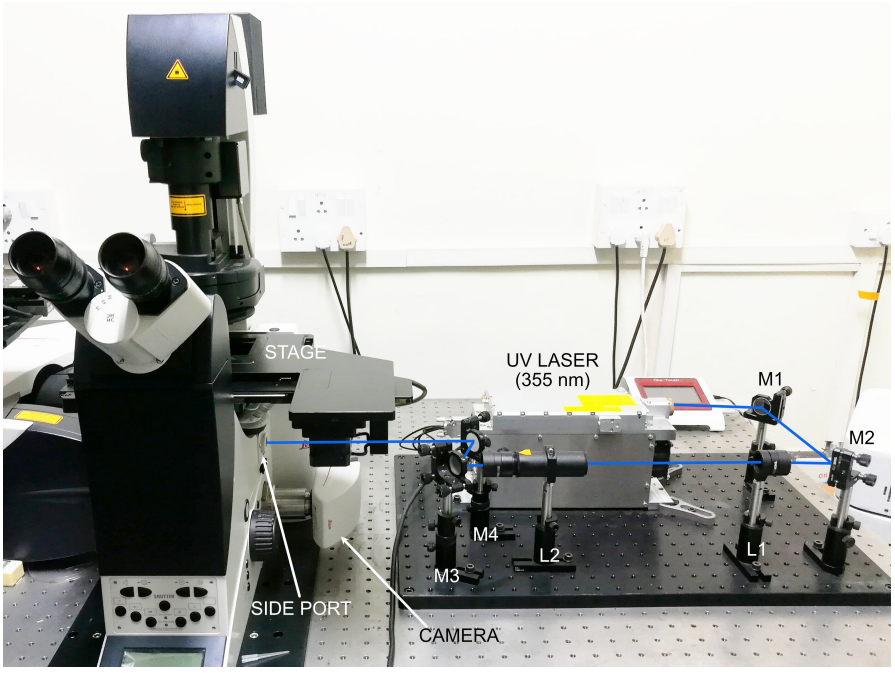

FIGURE 2.5: **Photograph of the laser ablation setup.** A laser is used to ablate the axons to investigate their mechanical properties. A microscope is used to image the sample before, during and after ablation.

2.5 Safety precautions for using the laser ablation setup

A 355 nm pulsed UV laser utilized for ablation is a Class 4 laser because of its high power. Such a laser can cause serious damage to the eyes and skin, including damage from scattered or reflected

beams. Therefore, it is essential to strictly follow safety precautions to significantly reduce the risks involved.

(1) Always wear laser safety goggles rated for 355 nm when the laser is on to protect your eyes.

(2) Ensure the setup and all light paths are adequately covered to prevent accidental exposure to laser light.

(3) Place warning signs near the laser and at the entry point of the room to alert individuals when the laser is on.

(4) Limit access to people not wearing proper safety goggles to reduce the chances of accidents.

(5) Avoid positioning unwanted reflective surfaces close to any exposed area along the beam path to minimize the chances of hazardous reflections.

(6) Do not wear items with reflective surfaces, such as watches, long necklaces, or rings, while aligning the laser. Additionally, avoid aligning the beam with your eyes at the same level as the laser beam.

(7) Ensure that all personnel involved in the laser ablation setup receive proper training before using it.

2.6 Characterisation of Laser ablation setup

In the previous section, we described the Laser ablation setup. This setup can perturb living samples, but that disturbance should be

confined locally. As we have discussed in the subsection 2.3.5, the laser may cause mechanical damage upon ablation, which includes the generation of shock waves. We also mentioned that picosecond lasers are a cost-effective option at a slightly compromised extent of damage, potentially admissible for long objects like axons. So, to evaluate the extent of damage caused to a sample, various methods are used to characterize it before conducting the experiments. Although this setup can be used to perform experiments with many cell types and tissues, for thesis work, we aim to use it to ablate axons. So all the characterisation is done in such a way that we can do such ablation experiments.

2.6.1 Impact of shock waves on bead bed after ablation

To investigate how the shock wave influences the sample, prepare a bed of polystyrene beads of size 1 μm in Milli-Q water. Focus on the bead bed and perform laser ablation. Then, observe the response of the neighbouring beads by analysing the difference between pre- and post-ablation images. Here, we attempted to ablate a bead to mimic conditions where material is present. The pre- and post-ablation images of the bead bed are shown in Figure 2.6a and 2.6b, respectively. The difference image, highlighting the displacement caused by the shock wave, is shown in Figure 2.6c. We estimated the extent of the affected region by measuring its diameter, assuming a circular profile. A total of n = 11 ablations were performed on the

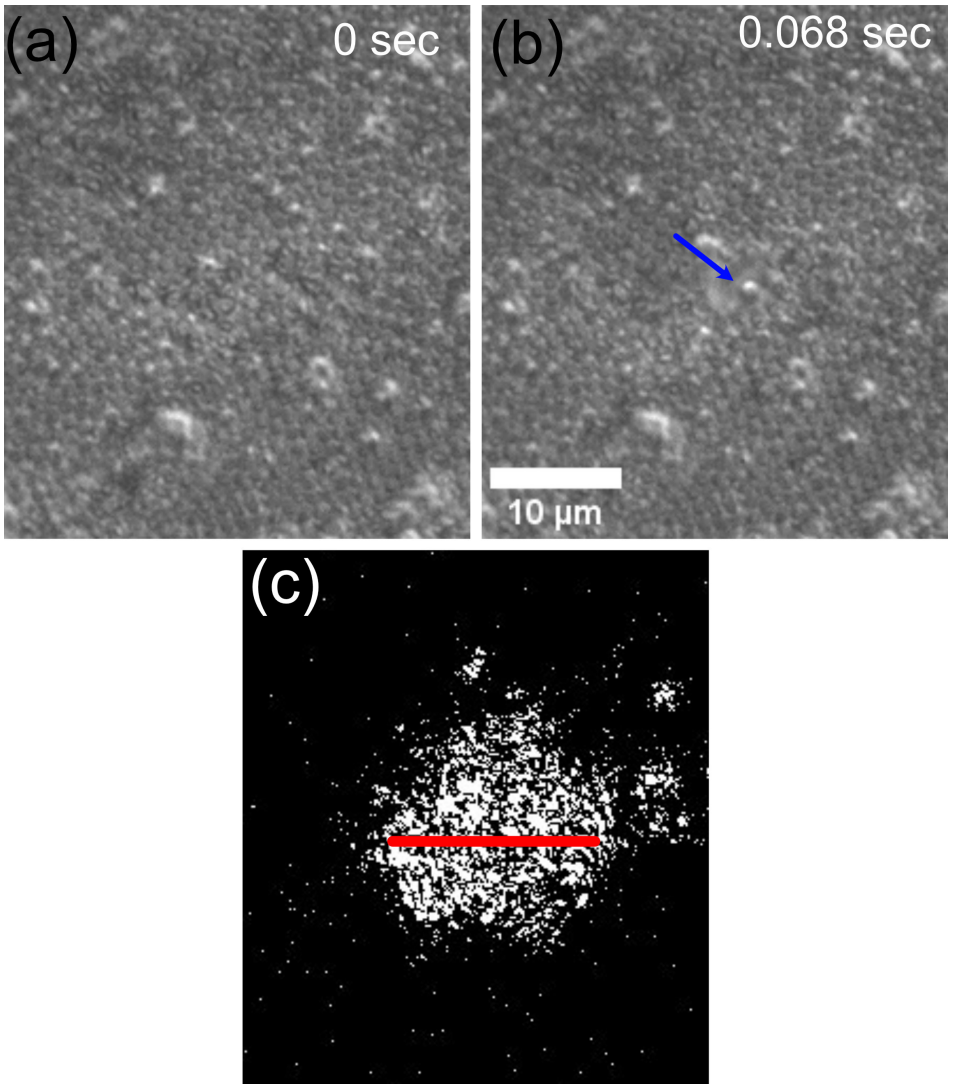

FIGURE 2.6: The bead bed images before and after ablation are shown in (a) and (b), respectively. The blue arrow indicates the ablation site. The difference between images (a) and (b) is shown in (c), where the bright region highlights the area affected by the shock wave. The red line represents the measured length used to estimate the extent of the impact. The scale bar represents 10 μm.

bead bed, and the resulting distribution of affected region lengths is summarised in the box plot shown in Figure 2.7. As can be seen, we observe a mean distance of about 20 microns for the region affected by the shock wave. Note that this does not necessarily mean that the ablation happened over this distance, as this is indicative of mechanical effects, which may or may not damage the axon. For this reason, we also perform another test using axons as discussed in

the next subsection 2.6.2.

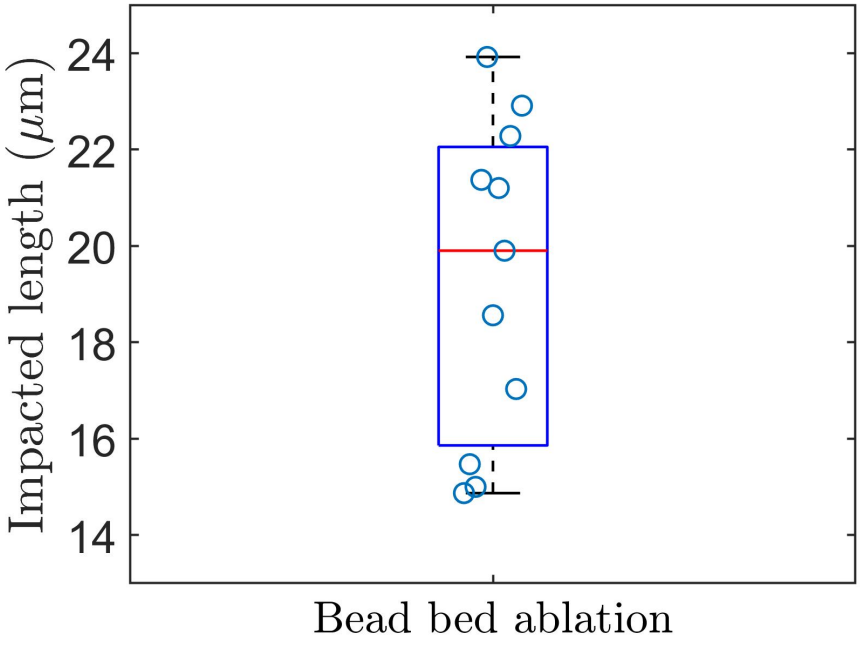

FIGURE 2.7: Box plot of the affected length due to the shock wave generated by laser ablation on the bead bed.

2.6.2 Experiments with fixed axons

In this thesis, we performed laser ablation on axons and analyzed the retraction responses. We aimed to understand whether the responses of axons after ablation were genuinely due to the axons themselves or if they were caused by disruption from the laser. To check that, experiments were conducted using chemically fixed axons to evaluate the spatial extent and effectiveness of laser ablation.

The steps for the cell fixing protocol are outlined below -

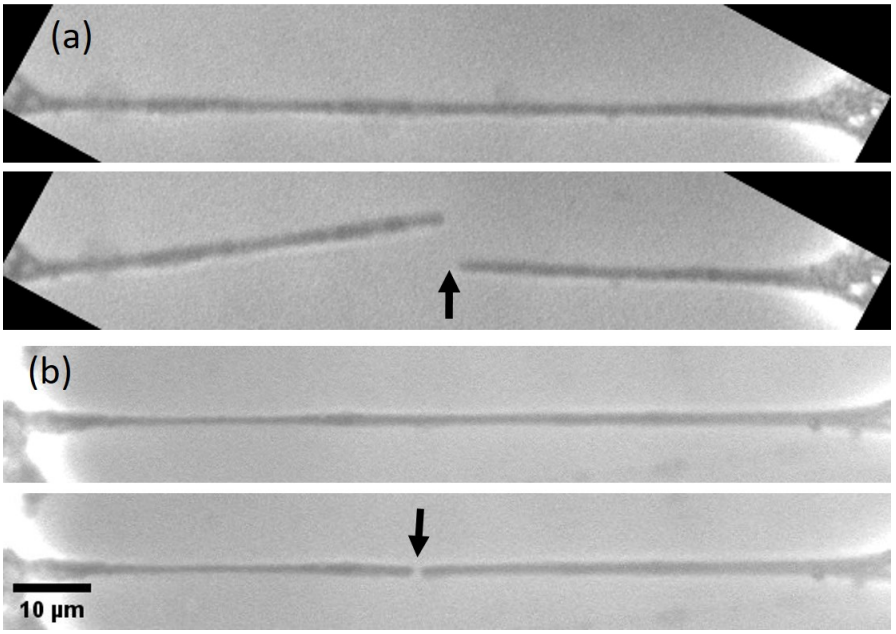

FIGURE 2.8: **Images of axons after fixation**. The pre- and post-ablation images of (a) full ablation and (b) partial ablation (explained in detail later in the next chapter 3). Bold black arrows indicate the cut sites.

(1) Carefully remove the culture media and gently add a fixative solution to completely cover them for 10 minutes at room temperature. This process will immobilise cellular structures. The 4% paraformaldehyde (Electron Microscopy Sciences 15710) is used as a fixative buffer.

(2) Remove the fixative and rinse the cells with phosphate-buffered saline (PBS) three times for 5 minutes each to remove any residual fixative.

(3) After the final wash, keep the cells in PBS at 4°C, or perform ablation experiments.

After full ablation and partial ablations, two types of analyses can be done-

1. Measure the contour length of axonal segments over time to determine whether the retraction observed in control cells is influenced by the laser treatment.

2. Assess the length and volume ejected by the laser

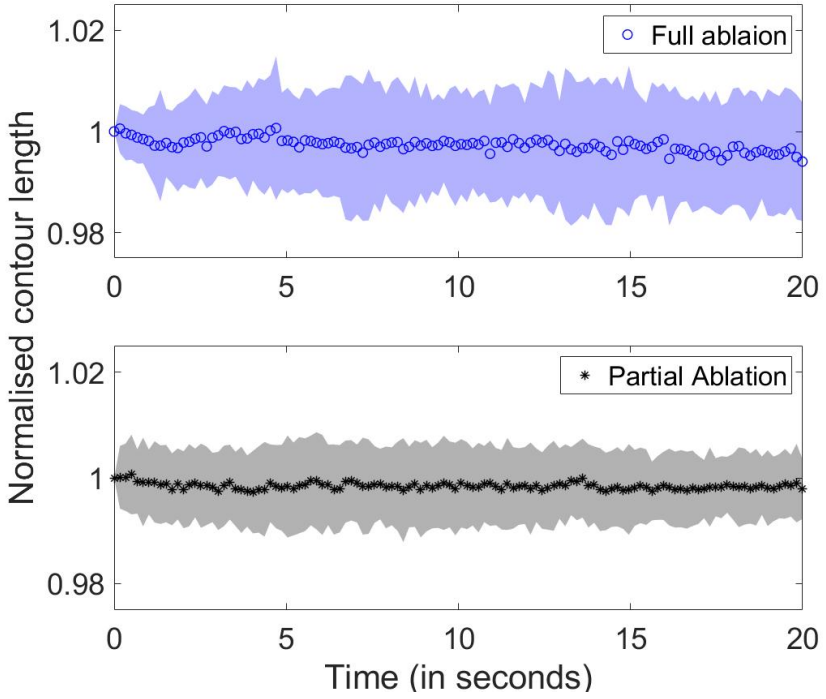

FIGURE 2.9: The average of normalised contour lengths of axonal segments vs time plot is shown. (a) After full ablation (n1 = 16 axons or 32 segments) (b) After Partial ablation (n2 = 18 axons or 36 segments). The averages are calculated using n1 for full ablation and n2 for partial ablation.

When axons are fully or partially ablated after fixation, there is no significant retraction observed in Figure (2.8). Even though axons can move sidewise, possibly due to shock waves, there is no retraction along the axonal axis or extended damage. The contour length over time did not change after ablation, as shown in Figure 2.9. This indicates that the ablation occurs in a very confined region of around 1.5 to 2.5 microns (see figure 2.10), but the axonal shaft may

experience lateral forces which do not result in observable damage. As we use axons that are 80 to 150 μm long for our experiments, a laser-induced damage of a few microns can be treated as a local damage.

Additionally, axonal length and volume after ablation may indicate the extent of axonal damage. The length ejected by the laser by measuring the pre-ablation axonal contour length (L_0) and post-ablation axonal segment lengths (L_1 and L_2). Along with the ejected length, the axonal volume can be estimated after evaluating the diameters of axonal segments. The box plot of length and volume values for complete and partial ablation is shown in figure (2.10) and (2.11), respectively. The volume values may vary because they depend on both the length ejected along the axon and the diameter, which can differ across experiments. In both types of experiments, the diameter is not constant, which contributes to the variability observed in the box plot shown in the figure 2.11.

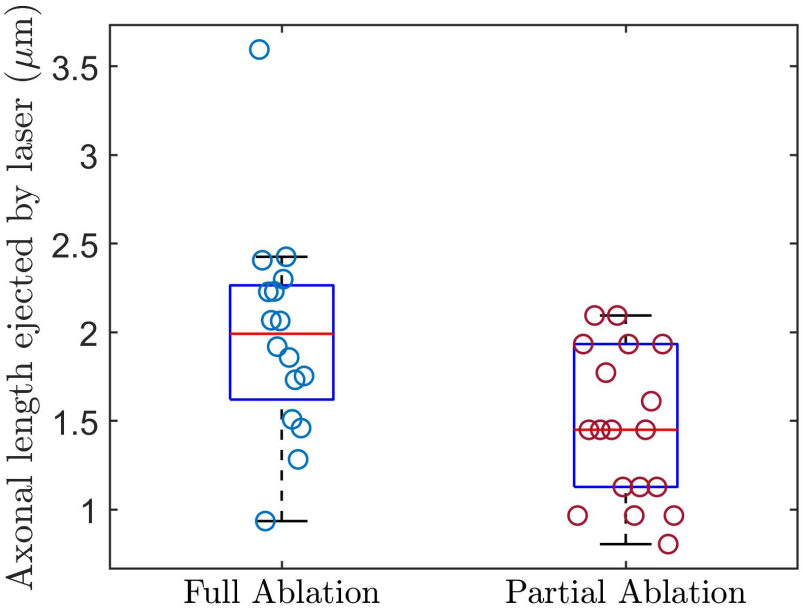

FIGURE 2.10: The boxplot of axonal lengths ejected by laser during (a) Full ablation (b) Partial ablation

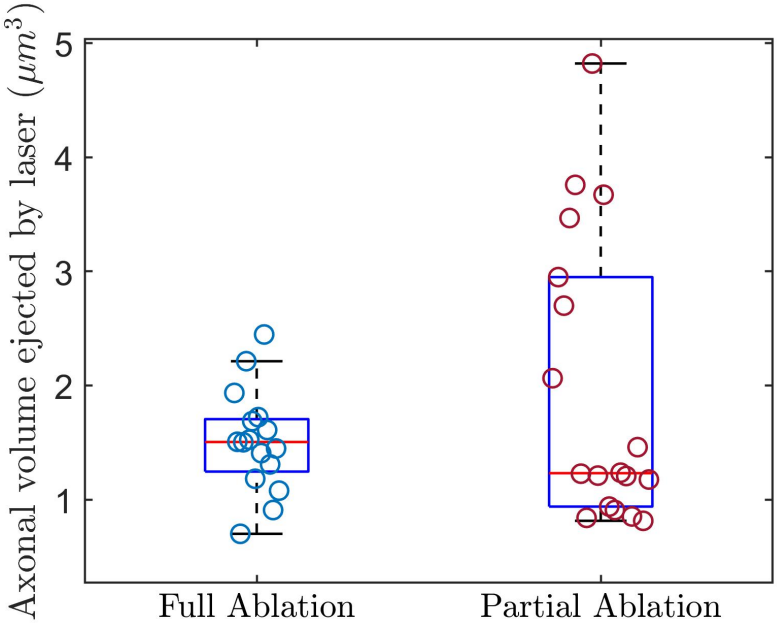

FIGURE 2.11: The boxplot of axonal volumes ejected by laser during (a) Full ablation (b) Partial ablation

Chapter 3

The role of cytoskeletal components in axonal retraction

3.1 Introduction

Laser ablation is a versatile tool that enables precise manipulation and investigation of the mechanical responses of tissues, cells and their components, including the cytoskeleton. In Drosophila embryos, laser ablation is employed to sever individual cell junctions, and the subsequent tissue recoil is analysed to comprehend the mechanical forces involved during morphogenesis [88]. Gonzalez and team used laser ablation to demonstrate that mechanical tension influences the dynamics of myosin II in rearranging (intercalating) Drosophila cells by stabilising it at cell junctions. When tension is reduced, myosin II rapidly disassembles. This suggests a link among tension, myosin II localisation and coordinated cell rearrangement [89]. Similarly, Rauzi and his team utilise laser ablation to uncover

anisotropic cortical tension, directed by myosin II, which guides cell rearrangement during tissue extension [77]. Together, these studies emphasise that tension acts as a product and a regulator of morphogenetic forces. At the single-cell level, laser ablation is used to remove the mitotic spindle and investigate chromosome movement and the generation of force during cell division. For example, the disruption of spindle microtubules in PtK_1 (kangaroo rat kidney) cells has shown that the forces exerted on chromosomes are facilitated by kinetochore fibres [90]. This technique has also been utilised to study the mechanical properties of the actomyosin cortex in living cells. By making precise laser cuts in the cortical layer, recoil velocity and deformation of the cortex are evaluated, providing quantitative data on cortical tension and elasticity [91]. Botvinick and team applied a picosecond laser ablation technique to precisely sever individual microtubules in living cells. This controlled ablation allows them to study microtubule dynamics with minimal collateral damage to surrounding structures [92]. Sanjay Kumar et al. used laser ablation to ablate individual stress fibres in living cells. This technique allows the authors to observe the retraction dynamics of the cut fibres, revealing that they behave in a viscoelastic manner—initial rapid recoil followed by slower relaxation. These findings show that stress fibres store mechanical tension and contribute to the overall cell shape [75].

Understanding how intracellular elements, such as stress fibres, manage and distribute tension establishes a mechanical basis for examining analogous mechanisms in neurons, like axonal retraction. Like stress fibres, axons are also under tension, which is reported by many studies [57, 58]. Investigating axonal retraction after laser ablation may provide essential insights about axonal mechanics. For example, by exploring how the stabilisation and destabilisation of cytoskeleton components affect axonal retraction. Moreover, such studies can reveal how structural integrity is maintained or lost during neuronal injury.

3.2 Previous works on axonal transection and retraction

Axonal retraction following transection/injury is thought to contribute significantly to the breakdown of neural networks leading to serious outcomes. However, the underlying mechanisms driving axon retraction that regulate this process are still not fully understood. Various experimental methods have been employed to deliver controlled damage to neural cells in order to investigate their retraction responses. These techniques include microknives or blades [93, 94], atomic force microscope (AFM) tip [4], glass micropipettes [3], and laser-based microsurgery [76]. They allow for the perturbation of axons, simulating injury and enabling the observation of the resulting cellular responses. The immediate separation of axonal segments

cut by a cataract knife was also observed, along with mitochondrial swelling and deformation near the transection site, likely resulting from direct mechanical damage [93].

Shao et al. demonstrated that the retraction of a transected axon induced by an atomic force microscope (AFM) tip is driven by intrinsic axonal tension and occurs in opposition to both neuron-substrate adhesion and the viscous resistance of the cell [4]. In experiments involving adherent axons, they found that strong attachment to the substrate could halt axon retraction, but retraction could be reinitiated by a second transection, although with reduced amplitude. Additionally, disrupting the actin cytoskeleton or reducing cell-substrate adhesion significantly affected retraction dynamics. Weakening the actin cytoskeleton likely decreases axonal tension, resulting in slower retraction, while reduced adhesion (due to diminished bond and energy density) leads to enhanced retraction [4].

In another study, Shao et al. used a sharp AFM tip to gently lift axons off the substrate, creating floating axons, and then transected them to trigger axon beading in a precisely controlled manner. They reported that axon diameter and cytoskeletal integrity influence the wavelength between beads, with thinner axons and disrupted actin cytoskeletons resulting in shorter beading wavelengths. For adherent axons, they observed that beading often initiates at regions with strong substrate adhesion, underscoring the role of adhesion in the initiation of beading [95].

Gallo has demonstrated that actomyosin contractility is responsible for axon retraction caused by severing. The use of Latrunculin A (Lat A) to depolymerise actin filaments prevented this retraction, indicating that actin filaments are essential for severing-induced axon retraction. Additionally, directly inhibiting myosin II with Blebbistatin reduced axon retraction in response to severing [3].

Axon retraction is not only a result of direct physical cuts but can also be triggered by mechanical stress. When a compressive force exceeding a critical limit is applied to the growth cone, it may initiate axonal retraction [96]. Additionally, Baas's group studied axonal retraction, which leaves a thin trailing remnant induced by the nitric oxide donor, NOC-7. They demonstrated that the microtubules reconfigured themselves into coiling and sinusoidal arrays to accommodate the shortening of the axon. Additionally, they found no loss of microtubule levels during the early stages of retraction. However, they observed significant microtubule depolymerisation during axonal retraction in nocodazole-treated cells. In contrast, axons treated with Taxol exhibited axonal retraction in response to NOC-7 without any loss of microtubules [97].

3.3 Axonal Retraction after Laser Ablation: Mechanical and Cytoskeletal Insights

Mechanical transection methods, such as microknives or micropipettes, often cause physical pulling on axons, leading to imprecise injury and

complicating the interpretation of retraction dynamics. In contrast, laser-based axonal ablation allows for clean, localised cuts with micrometre precision, avoiding unwanted mechanical artefacts. This makes it an ideal tool for studying axonal mechanics and injury responses.

Many prior studies have performed retraction experiments on axons adhered to the substrate, where surface interactions can introduce biases that affect the retraction behaviour. To minimise these effects, we focus on ablating axons that are floating—attached only at their two extremities (shown in the figure 3.1)—and analyse their mechanical responses to isolate intrinsic cytoskeletal properties from adhesion-dependent effects. To confirm whether an axon is detached from the surface, the microscope stage is gently tapped. If the axon is adhered, it remains stationary; if it is floating, deflection can be observed on the computer screen via the camera. Additionally, debris on the surface is used as a reference to determine whether the axon is lifted away from the substrate.

Axons are known to exist in a state of pre-existing tension, and any perturbation, such as ablation, leads to changes in tension due to structural reorganisation. We aim to understand how this structural organisation, particularly involving the cytoskeleton, influences the axon's mechanical behaviour during retraction. To this end, axons were treated with various pharmacological agents that either destabilise or stabilise the cytoskeleton and then fully and partially

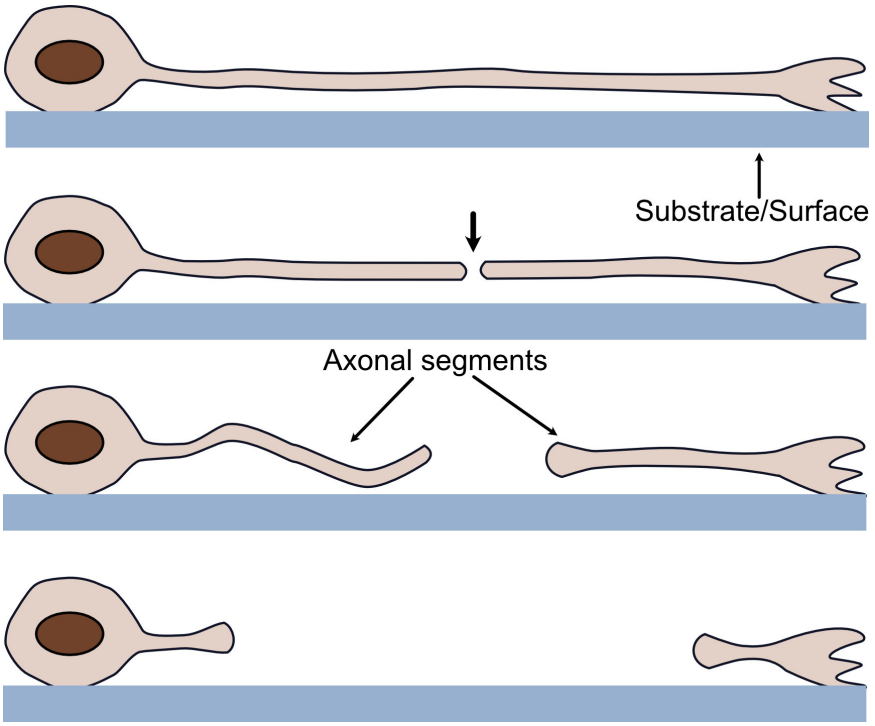

FIGURE 3.1: The neuron is anchored at both ends, but the axonal part is detached from the substrate. The bold black arrow indicates the point of ablation. Following ablation, the axonal segments exhibit buckling and retraction.

transected using a UV pulsed laser. Retraction was quantified using length retraction vs time plots and the ratio of contour length to end-to-end distance vs time plots as a measure of post-ablation buckling.

In our experiments, picosecond laser cuts produced retraction on both sides of the axon. We also observed secondary responses such as buckling and twisting, highlighting the role of cytoskeletal forces in axonal shape transformations. In full ablation, both the membrane and cytoskeletal components are ablated, whereas in partial ablation, only the cytoskeleton is disrupted while the membrane remains intact, resulting in long-range cytoskeletal retraction.

3.4 Pharmacological agents used for experiments

To study the role of the axonal cytoskeleton in laser ablation-induced retraction, neurons were treated with 30μM Blebbistain (Blebbi)(B0560, Sigma-Aldrich) for 20 min to inhibit myosin II activity, 1μM Latrunculin-A (Lat A) (L5163, Sigma-Aldrich) for 10 min to destabilise actin filaments, 16.67μM Nocodazole (Noco) (M1404, Sigma-Aldrich) for 30 min to destabilise microtubules, 10μM Taxol (T7402, Sigma-Aldrich) for 30 min to stabilise microtubules and 5μM Jasplakinolide (Jasp) (J7473, Thermo Fisher Scientific) for 30 min to stabilise actin filaments. All the drugs were dissolved in dimethyl sulfoxide (DMSO) (D84818-50ml, Sigma-Aldrich) with a final DMSO concentration kept below 1% v/v. Control experiments were performed with less than 1% DMSO. Known responses of chick fibroblasts are used to test the drug's efficacy before using them on neurons.

3.5 Results

3.5.1 Retraction responses of axons after full ablation

Building on the evidence that axonal retraction responses are influenced by cytoskeletal components, we conducted full ablations on control axons and those treated with specific pharmacological agents

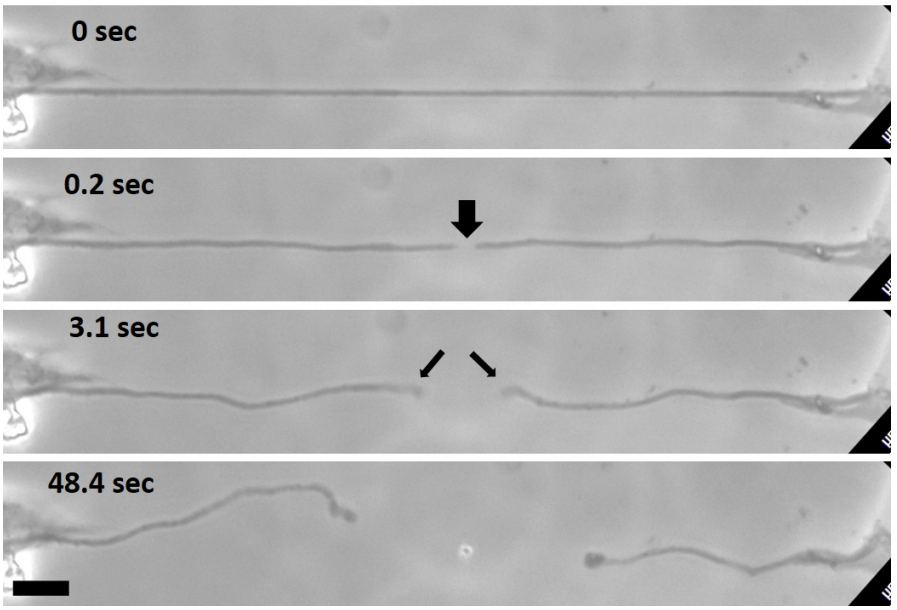

FIGURE 3.2: The sequence of images for full ablation of control axons is shown here. The bold black arrow indicates the point of ablation, and the thin arrows indicate the retracting segments. The scale bar is 10μm.

that target actin and microtubule dynamics. We quantitatively analysed retraction behaviour—specifically, contour length—to uncover how different cytoskeletal elements contribute to or resist retraction forces following injury. This may further indicate which cytoskeletal component or drug is responsible for stabilising the axon after transection (or injury). In the case of full ablation, axons produce two separate segments after severing and exhibit retraction and buckling (discussed in detail in subsection 3.5.3), as shown in Figure 3.1 and Figure 3.2. However, in some cases (e.g., when treated with Taxol), axons did not retract significantly after full ablation, as shown in Figure 3.3.

As we grow neurons in a petri plate with viscous media containing methylcellulose, which helps neurons adhere more stably during growth. The medium was replaced with methylcellulose-free media

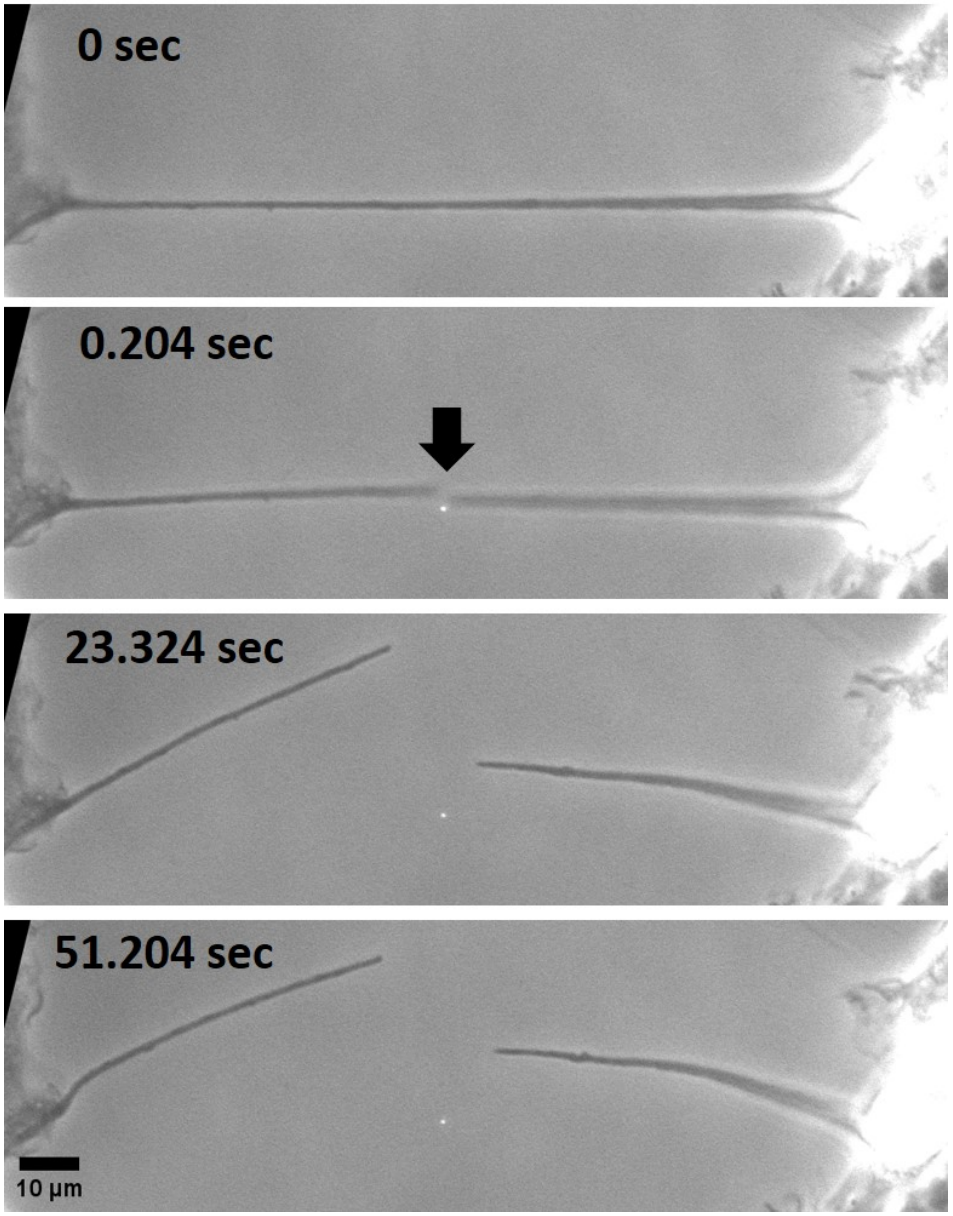

FIGURE 3.3: A series of images for full ablation of Taxol-treated axons is shown here. The bold black arrow indicates the point of ablation. In the third image from the top, the segments do not retract in the axonal axis direction but move away from the ablation point.

30 minutes before the experiments to reduce surface adhesion and allow axonal shafts to float more freely (shown in the figure 3.1). The imaging of axonal retraction following full ablation was performed at 15 frames per second, and the data (for control) is shown

in Fig 3.4a. The time duration in the plot varied across axonal segments, and some gaps appeared in the data. During retraction, the axonal segment briefly went out of focus, and the analysis code could not process those frames. When the segment came back into focus, contour length measurements resumed, resulting in the segmented appearance of the curve.

The flowchart of the algorithm used to extract the y-positions of axons during retraction and to calculate the contour length is provided in Appendix A. Due to cell-to-cell variability, averaging was performed only up to the time point where sufficient data were available. The variability in retraction dynamics between axons is most likely due to differences in internal structure and diameter. Axon length may also play a role, although lengths were taken within 80–150 μm. Figures 3.4b,c,d show the retraction response for axons treated with specific cytoskeleton perturbing drugs. The pharmacological agents, concentration and waiting time used for ablation experiments are mentioned in the section 3.4.

DMSO (control)-treated cells were used for full ablation, and we observed retraction of axonal segments, as shown in the figure 3.4a. After performing control experiments, we proceeded to explore the effect of cytoskeletal drugs on axon retraction post-ablation. First, axons were treated with blebbistatin, which inhibits the activity of myosin motors. After ablation, the retraction rate was slower compared to the control. The contour length analysis is shown in the figure 3.4b. Next, axons were treated with Latrunculin A, which

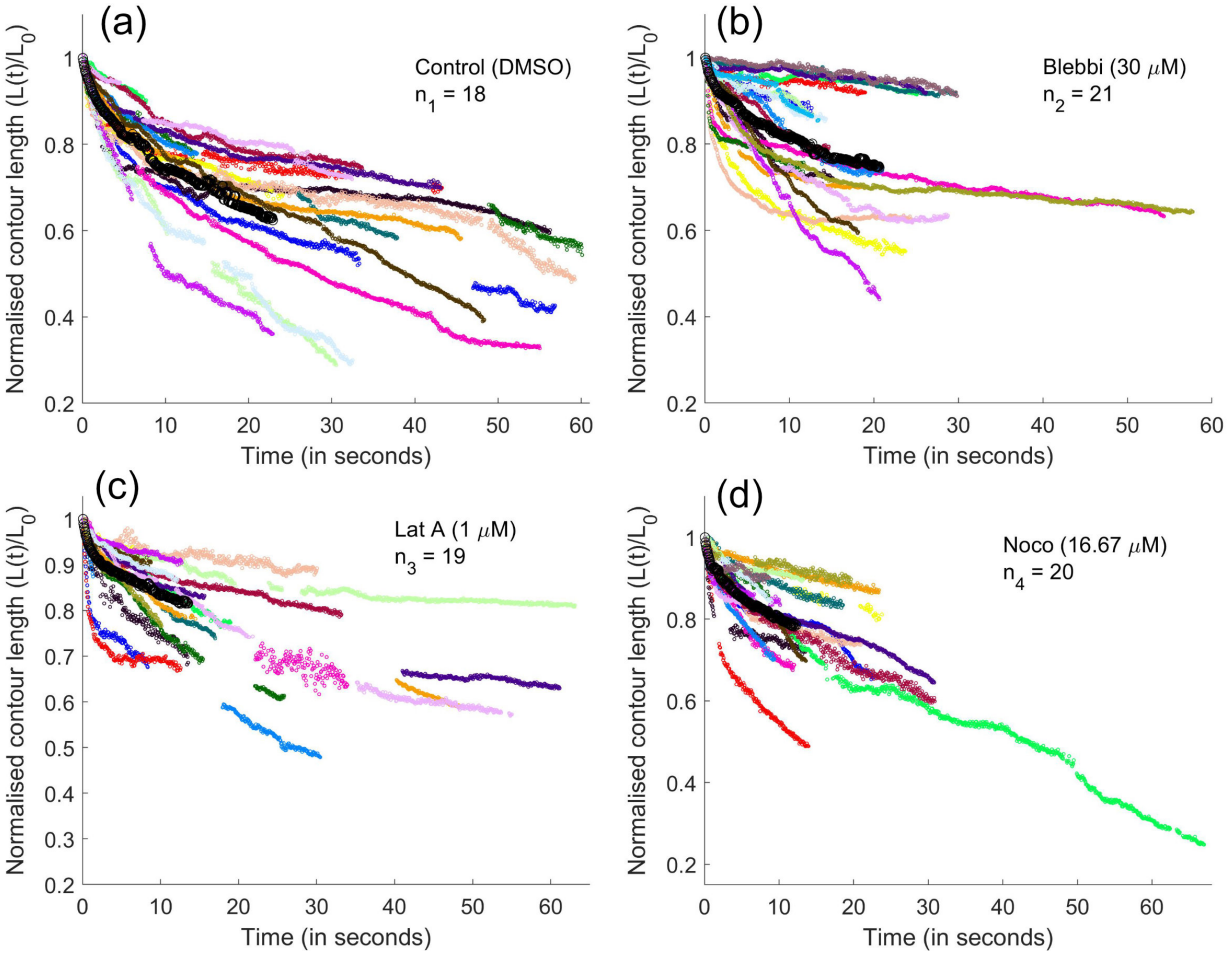

FIGURE 3.4: The normalised contour length vs time plot is shown in (a) for Control (DMSO), (b) Blebbistatin (c) Latrunculin A and (d) Nocodazole treated axons. The bold black circle represents the average plot for each treatment. The other colored curves with smaller circle markers represent the individual axonal segment contour length plots. Normalisation was done by dividing the contour length at each time point, L(t), by the initial contour length just after ablation (L_0). Gaps in the individual axonal contour length data occur due to extreme out-of-focus conditions, and these points were removed to avoid distorting the average. Some axonal segments went out of focus early, making further analysis unreliable, so the analysis was stopped at that stage. The drug names are mentioned in the plots, and n_1, n_2, n_3, and n_4 represent the number of axonal segments. The data was obtained using multiple embryos.

depolymerises filamentous actin. After ablation, these axons exhibited slower retraction compared to the control. The contour length is shown in the figure 3.4c. Nocodazole-treated axons, in which microtubules were depolymerised, too, exhibited slower retraction following full ablation compared to controls. The contour length

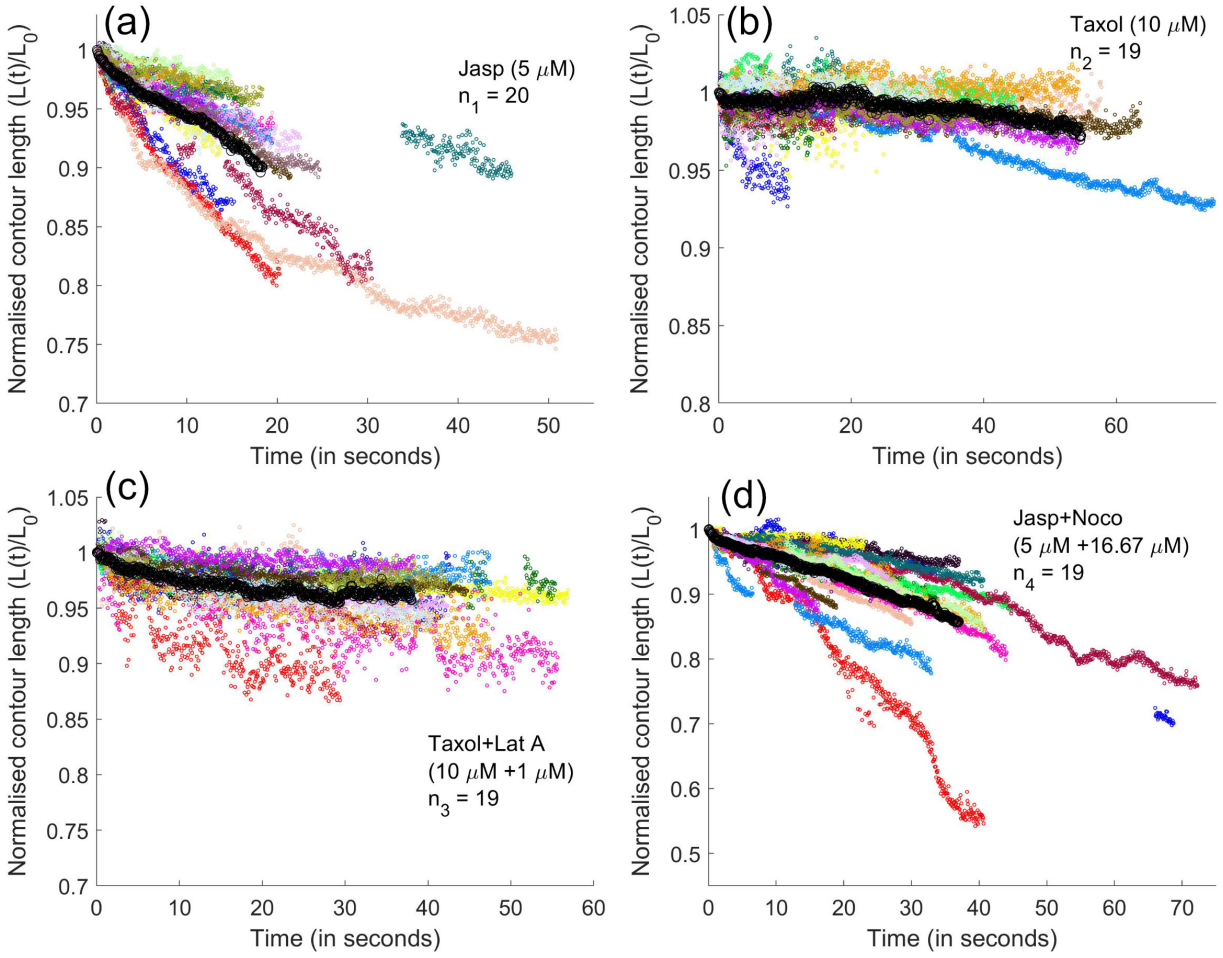

FIGURE 3.5: The plots of normalised contour length versus time for (a) Jasplakinolide, (b) Taxol, (c) Taxol + Latrunculin A, and (d) Jasplakinolide + Nocodazole-treated axons are shown. The bold black circle indicates the average plots. The additional colored curves with smaller circle markers represent the contour length plots of individual axonal segments. The names of the drugs are indicated in the plots, and n_1, n_2, n_3, and n_4 denote the number of axonal segments used in each condition.

measurement is shown in the figure 3.4d.

Next, we exposed neurons to drugs that stabilise cytoskeletal elements. Jasplakinolide was used to stabilise filamentous actin in axons. Following full ablation, these axons showed reduced retraction relative to controls. The corresponding contour length data is shown in the figure 3.5a. Taxol-treated axons, with stabilised microtubules, showed a significantly reduced retraction rate following full ablation

compared to controls. Corresponding contour length data is shown in the figure 3.5b.

After examining the effects of individual cytoskeletal components using treatments that target either actin (e.g., Latrunculin A, Jasplakinolide) or microtubules (e.g., Nocodazole, Taxol), the contributions of each cytoskeletal component to axonal retraction dynamics could be isolated. However, cytoskeletal elements do not operate independently in neurons. Periodic actin structures play a crucial role in maintaining the integrity of microtubule networks within axons. Disruption of the actin cytoskeleton leads to the formation of gaps in microtubule bundles, reduced microtubule polymerisation, and a decrease in axonal stability [98]. This indicates that actin organisation supports microtubule architecture. Furthermore, both microtubules and membrane tension have been shown to contribute to axonal responses such as beading, retraction, and degeneration [99]. These findings suggest that the coordinated action of microtubules and membrane tension is essential for governing axonal mechanical behaviour. To further understand their interdependent roles, we also investigated how simultaneous perturbation of both cytoskeletal components influences axon retraction dynamics following ablation.

In the combination treatment, microtubules were first stabilised using Taxol, followed by actin depolymerisation with Latrunculin A. This resulted in reduced retraction after full ablation compared to

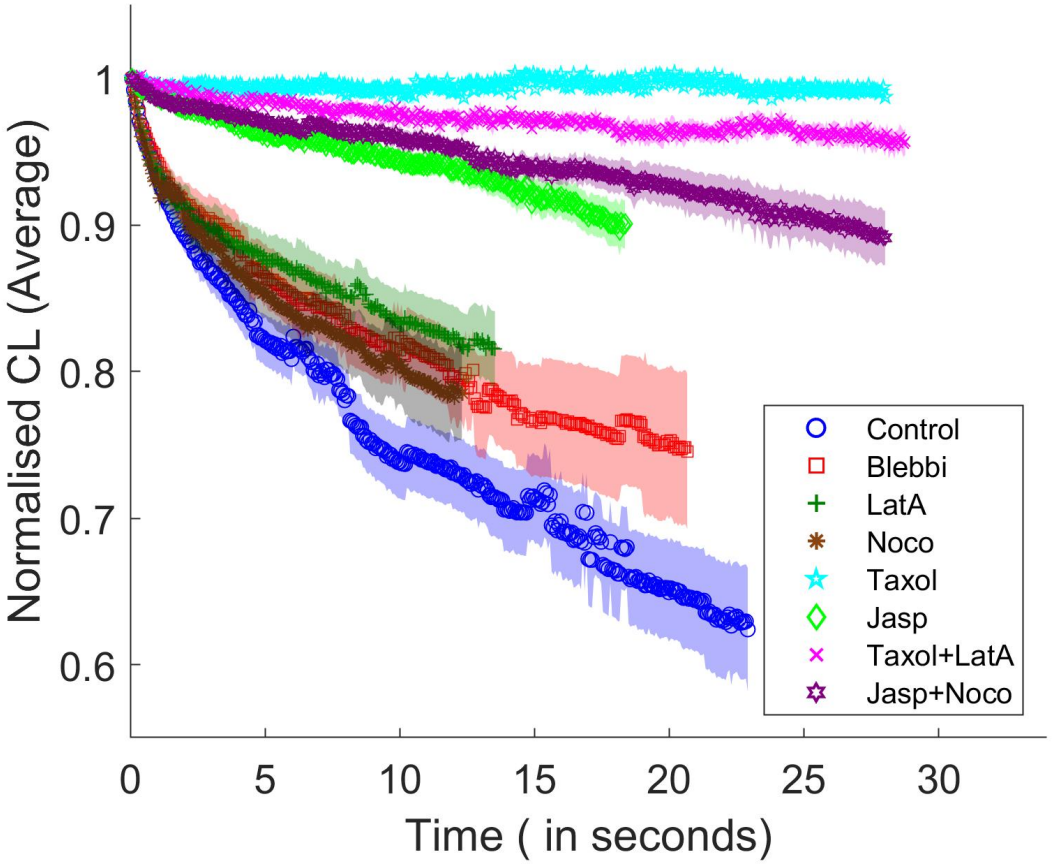

FIGURE 3.6: Normalised average contour length versus time plots for axons treated with Blebbistatin, Latrunculin A, Nocodazole, Taxol, Taxol + Latrunculin A, and Jasplakinolide + Nocodazole, along with the control (DMSO), following full ablation. The shaded regions represent the standard error of the mean (SEM).

controls. The corresponding contour length is shown in the figure 3.5c. In yet another combination treatment, actin was first stabilised using Jasplakinolide, followed by treatment with Nocodazole. This also resulted in slower retraction compared to the control. The figure 3.5d shows the associated contour length data.

In summary, we have observed that axons after full ablation had cytoskeletal elements severed, including the membrane. While all drug

treatments resulted in slower retraction speeds compared to the control, cytoskeleton stabilising drugs caused a significantly greater reduction in retraction speed than destabilising agents. A summary of the reduction in retraction speed observed across the various treatments is shown in figure 3.6.

3.5.2 Further analysis of ablation data

To further analyse the retraction responses quantitatively, we fitted the average data for all treatments. We first attempted to fit the average contour length data obtained from destabilising drug treatments, including the control, using a single exponential function. However, the initial part of the curves did not fit well. Therefore, we applied a double exponential function, which provided a more reasonable fit. Although this model improved the fit for most conditions, certain datasets still showed poor fitting in the later phase of the curve. To address this, we employed a composite model comprising a double exponential and a linear component of the form $y(t) = A_1 e^{-t/\tau_1} + A_2 e^{-t/\tau_2} + mt + C$, where τ_1 and τ_2 are the two relaxation time constants and m represents the slope. For stabilising and combination treatments, the initial fit using a single exponential function did not adequately capture the whole experimental data. Furthermore, the latter part of the curve appeared approximately linear. Therefore, we used a combined model of the form $y(t) = Ae^{-t/\tau} + mt + C$. which provided a good fit to the data. In the case of Taxol treatment, the linear fit resulted in zero velocity.

The negative sign of the slope indicates retraction. The parameters extracted from the fits for destabilising treatments are summarised in Table 3.1, while those for stabilising and combination treatments are listed in Table 3.2.

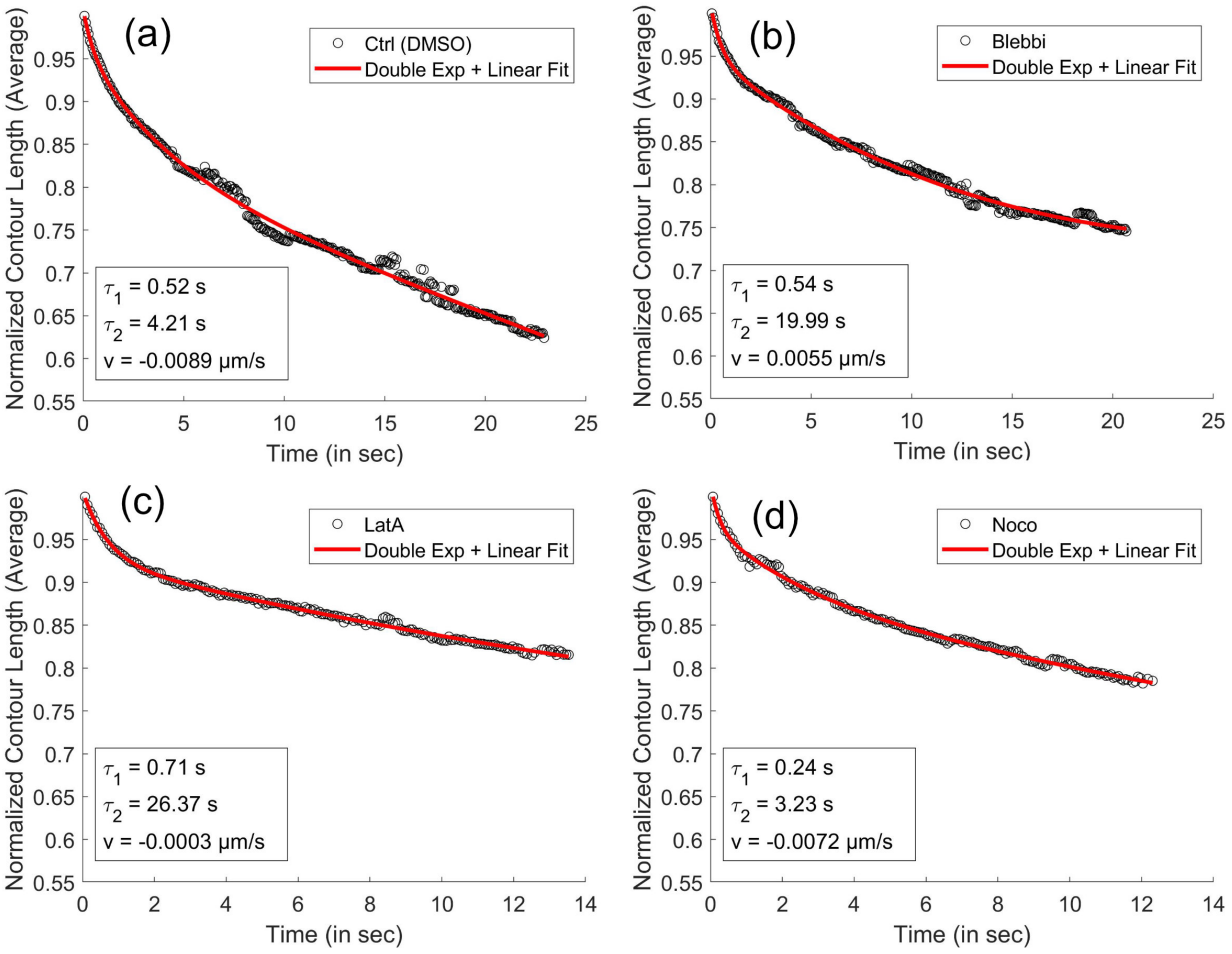

FIGURE 3.7: The combined double exponential and linear fit for normalised contour length (average) data is shown for (a) Control (DMSO), (b) Blebbistatin, (c) Latrunculin A, and (d) Nocodazole-treated axons. Black circle markers indicate the average data points, and the red curve represents the fitted plot. The two time constants and velocities are indicated in each plot for all treatments.

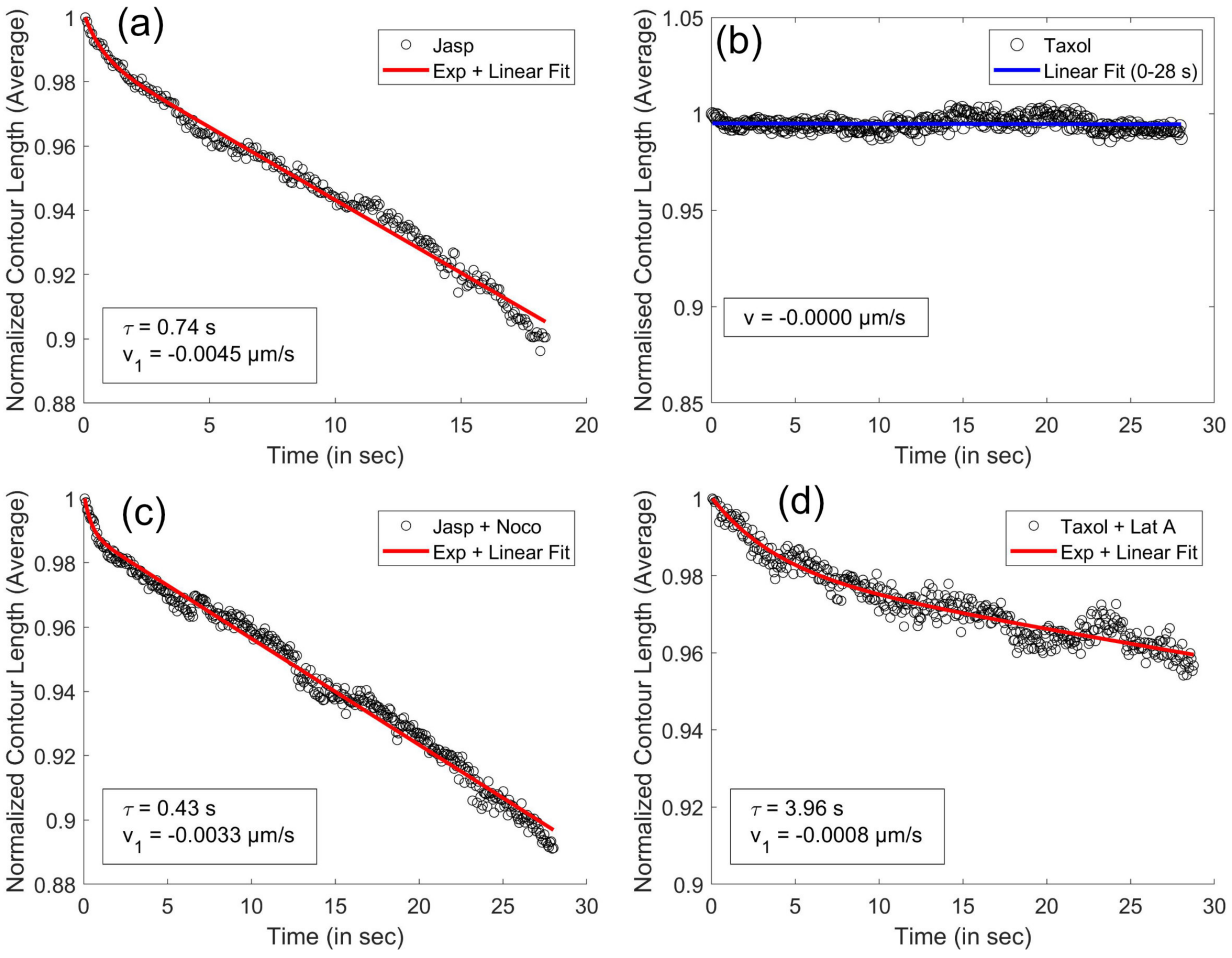

FIGURE 3.8: Fits to the normalised average contour length data are shown for (a) Jasplakinolide, (b) Taxol, (c) Taxol + Latrunculin A, and (d) Jasplakinolide + Nocodazole-treated axons. A combination of a single exponential and a linear function was applied for Jasplakinolide and combination treatments (red solid line), while a linear fit was used for the Taxol case (blue solid line). Black circles indicate the average data points.

Drug treatment	**Relaxation Times (in sec)**		**v (in μm/m)**
	τ_1	τ_2	
Control (DMSO)	0.52	4.21	-0.0089
Blebbistatin	0.57	14.30	-0.0003
Latrunculin A	0.71	26.37	-0.0003
Nocodazole	0.24	3.23	-0.0072

TABLE 3.1: Relaxation times and velocities following full ablation under various treatments (Blebbistatin, Latrunculin A, Nocodazole), including the Control condition.

Drug treatment	**τ (in sec)**	**v (in μm/m)**
Jasplakinolide	0.74	-0.0045
Jasplakinolide+Nocodazole	0.43	-0.0033
Taxol+Latrunculin A	3.96	-0.0008
Taxol	Non-exponential	0

TABLE 3.2: Relaxation times and velocities were extracted from the retraction curves (Contour length vs time) for various treatments (Jasplakinolide, Jasplakinolide+Nocodazole, Taxol+Latrunculin) following full ablation. For Taxol, which remained nearly constant throughout, the velocity was considered to be zero for the entire curve.

3.5.3 Axonal buckling following ablation

The buckling data for control, Blebbi, Lat A and Noco are shown in figure 3.9a, b, c, d, respectively. The buckling data for cytoskeleton stabilising drugs (Taxol and Jasp), as well as combination treatments (Taxol + LatA and Jasp + Noco), are shown in figure 3.10a, b, c, d, respectively.

A comparison of the averaged buckling data for the initial 30 s, for all treatments, is presented in Figure 3.11. The buckling plots over time for most treatments largely overlap, except for those involving

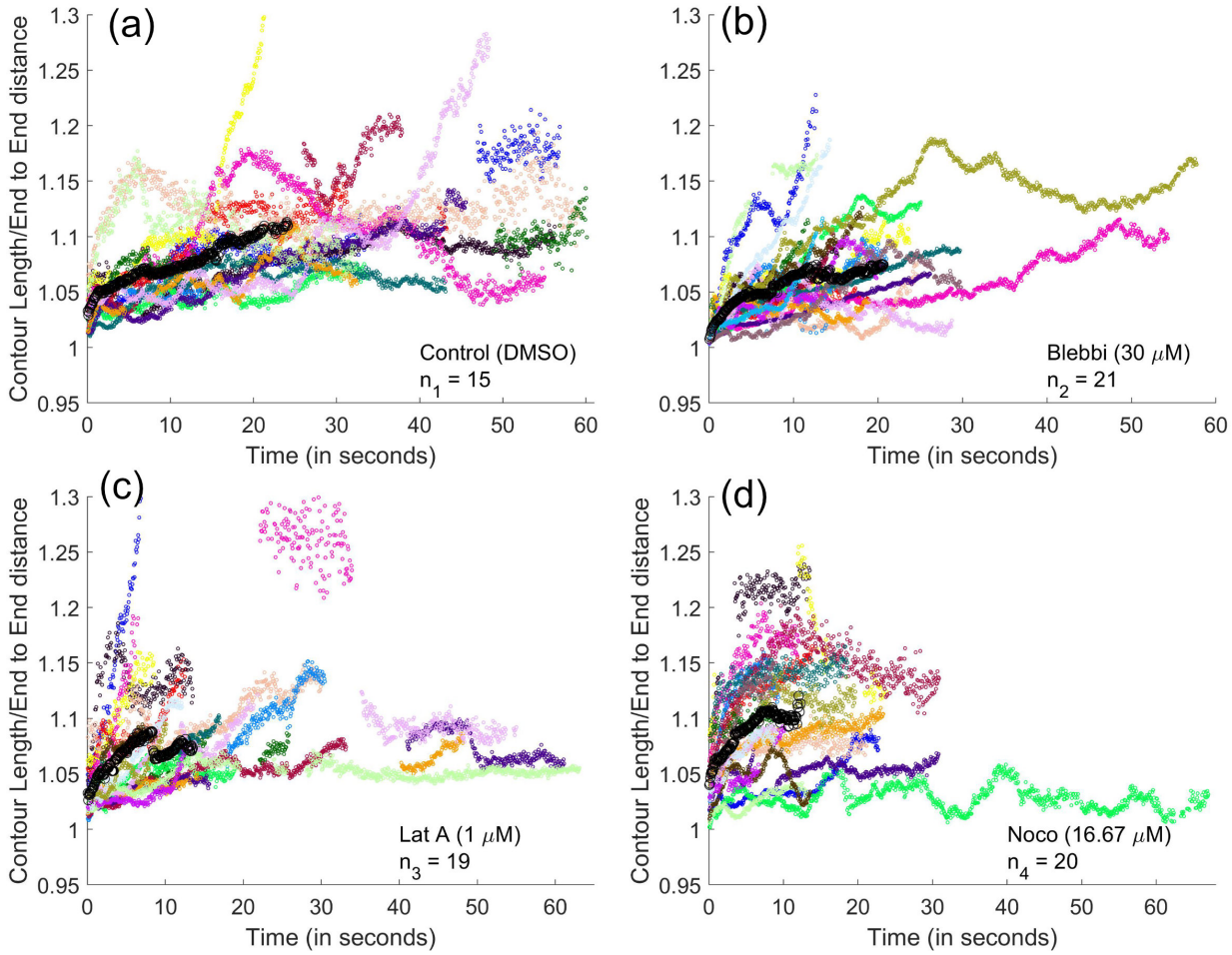

FIGURE 3.9: The buckling (contour length/end to end distance) and time plot is shown in (a) for Control (DMSO), (b) Blebbistatin (c) Latrunculin A and (d) Nocodazole treated axons. The bold black circles represent the average buckling response for each treatment, while the colored curves with smaller circular markers correspond to the buckling behaviour of individual axonal segments.

Taxol and the combination of Taxol and Latrunculin A, which show a noticeable difference. Specifically, axons treated with Taxol or Taxol+LatA exhibit significantly reduced buckling compared to the control and other treatments.

Although the buckling data are relatively noisy, both the images and contour length analysis clearly indicate that Taxol suppresses buckling. This suppression may result from an increase in microtubule number and/or length, leading to a greater number of microtubules

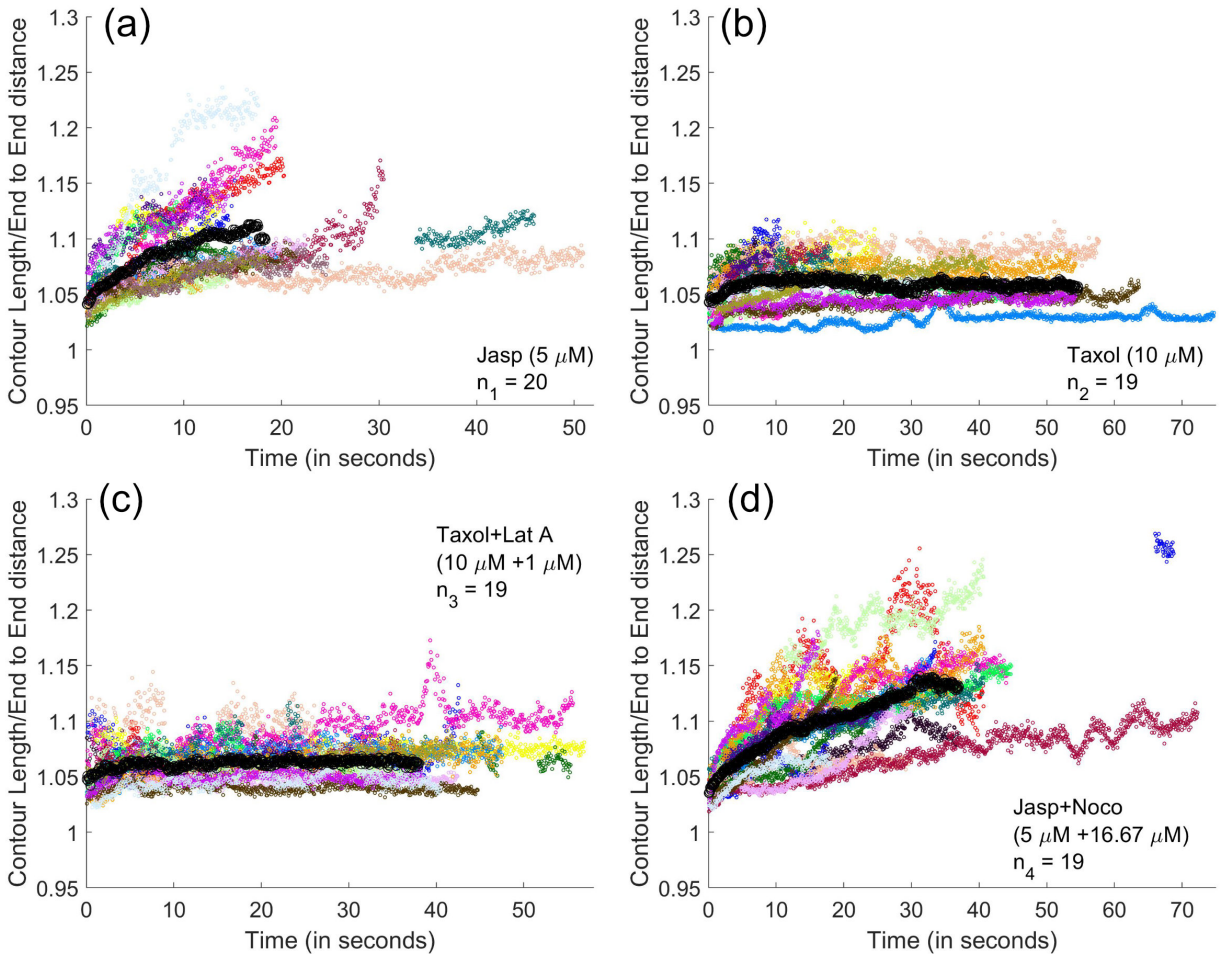

FIGURE 3.10: The buckling versus time plots for (a) Jasplakinolide, (b) Taxol, (c) Taxol + Latrunculin A, and (d) Jasplakinolide + Nocodazole-treated axons are shown. The bold black circles represent the average buckling curves for each treatment, while the colored curves with smaller markers represent the buckling behaviour of individual axonal segments.

per axonal cross-section and, consequently, a greater bending modulus of the microtubule bundle. Supporting images of control and Taxol-treated axons further illustrate this trend, as shown in the figure 3.2 and 3.3. Furthermore, the combined treatment with Taxol and Latrunculin A, which stabilises microtubules while eliminating actomyosin-driven contractile forces, also results in minimal buckling, too supports that microtubule mechanics play a dominant role

in axonal buckling. For direct comparison, the buckling plots of control, Taxol, and Taxol+LatA treatments, with error bars, are shown in Figure 3.12. To summarise, these observations suggest that microtubule stabilisation by Taxol enhances axonal stiffness and reduces susceptibility to buckling.

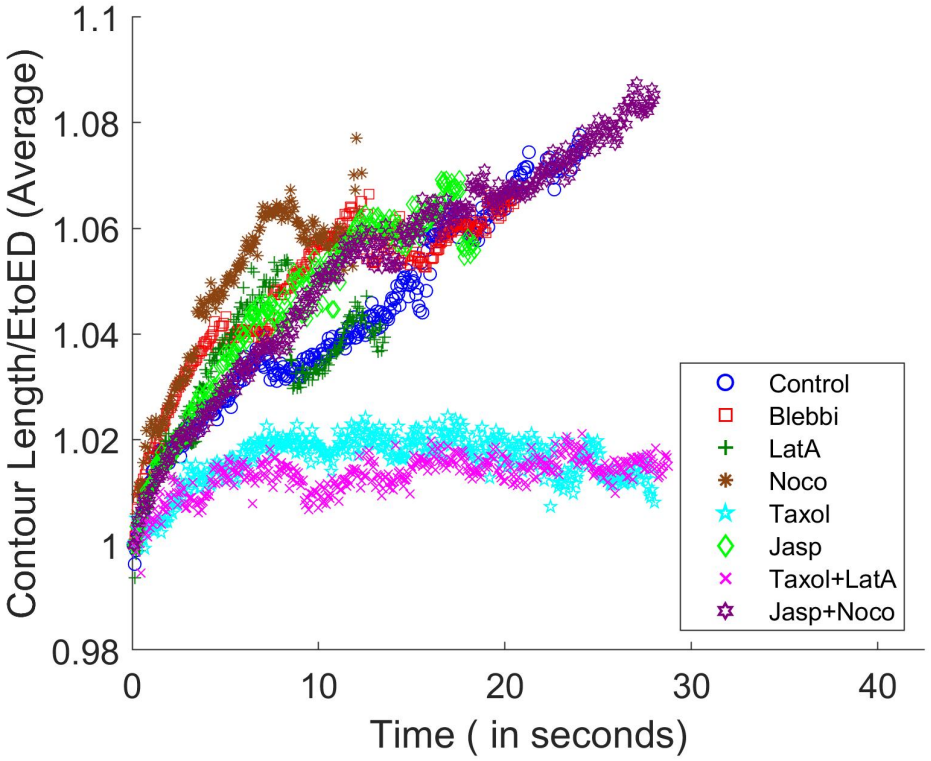

FIGURE 3.11: Average buckling versus time plots for all pharmacologically treated axons, including Blebbistatin, Latrunculin A, Nocodazole, Taxol, Taxol + Latrunculin A, and Jasplakinolide + Nocodazole, along with the control (DMSO), following full ablation.

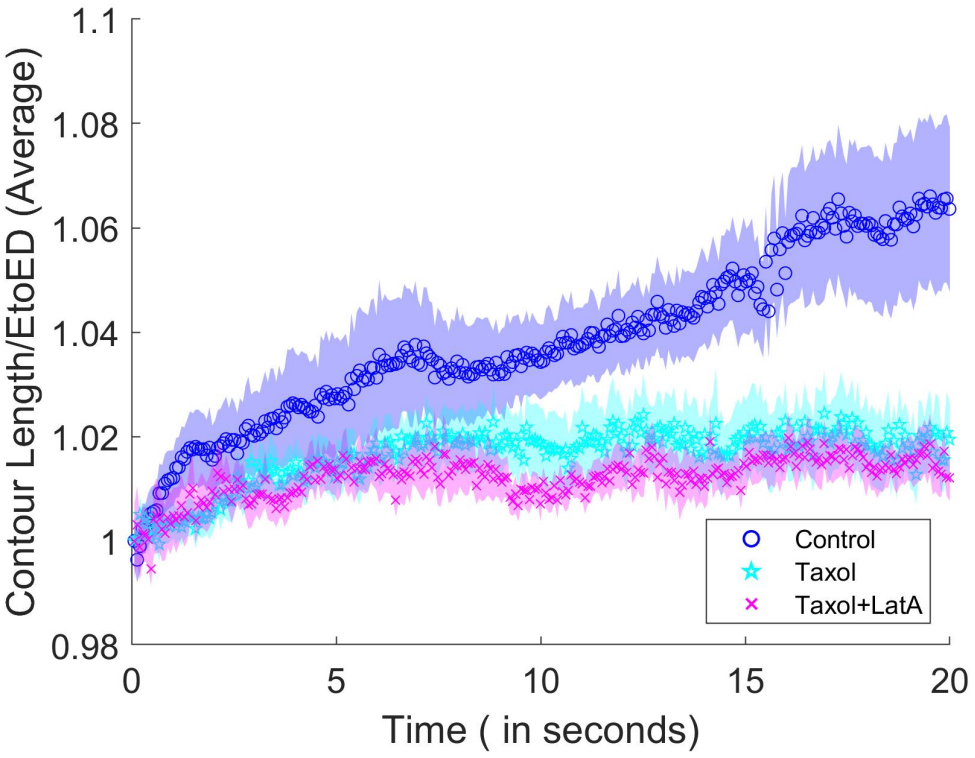

FIGURE 3.12: Buckling comparison of control, Taxol, and Taxol + Latrunculin A treated axons after full ablation, shown with error bars.

3.5.4 Retraction Responses of axons after partial ablation

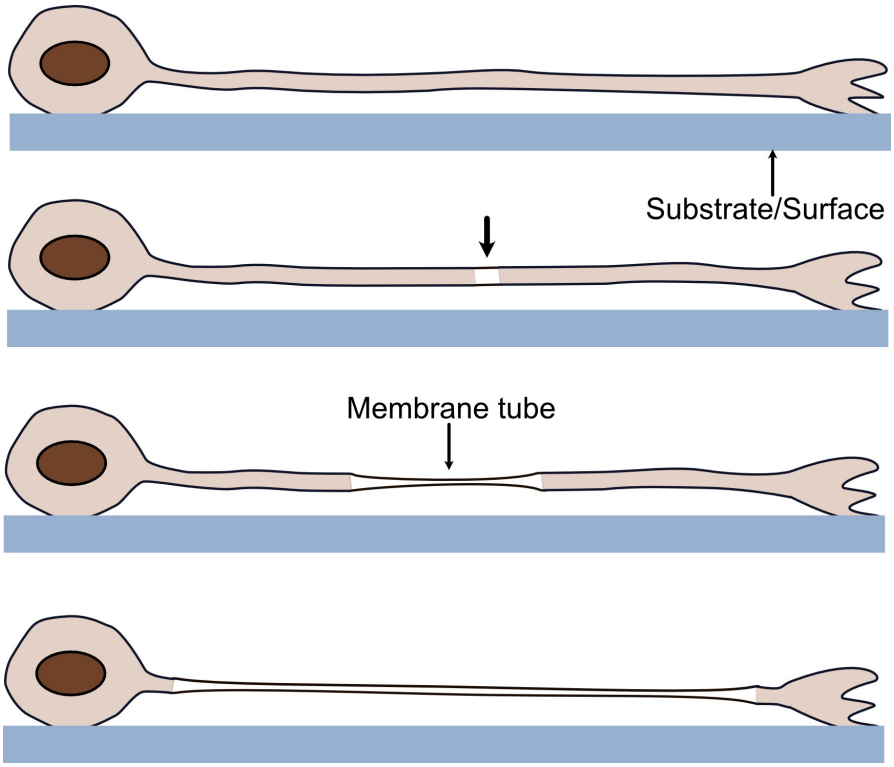

FIGURE 3.13: Both ends of the neuron are attached at both ends, but the axonal region is free from the substrate. The thick black arrow points to where the ablation occurred. After ablation, the axon thins down as the thinned portion expands toward both sides, while the membrane tube remains preserved.

In experiments involving complete ablation of floating axons, the proximal and distal parts are fixed only at their extremities. However, at the point of ablation, both segments move freely in the extracellular medium due to the complete cut. We observed that the axonal segments tend to shift out of focus after ablation. This shift complicates the accurate measurement of contour lengths. The error in calculating contour length may affect our understanding of how cytoskeletal elements contribute to long-term retraction.

To overcome this issue, we developed a technique to perform partial ablation of axons, which involves severing only the intracellular

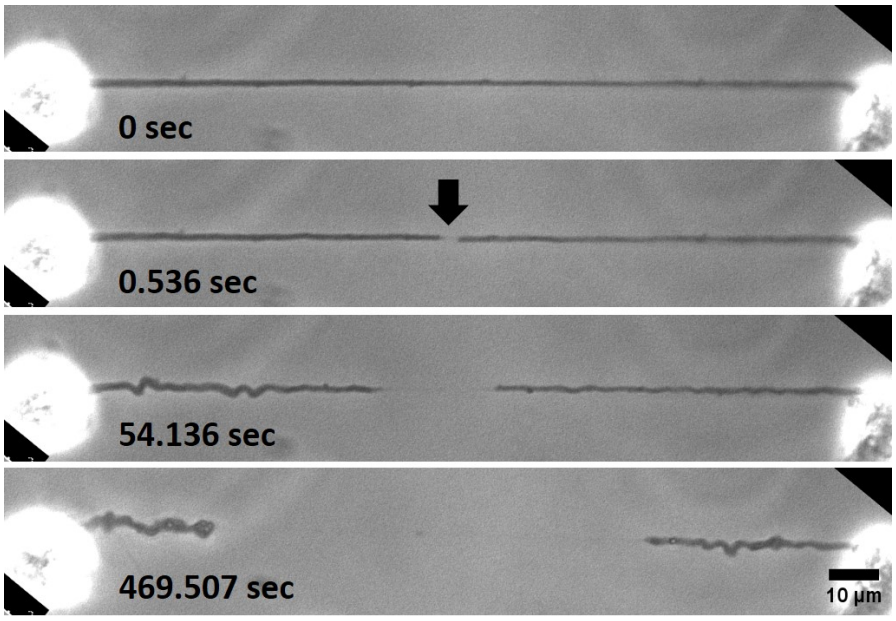

FIGURE 3.14: This image sequence shows partial ablation in control axons. The thick black arrow marks the ablation site. Following ablation, the internal cytoskeletal material retracts toward both ends, while the membrane remains intact. Scale bar: 10 μm.

components while keeping the membrane tube intact. The tension in the contiguous membrane bridge keeps the axon straight and mostly in focus, even as the axonal cytoskeleton recedes in both directions (shown in the figure 3.13 and 3.14).

We also observed a variability in axonal diameters across samples. This variation is important because the diameter of an axon can influence its mechanical behaviour. For example, a thicker axon may resist deformation differently than a thinner one due to differences in cross-sectional area, internal tension, and cytoskeletal composition. Microtubule density decreases with increasing axonal diameter, but there is a rise in the total number of microtubules in DRG neuron axons [100]. Therefore, this heterogeneity in axonal diameter could affect the retraction response. To account for this, we measured

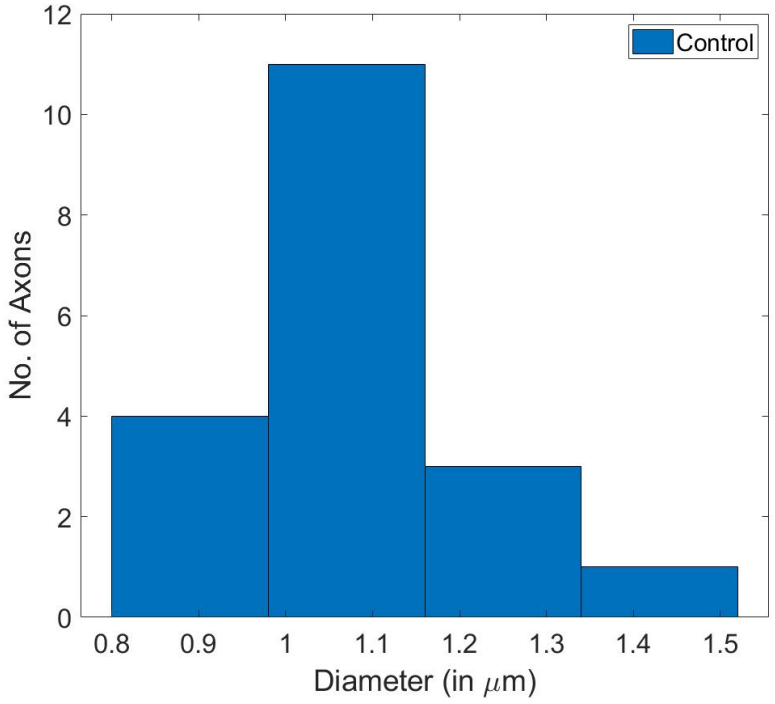

FIGURE 3.15: The diameter distribution of axons subjected to partial ablation in control-treated conditions is shown here.

the diameter of axons used in the control experiments shown in the figure 3.15.

All the drug treatments here were performed in the same way as done for the full ablation experiments and described in the section 3.4. The partial ablation data were initially recorded at 6 frames per second (fps) until around 60 seconds, after which the recording speed was switched to 15 fps. The gap in the data corresponds to the transition between the two recording speeds.

The contour length analysis for control axons (treated with DMSO) after partial ablation is shown in figure 3.16. Blebbistatin-treated axons exhibit slower retraction compared to control, as illustrated in figure 3.17. Similarly, Latrunculin A treatment results in reduced

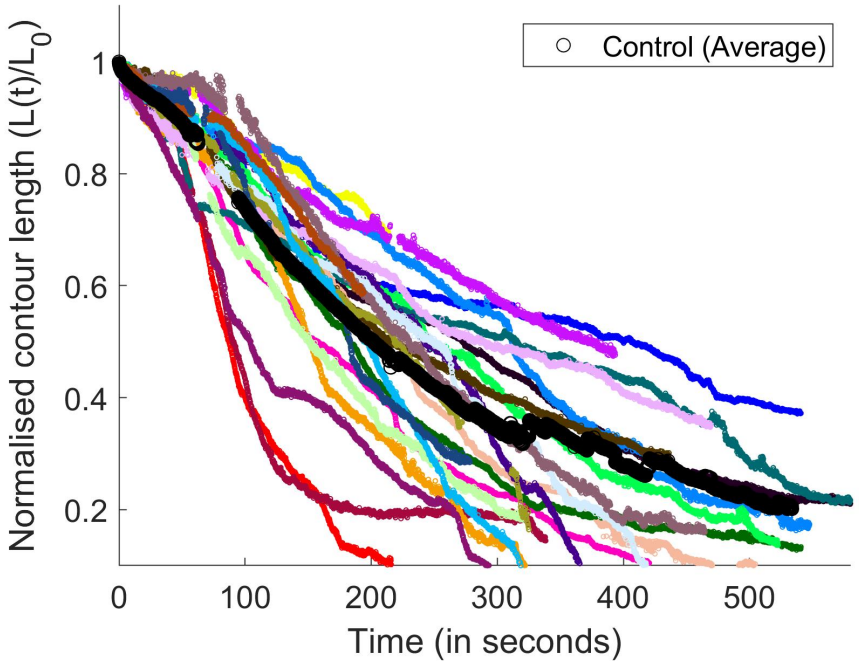

FIGURE 3.16: The normalised contour length vs time plot for control (DMSO) axons after partial ablation is shown here. The bold black circle represents the average plot over n = 24 axonal segments. The other colored curves with smaller marker sizes represent the individual axonal segment contour length plots. Normalisation was done by dividing the contour length at each time point, L(t), by the initial contour length just after ablation (L_0). Discontinuities in the average plot arise because some axonal segments retract early. The gap in the data at around t = 54 s is due to the switching of the recording speed from 15 fps to 6 fps.

retraction, with corresponding data shown in figure 3.18. In contrast, Nocodazole-treated axons retract more rapidly than control (figure 3.19), while Jasplakinolide treatment also increases retraction, though to a lesser extent (figure 3.20). Taxol treatment leads to slower retraction relative to control (figure 3.21). Notably, the combination of Taxol and Latrunculin A results in minimal retraction, indicating a strong inhibitory effect on cytoskeleton-driven shortening as shown in figure 3.22. The average normalised contour length over time for all partial ablation experiments with different drug treatments is summarised in the figure (3.23).

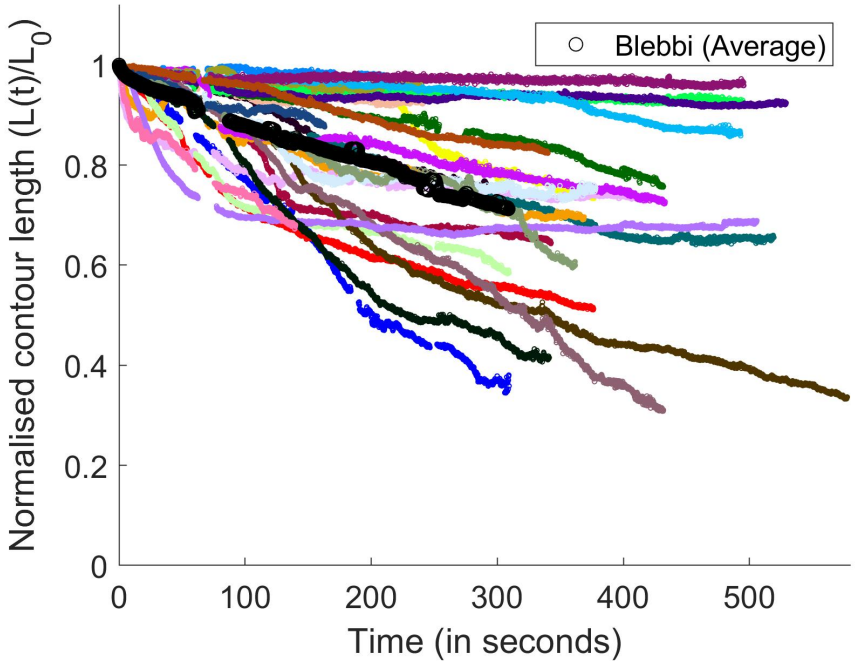

FIGURE 3.17: The normalised contour length vs time plot for blebbi-treated axons is demonstrated here. The bold black circle represents the average plot over n = 28 axonal segments. The other colored curves with smaller marker sizes represent the individual axonal segment contour length plots.

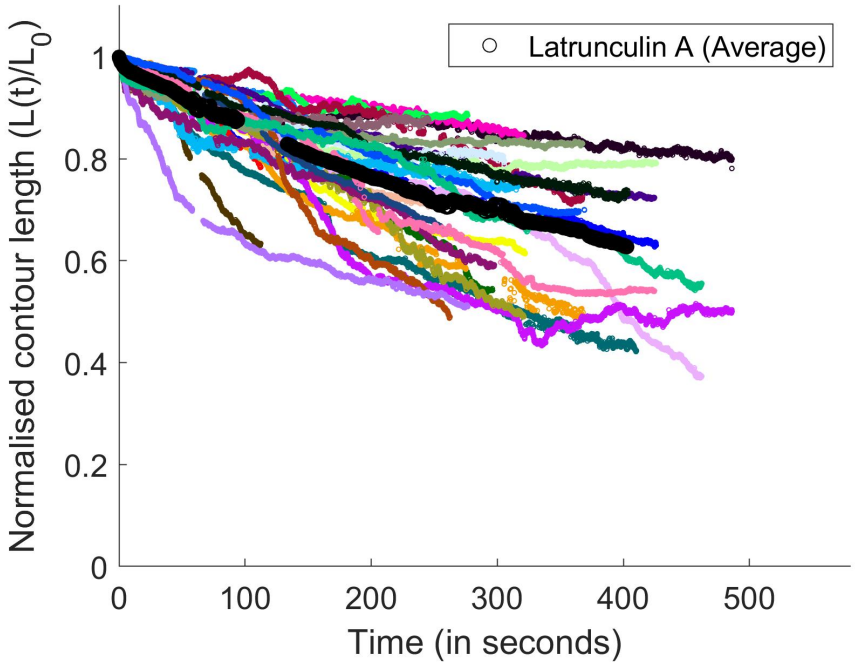

FIGURE 3.18: The normalised contour length vs time plot for Lat A-treated axons is shown here. The bold black circle represents the average plot over n = 30 axonal segments. The other colored curves with smaller marker sizes represent the individual axonal segment contour length plots.

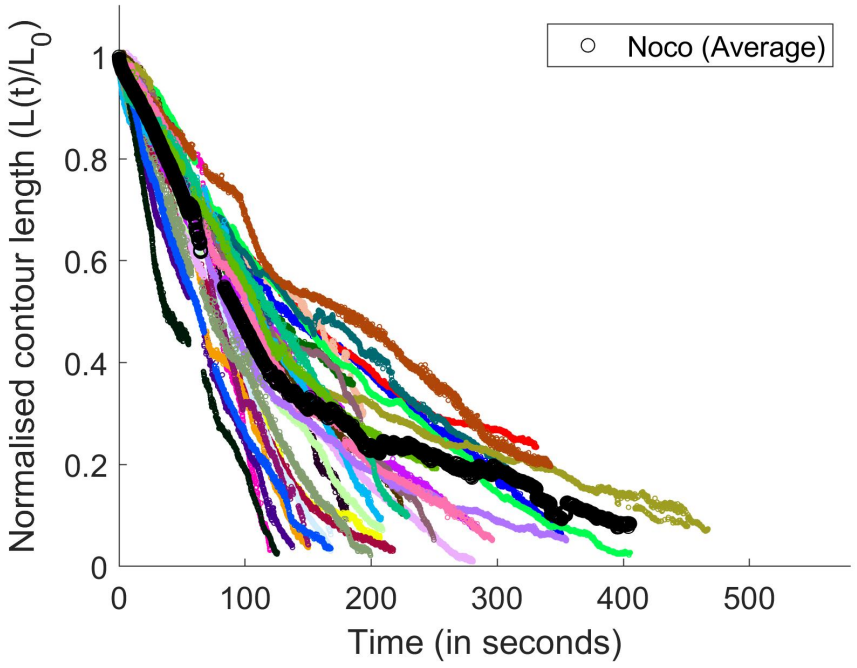

FIGURE 3.19: The normalised contour length vs time plot for Noco-treated axons is shown here. The bold black circle represents the average plot over n = 31 axonal segments. The other colored curves with smaller marker sizes represent the individual axonal segment contour length plots.

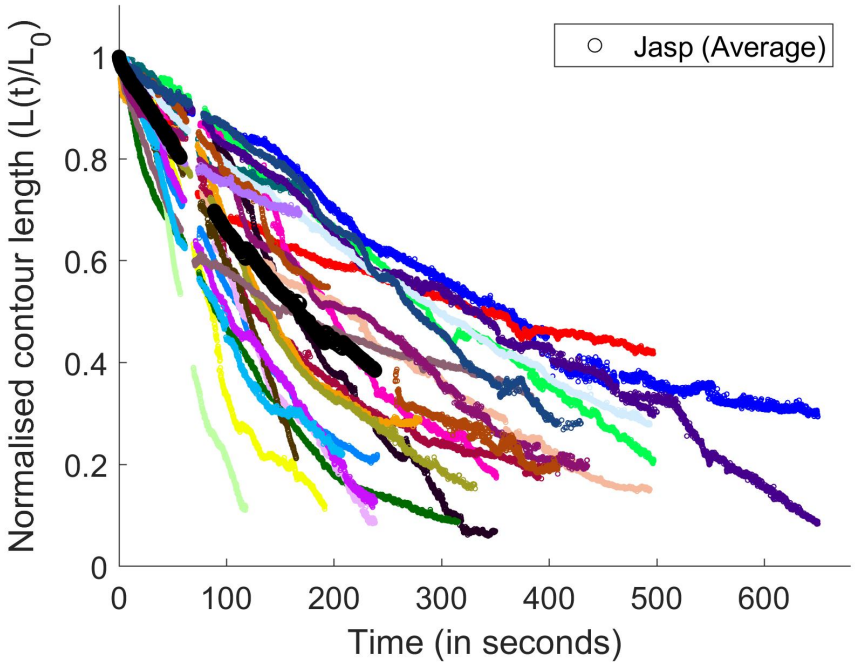

FIGURE 3.20: The normalised contour length vs time plot for Jasp-treated axons is shown here. The bold black circle represents the average plot over n = 25 axonal segments. The other colored curves with smaller marker sizes represent the individual axonal segment contour length plots.

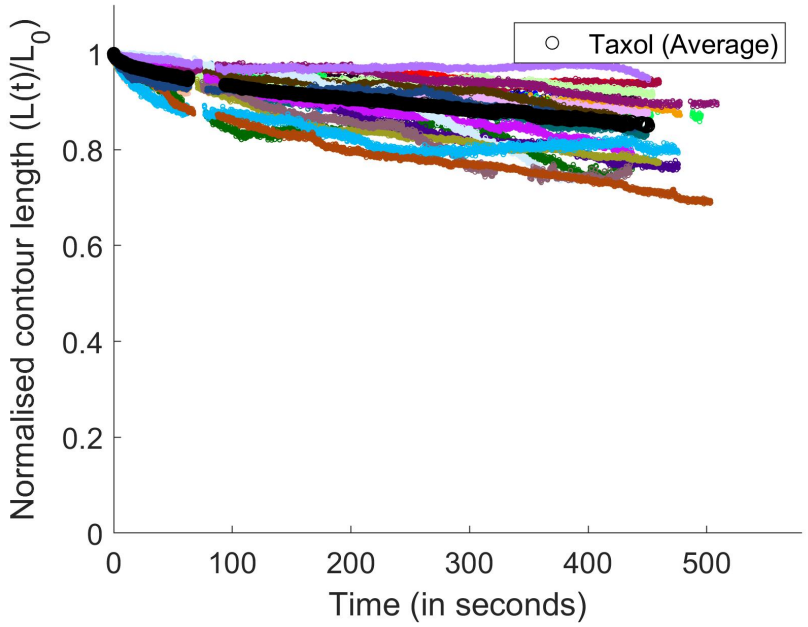

FIGURE 3.21: The normalised contour length vs time plot for Taxol-treated axons is demonstrated here. The bold black circle represents the average plot over n = 25 axonal segments. The other colored curves with smaller marker sizes represent the individual axonal segment contour length plots.

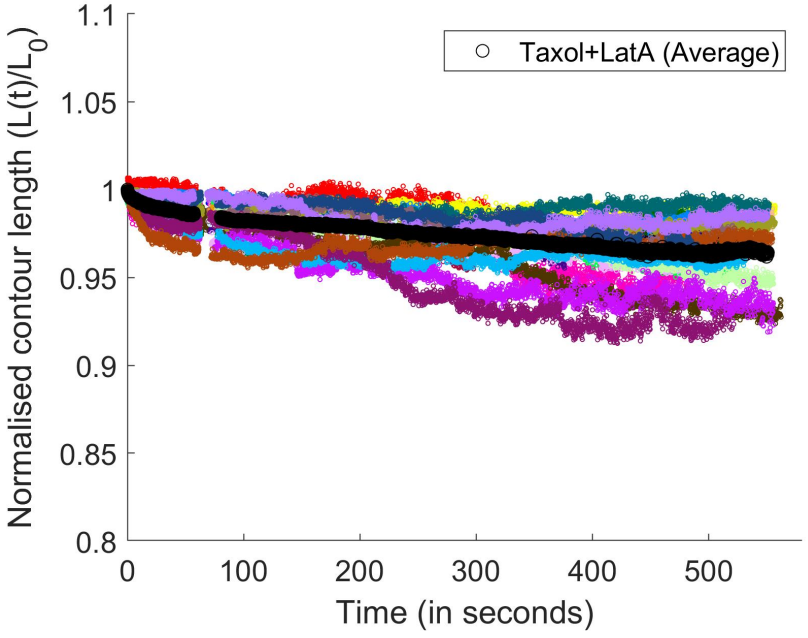

FIGURE 3.22: The normalised contour length over time for axons treated with a combination of Taxol and Latrunculin A, after partial ablation, is shown here. In this experiment, the axons were first treated with Taxol for 30 minutes, followed by treatment with Lat A for an additional 15 minutes. The bold black circle represents the average plot over n = 34 axonal segments. The other colored curves with smaller marker sizes represent the individual axonal segment contour length plots.

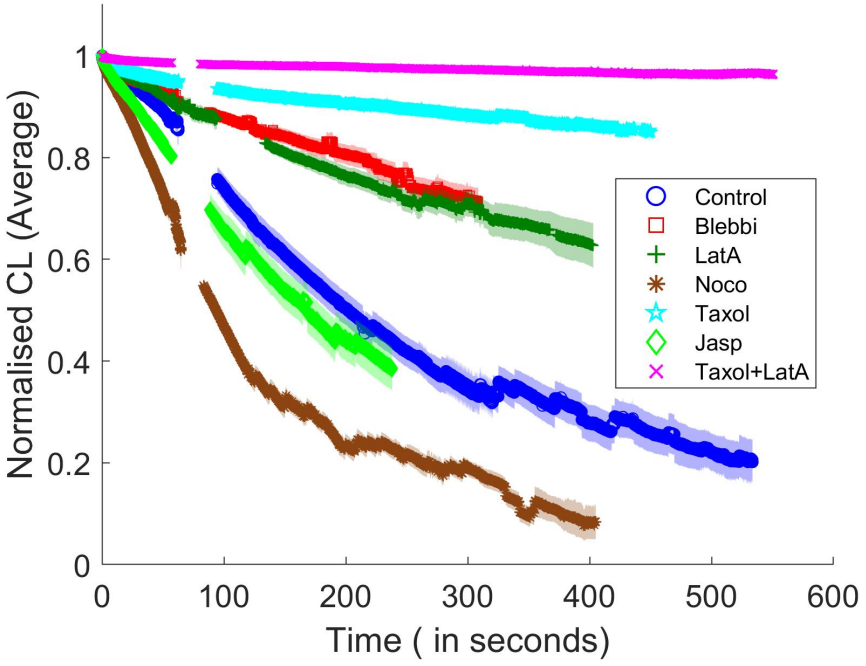

FIGURE 3.23: Normalised contour length (Average) with time plots of all pharmacologically treated axons including control (DMSO), Blebbistatin, Latrunculin A, Nocodazole, Taxol, Jasplakinolide and Taxol+Latrunculin-A after partial ablation.

3.5.5 Axonal retraction induced by growth-cone detachment using trypsin

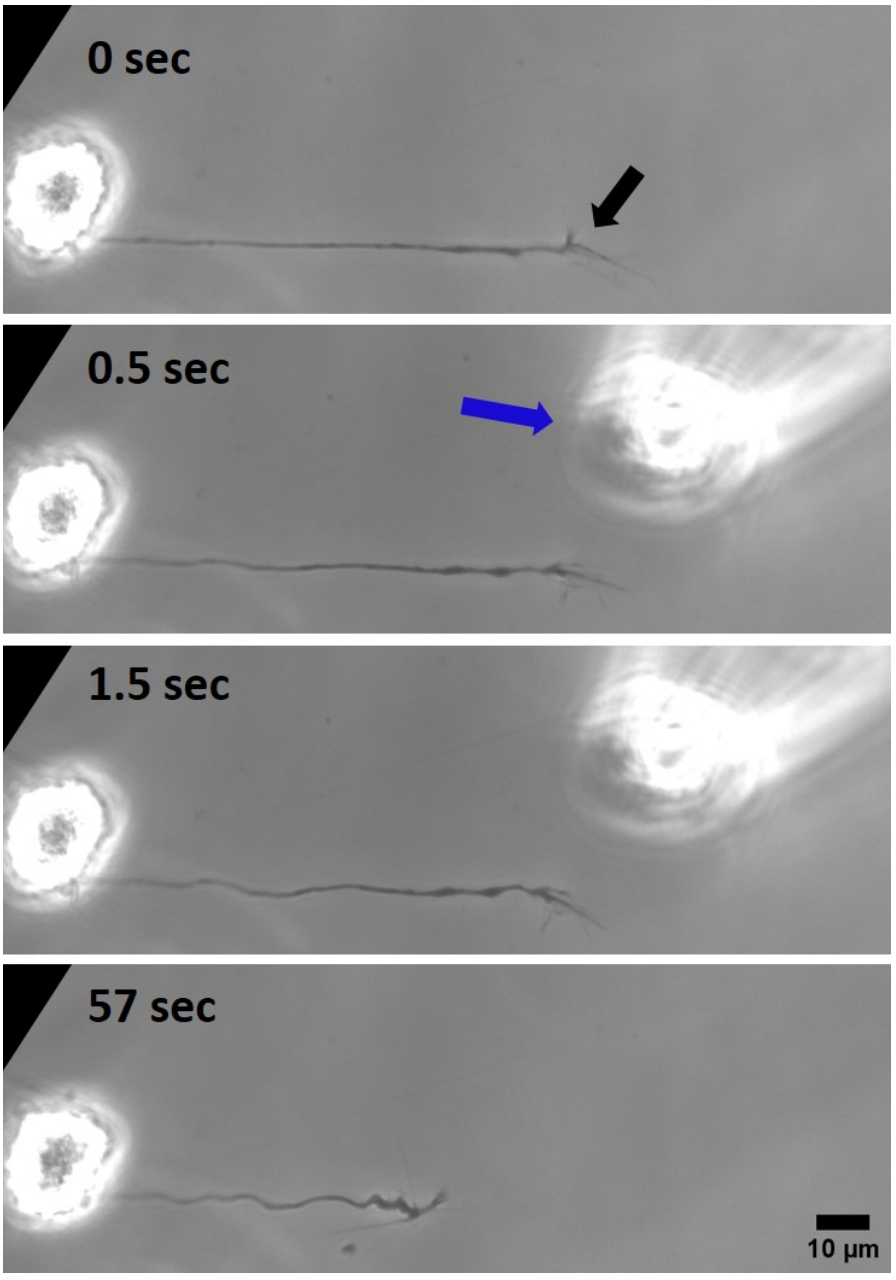

FIGURE 3.24: Image sequence showing axonal retraction following trypsin-induced growth cone detachment. The black arrow points to the growth cone, while the blue arrow indicates the glass capillary containing trypsin.

When ablation with a laser is performed, it severs microtubules and may induce microtubule depolymerisation. This laser induced microtubule damage may significantly affect the observed retraction

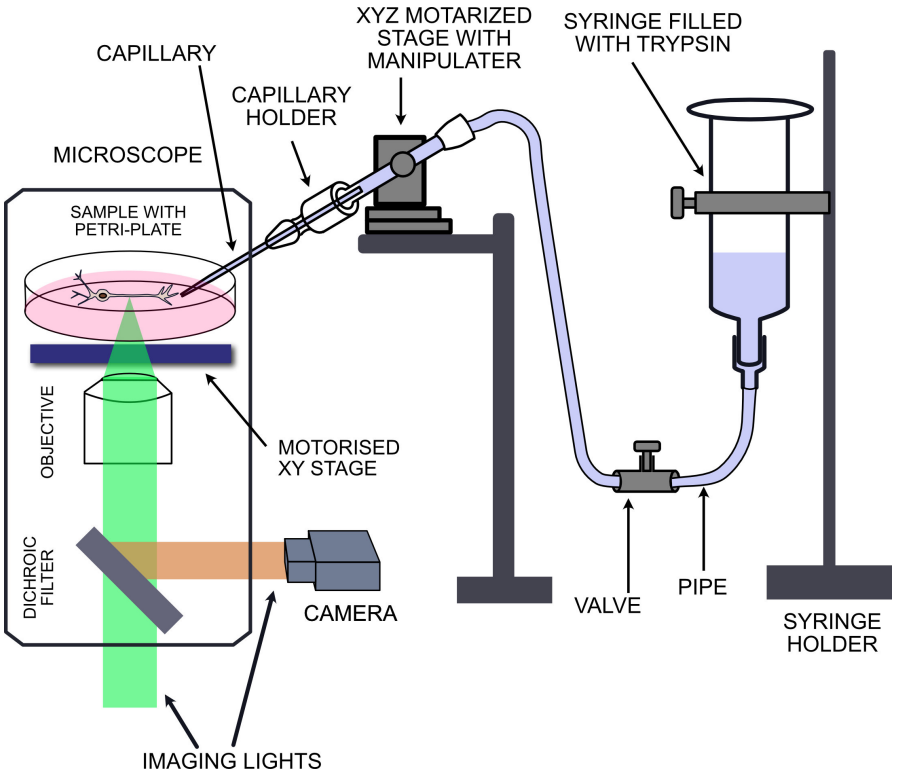

FIGURE 3.25: **Gravity-driven flow system for localised trypsin application** This setup consists of a syringe filled with trypsin and connected to a plastic tube, positioned at a higher level relative to the sample stage to enable gravity-driven flow. A valve is integrated along the plastic tube to control the fluid flow. An XYZ motorised stage, mounted on a secondary platform holding a capillary holder that connects a plastic tube on one end and a glass capillary on the other. The forged tip of the capillary is positioned near the neuronal growth cone. The sample immersed in a nutrient medium is placed on the microscope stage. Imaging lights illuminate the sample, and a camera captures the images.

responses. Additionally, laser ablation may trigger calcium influx and activate injury-induced signalling pathways (discussed in detail in Chapter 4). To investigate retraction responses without inducing direct cytoskeletal damage, we employed a biochemical method to induce axonal detachment. Specifically, we used trypsin, a proteolytic enzyme that breaks down proteins, to locally detach the axon from the substrate at the growth cone. In addition to injury-induced retraction, axons also undergo retraction during development as part of the natural pruning process to eliminate unnecessary branches.

To examine whether the mode of induction influences the retraction response, this non-injury approach can be used. This method may mimic retraction events that occur during development.

In this experiment, we utilised trypsin-induced retraction, wherein trypsin was applied near the axonal growth cone to locally degrade the linkages to the extracellular matrix (ECM) and disrupt adhesion between the axon and the substrate (shown in figure 3.24). Unlike laser ablation, which physically severs the axon and can lead to rapid cytoskeletal disruption and local depolymerisation at the injury site, trypsin treatment does not cut the axon. Also, it weakens axon-substrate interactions and induces retraction without damaging the axonal membrane or internal cytoskeletal structure. This approach maintains the mechanical continuity of the axon, thereby allowing the study of retraction driven purely by the intrinsic cytoskeletal tension.

To enable localised application of trypsin to axonal growth cones, we developed a home-built gravity-driven flow system for controlled detachment and retraction analysis, as shown in figure (3.25). In this setup, borosilicate glass capillaries (catalogue number B100-75-10, Sutter Instrument, United States) were pulled into fine-tipped needles using a micropipette puller (Model P-2000, Sutter Instrument, United States) equipped with a CO_2 laser-based heating source. The inner diameters of the capillary tips were refined to 20–30 μm using a microforge (Model MF-900, Narishige, Japan). These forged capillaries were then mounted on a mechanical micromanipulator

(Model BRM/E, Xenoworks, Sutter Instrument, United States) via a needle holder. One end of the needle holder was connected to a plastic syringe filled with trypsin through tubing and a flow-control valve, while the other end held the capillary needle. The tip of the needle was immersed in the culture medium and positioned near the growth cone on the glass substrate using the micromanipulator's stage controller. Trypsin was then released using the valve to induce detachment of the growth cone. The resulting retraction dynamics were recorded using a camera (DFC365 FX, Leica) at a frame rate of 2 fps.

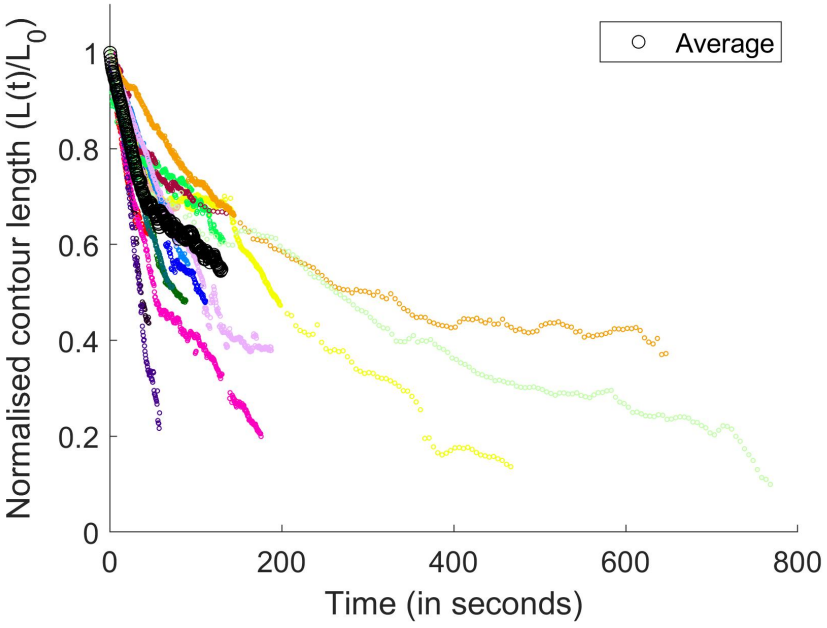

FIGURE 3.26: The plot of normalised contour length over time for axons detached from growth cones by trypsin treatment is shown here. The bold black circle indicates the average plot based on n = 15 axons. The additional colored curves with smaller markers represent the contour length plots of individual axonal segments.

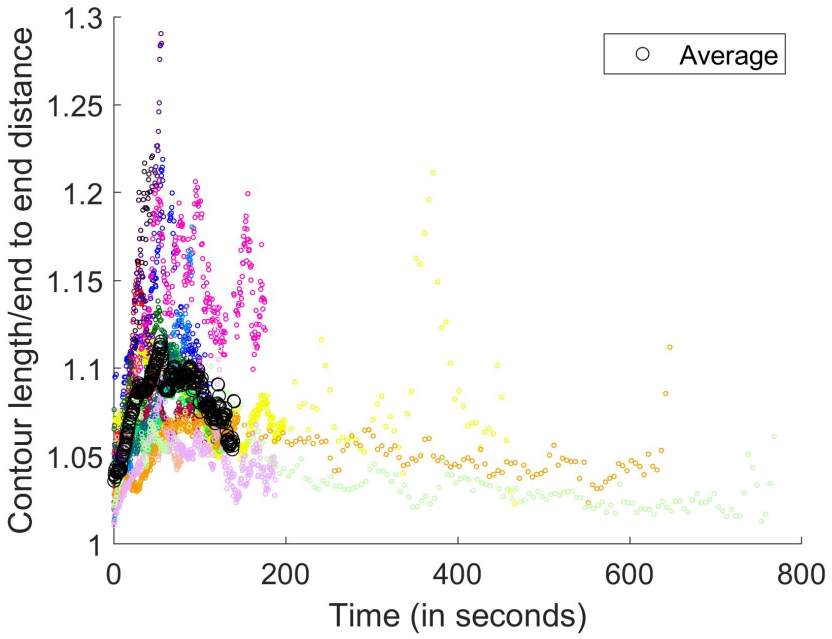

FIGURE 3.27: The plot for the buckling vs time of trypsin-induced detached axons from growth cones is shown here. The bold black circle indicates the average plot over n = 15 axons. The additional colored curves with smaller markers represent the contour length plots of individual axonal segments.

The flow of trypsin in this setup is driven by hydrostatic pressure, which is generated by positioning the trypsin-filled syringe at a height above the sample stage. Since the syringe lacks a plunger, gravity acts directly on the fluid column, which creates pressure at the base of the syringe according to the equation P= ρgh. In this equation, P represents the hydrostatic pressure at the outlet, ρ is the density of the trypsin solution (approximately 1000 kg/m^3, similar to water), g is the gravitational acceleration (9.81 m/s^2), and h is the vertical height difference between the fluid level in the syringe and the fluid level in the petri plate. Since the capillary tip is immersed in the petri dish fluid, that fluid exerts its own pressure. What matters is the difference in pressure, that is, how much more pressure the syringe height generates relative to the dish fluid. This pressure

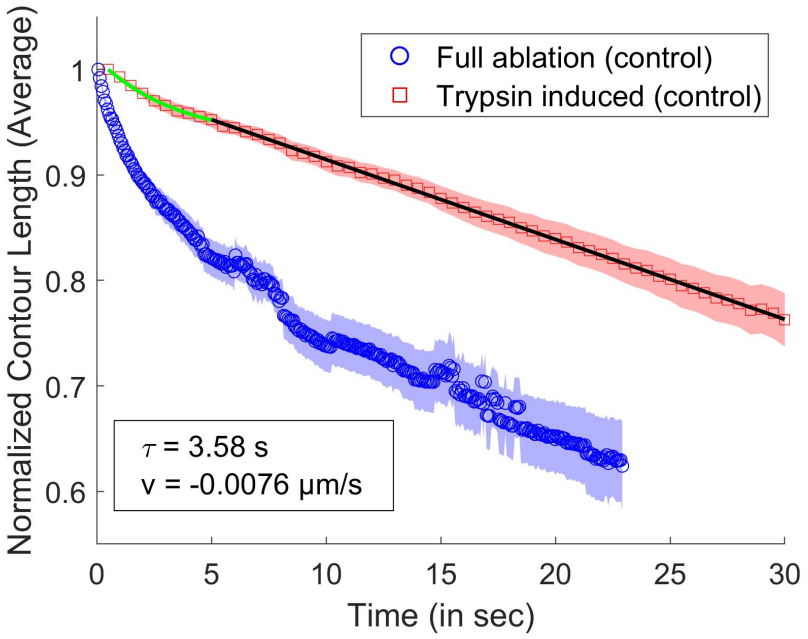

FIGURE 3.28: The comparison of normalised contour length versus time plots for full ablation and trypsin-induced axons. This comparison is for control (DMSO-treated) axons. The blue circle and red square denote the full ablation and trypsin-induced data, respectively. The averages are taken over n1 = 18 axonal segments for full ablation and n2 = 15 for trypsin-induced axons. Contour length data from trypsin-induced axons is fitted with a green exponential curve up to 5 seconds to get the relaxation time, followed by a black linear fit to estimate retraction velocity.

drives the trypsin solution through the connected plastic tube and ultimately toward the capillary.

The contour length and buckling responses during retraction, following growth cone detachment induced by trypsin, are shown in the figures 3.26 and 3.27, respectively. The contour length data is fitted with a single exponential curve for the initial 5 seconds, yielding a relaxation time of 3.58 seconds. Beyond 5 seconds, a linear fit is applied to determine the retraction velocity, which is 0.0076 μm/s (shown in the figure 3.28).

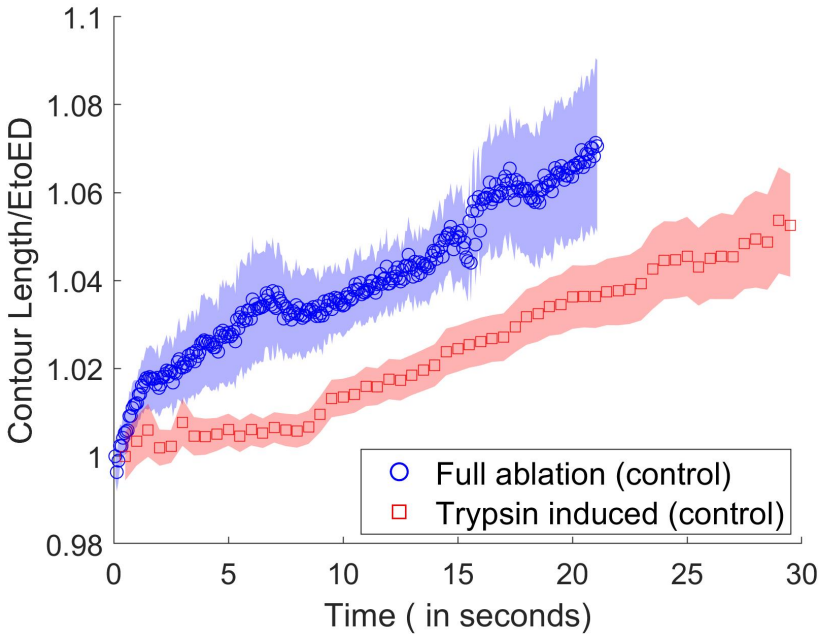

FIGURE 3.29: The comparison of buckling versus time plots for full ablation and trypsin-induced axons. This comparison focuses on control axons treated with DMSO. The data for full ablation is indicated by a blue circle, while the trypsin-induced data is represented by a red square. Averages have been calculated from n1 = 18 axonal segments for the full ablation group and n2 = 15 axons for the trypsin-induced group.

3.5.5.1 Possible explanation for full ablation and trypsin-induced retraction of control axons

The contour length and buckling responses after laser ablation and local treatment of trypsin for control axons are shown in the figures 3.28 and 3.29. The contour length evolution is much faster in laser ablation compared to retraction induced by local application of trypsin. Additionally, axonal buckling is lower in trypsin-detached axons than in fully ablated ones. Although full ablation-induced retraction exhibits two time scales, the initial dominant time scale is $\tau_1 = 0.52$ sec (from Table 3.1), whereas trypsin-induced retraction shows a relaxation time scale of $\tau = 3.58$ sec. This indicates a

significant quantitative difference between the two types of induced retraction.

In full ablation, cutting the axon triggers a rapid calcium influx (explained in detail in chapter 4), which can activate actomyosin contractility and calpain proteases [101]. These processes may weaken the cytoskeleton and accelerate retraction. In contrast, trypsin-induced detachment likely causes little or no calcium influx, so active contraction and cytoskeletal disassembly are limited, resulting in slower retraction.

3.6 Possible explanation for retraction after ablation

Although the overall trends in response are similar between full and partial ablation for most drugs, Jasplakinolide and Nocodazole exhibit pronounced differences (see figure 3.6 and 3.23).

Myosin II motor activity is essential for retraction. Inhibiting myosin with blebbistatin dramatically suppresses retraction of severed axons. Gallo et al showed in retinal and chick DRG axons that Blebbistatin treatment minimised axon retraction after severing. When myosin II is blocked, the axon barely retracts following injury. They have also reported that inhibiting upstream regulators of myosin, such as Rho-associated protein kinase (ROCK)or Myosin light-chain kinase (MLCK) also prevented retraction [3]. These data suggest

that the retractile response is actomyosin-driven, and without myosin force generation, the axon cannot retract itself. We observed that Blebbistatin-treated axons shortened after ablation, but at a reduced rate compared to controls, suggesting that additional mechanisms contribute to the retraction. These may include cytoskeletal depolymerisation triggered by elevated calcium levels or the action of enzymes such as calpains, which can disrupt microtubules (more detailed discussion in chapter 4).

Treatment with Taxol markedly slows axonal retraction. Taxol binds to and stabilises microtubules preventing depolymerisation, thereby reinforcing the axonal scaffold. In agreement with this, Datar et al. found that Taxol pretreatment strongly attenuated retraction after partial laser cut. In their measurements of retraction distance over time, Taxol-treated axons retracted only briefly and then stopped retraction much earlier than untreated control axons [99]. Thus, Taxol prevents the usual contraction by maintaining microtubule integrity. In essence, stabilised microtubules oppose the contractile forces, so the axon cannot shorten as much. In contrast, disrupting the axonal microtubule network promotes retraction. Early studies showed that loss of microtubules treated with Nocodazole and retraction induced by NOC-7 (Nitric oxide variant) causes enhanced retraction of axons [97]. More recent work confirms that pharmacological depolymerisation of microtubules (e.g. with nocodazole) induces collapse of severed axons [102]. For instance, Tymanskyj and Ma demonstrated that DRG axon branches retracted in response to

nocodazole-induced microtubule loss. In other words, microtubule destabilisation by nocodazole makes the axon more susceptible to contractile shortening after injury. It is thought that intact microtubules normally provide structural resistance to actomyosin tension, so their removal allows a more rapid retraction [97, 102]. In our partial-ablation experiments, nocodazole-treated axons retracted faster than controls, consistent with previous findings that microtubule loss accelerates retraction dynamics. However, complete transection of axons (full ablation) resulted in a slower retraction speed, and the underlying reasons for this difference are yet to be understood.

Actin filaments form a dynamic network that works with myosin II to generate contractile force. Latrunculin A, which depolymerises F-actin, prevents axonal retraction. Gallo showed that severing-induced retraction was abolished when actin was depolymerised [3]. In his experiments with retinal and chick DRG axons, Lat A completely blocked the shortening of severed segments. Similarly, Mutalik et al. reported that Lat A pretreatment completely abolished myosin-mediated axonal contractility in trypsin-detachment assays [61]. These results indicate that F-actin filaments are required for axon shortening. When actin is removed, there is less or no substrate for myosin-driven contraction. We still observe some retraction because Blebbistatin acts in a dose-dependent manner and may not fully inhibit myosin II activity. Additionally, residual F-actin

remaining after Latrunculin A treatment may support limited contractile activity, allowing some retraction to occur. Alternatively, the retraction could be partially driven by microtubule depolymerisation.

Conversely, Jasplakinolide stabilises F-actin by promoting actin polymerisation and inhibiting filament disassembly. By preventing actin turnover, Jasp shifts the balance toward irreversible contraction. In Gallo et al.'s studies, treatment with Jasp caused axons to retract [54]. This retraction was due to the action of endogenous myosin. Jasp-treated axons collapsed via a myosin-dependent mechanism, which is sensitive to ROCK and MLCK inhibitors [54]. Thus, locking actin into place is enough to unleash the contractile machinery and causes axonal retraction. However, either removing actin or preventing its turnover results in different outcomes. Actin removal halts contraction, while stabilisation of actin triggers contraction. But in our partial ablation experiment, the retraction after treatment with Jasp is slightly faster than in the control experiment. This could be because partial ablation leaves the membrane and most cytoskeletal components intact, preserving mechanical resistance from microtubules and crosslinking proteins. Additionally, actin structures beyond the periodic rings present in the axon may also contribute to its stability. As a result, even if contractility is slightly enhanced, the overall retraction is not much faster compared to control. However, in the case of full ablation, retraction is much slower compared to the control, and the underlying mechanism remains unclear.

When a combination of Taxol and Latrunculin A is used for experiments. The Taxol treatment is for 30 minutes, followed by an additional 30-minute treatment with Latrunculin A. First, the microtubules are stabilised, and, the actin polymerisation is blocked. The stabilised microtubules provide a rigid internal scaffold, while the absence of polymerised actin eliminates the contractile machinery. As a result, no significant retraction is observed.

In summary, the above discussion may indicate that axonal retraction after partial ablation requires coordinated action of actin and myosin against the microtubule framework. Disrupting actin or blocking myosin halts retraction, whereas drugs that weaken microtubules allow faster retraction in partial but not in full ablation. However, stabilising microtubules acts as a counterbalance to contractility and limits retraction. The combination of Taxol and Lat A blocks the axonal retraction.

Comparison of full and partial ablation shows that nocodazole and jasplakinolide produce divergent responses, which could arise from differences in boundary conditions. Full ablation creates two free ends and breaks symmetry, whereas in partial ablation, the tube remains intact and symmetry is preserved. Although the exact mechanism remains unclear, the explanation offered here provides one plausible interpretation.

3.7 Cytoskeletal response times

Full laser ablation of an axon causes a rapid viscoelastic retraction of segments, followed by slower cytoskeletal remodelling. In chick DRG axons, passive stretch-release experiments show that axons return to their resting length within 5–10 seconds once the external load is removed. In other words, the viscoelastic relaxation time of the axon is on the order of only a few seconds after sudden stretch [31].

Actin filaments turn over much faster than microtubules in neurons. In growth cone lamellipodia (e.g. cultured chick DRG or Retinal Ganglion neurons), F-actin is completely recycled on the order of 3–5 minutes in the lamellipodia of growth cones [54]. By contrast, axonal microtubules are very long-lived. Experiments in cultured neurons find an average MT half-life of ∼2.2 hours (132 min) in axons [103]. In other words, most microtubules persist for hours before complete turnover.

The rates of filament polymerisation also differ by filament type. Actin treadmilling in the growth cone enables steady retrograde motion. for example, lamellipodial protrusion and withdrawal typically occur at ∼1–4 μm/min [104]. Microtubule shrinkage rates during catastrophe are slower than polymerisation rates. Microtubule growth typically occurs at rates of 12–18 μm/min, consistent with values reported in Xenopus and rodent neurites [105].

Active contractile response after adhesion release also occurs on the order of seconds to minutes. In cultured chick DRG neurons, curved

axons treated with trypsin straighten via actomyosin contraction. A clear shape change is seen within 10–20 seconds of detachment, and the axon reaches its new (shortened) length within 1–5 minutes. Thus, actomyosin-driven straightening/shortening of an axon after release of attachments takes on the order of minutes [61]. Myosin-II inhibitors block this shortening, confirming it is active rather than purely elastic.

The timescales reported for cytoskeletal dynamics in neurons suggest that passive recoil occurs within seconds, actin turnover and contractile activity unfold over minutes, and microtubule turnover typically occurs over hours. Since our experimental timescale is on the order of minutes, we can reasonably neglect microtubule turnover during retraction. Actin turnover in structures like the lamellipodium occurs within 1–5 minutes; however, in the axonal shaft—where actin exists in more stable ring-like structures—turnover is likely slower. Thus, axonal retraction in our experiments is primarily governed by rapid passive recoil and actomyosin-driven contractility.

.

3.8 Axonal Twisting after Ablation

After laser ablation, axons often show twisting or rotational relaxation of the axonal segment shaft, which may indicate release of

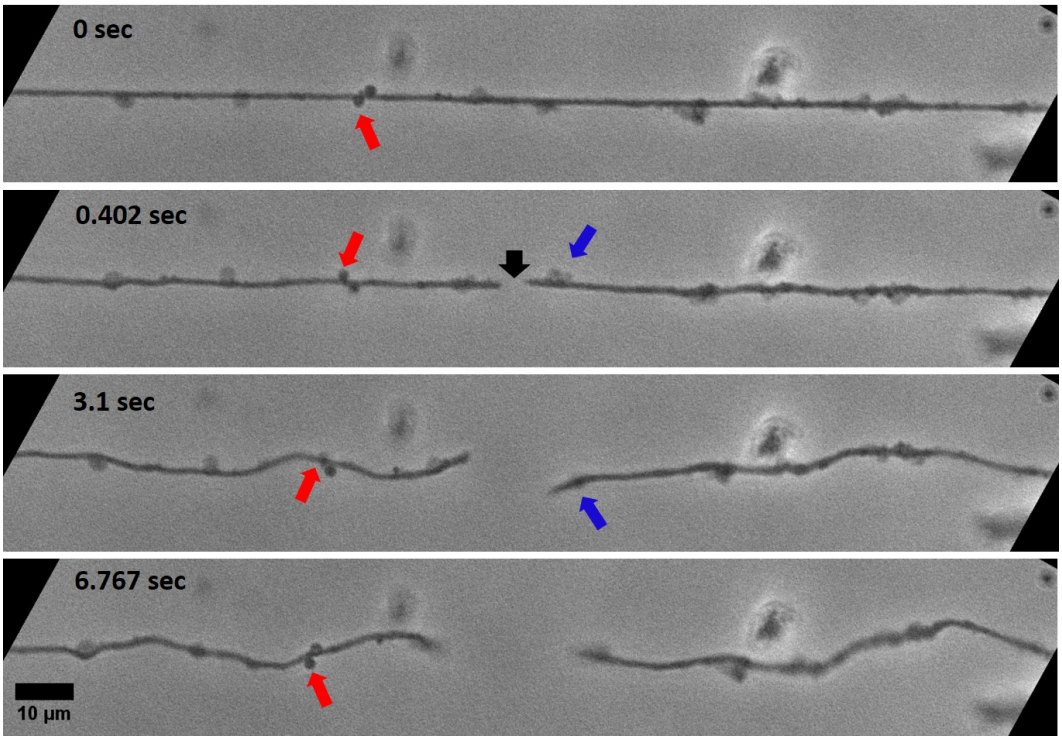

FIGURE 3.30: The image sequence illustrates axonal twisting in control axons following full ablation. The twisting is inferred from the movement of debris or uneven surface structures along the axon after ablation. These features, indicated by blue and red arrows, exhibit rotational displacement over time. The ablation site is marked by a bold black arrow.

torsional stress. This behaviour is likely a result of the pre-stressed composite structure of the axon. When the cut releases longitudinal tension, any built-up torsion in the microtubule bundle, for example, is relieved by rotation. The severed segment twists until internal stresses are minimal. In essence, the axon behaves like a pre-twisted elastic material. While the precise function of this twist release is not fully understood, it may help redistribute mechanical energy (analogy with the twisted rod) and cause cytoskeletal reorganisation at the cut site. The axonal twist after full ablation and partial ablation is shown in figure (3.30) and (3.31)

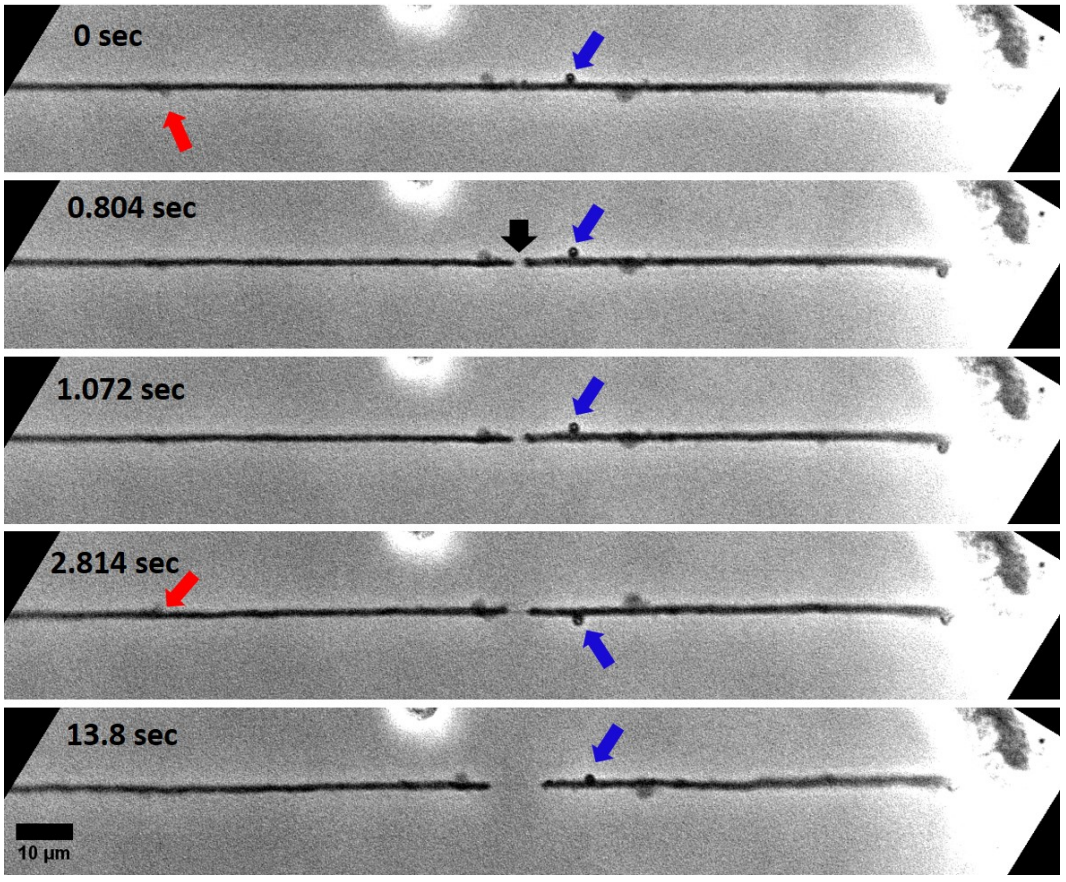

FIGURE 3.31: The image sequence shows axonal twisting in control axons following partial ablation. Twisting is suggested by the rotational movement of debris or irregular surface features along the axon, marked by red and blue arrows. The ablation site is indicated by a bold black arrow.

.

3.9 Some interesting observations

When control axons are partially ablated, the corresponding plots are shown in Figure 3.16. However, some interesting observations and details for the control axons after partial ablation are explained in the figure (3.32),(3.33) and (3.34).

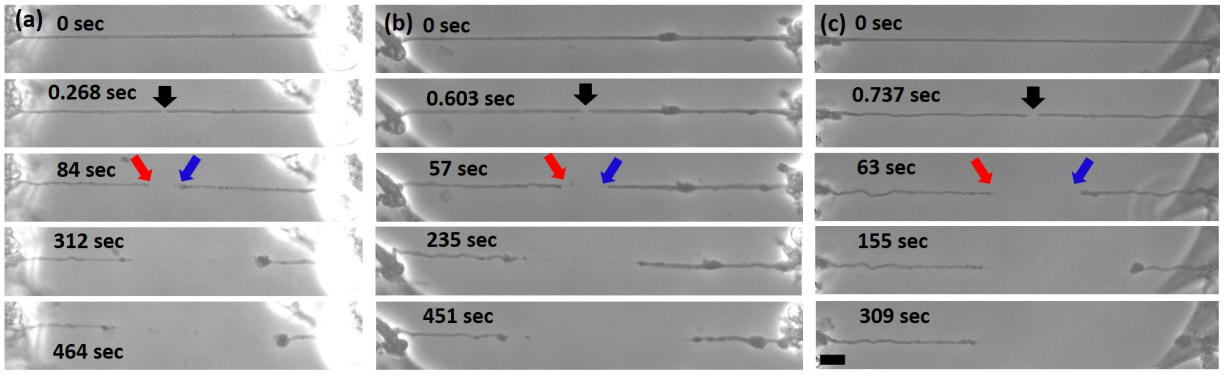

FIGURE 3.32: The image sequence shows the retraction behaviour of control axons following partial ablation. (a) The segment marked by the red and blue arrows shows no significant retraction between 312 sec and 464 sec. (b) The segment marked by the red arrow shows no significant retraction between 235 sec and 451 sec. (c) The segment marked by the red arrow exhibits minimal retraction between 63 sec and 306 sec.

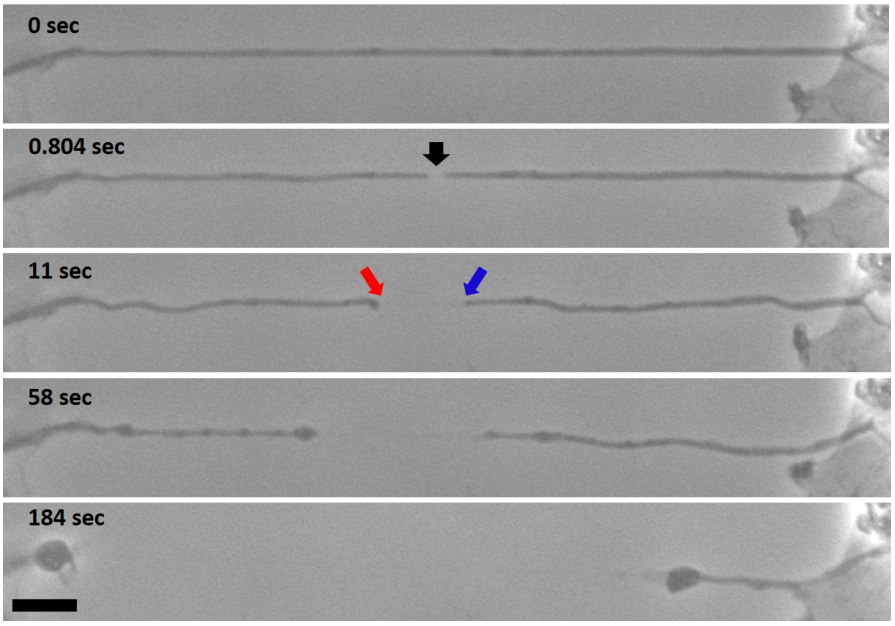

FIGURE 3.33: The image sequence of control axons following partial ablation shows no significant retraction between 11 seconds and 58 seconds in the segment indicated by the blue arrow. The contour length analysis of both segments is shown in figure (3.34).

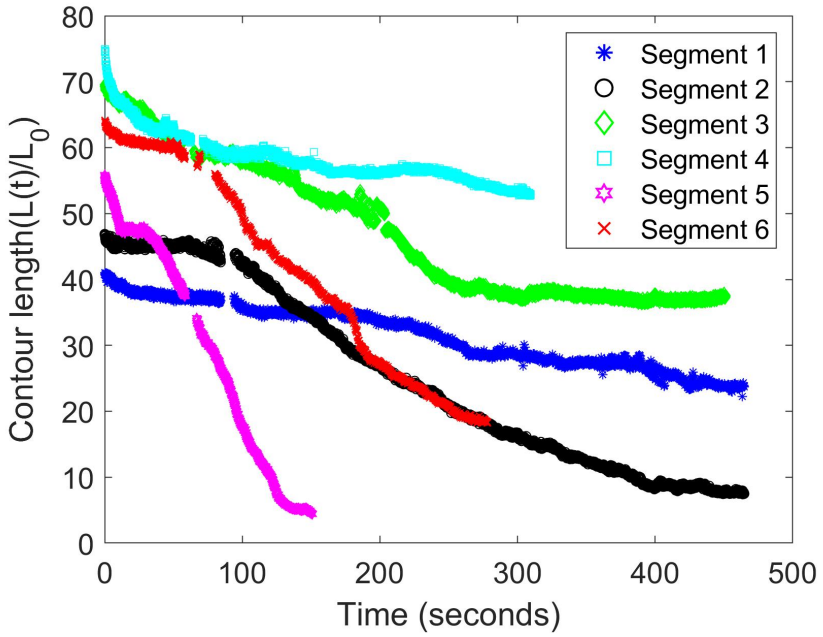

FIGURE 3.34: The blue asterisk and black circle plots represent the contour length data of the segments indicated by the red and blue arrows, respectively, in figure 3.32a. The green diamond plot corresponds to the segment marked by the red arrow in figure 3.32b, and the cyan square plot corresponds to the segment marked by the red arrow in figure 3.32c. All segments indicated by red arrows in figure 3.33 show either very slow retraction or no retraction after some time. The segment indicated by the blue arrow in the same figure initially retracts very slowly, followed by a sudden retraction. The magenta hexagon and red cross plots represent the contour length data of axonal segments marked by the red and blue arrows, respectively, in the figure 3.33. The segment marked by the red arrow (magenta hexagon) retracts initially, pauses, and then undergoes a sudden retraction. The segment marked by the blue arrow (red cross) also begins with very slow retraction, followed by a sudden contraction.

Chapter 4

The role of calcium in axonal retraction and recovery after partial laser ablation

In the previous chapter, we explored how different pharmacological treatments targeting cytoskeletal elements affect axonal retraction following both full and partial laser ablation. Our studies revealed that retraction dynamics are influenced by microtubules, actin filaments, and myosin II motor protein, with each component contributing in distinct ways. In addition to these structural factors, axonal injury may activate biochemical responses, particularly an increase in intracellular calcium concentration. This calcium influx occurs rapidly after ablation and may trigger calcium-dependent proteases. These enzymes can degrade essential cytoskeletal components, which may affect axonal retraction.

In this chapter, we will focus on the role of calcium after axonal ablation. Specifically, examining the effects of chelating calcium to limit intracellular calcium elevation. We aim to determine how this chelation influences retraction behaviour and the subsequent recovery of some key cytoskeletal components, namely actin and microtubules.

To fully comprehend the impact of calcium on axonal retraction and recovery, it is essential to understand the mechanisms that regulate its levels within the cell. The elevation of intracellular calcium after axonal injury involves a complex interplay between calcium influx from the extracellular space, release from intracellular stores, and active calcium clearance mechanisms. In the next section, we will explore the sources of calcium within axons, the pathways through which calcium levels rise following injury, and the cellular mechanisms that restore calcium to its previous (pre-ablation) levels, thereby modulating the cellular response to injury. Understanding these dynamics is critical for unravelling how calcium influences retraction processes after partial ablation.

4.1 Role of calcium in cells: from homeostasis to degeneration

4.1.1 Calcium homeostasis and its regulation

Calcium plays a major role in maintaining a great variety of neuronal processes that are crucial for neuronal function, such as neurotransmission and synaptic plasticity, along with the regulation of axonal growth, development, and regeneration [106]. Maintaining calcium homeostasis is crucial for neurons to ensure proper signalling, plasticity, and survival.

Calcium homeostasis is the process of regulating intracellular Ca^{++} levels (in the nM range) compared to the extracellular milieu (in the mM range). In general, increases in Ca^{++} are typically short (ranging from milliseconds to a few minutes) because of a complex system of calcium buffers, pumps, channels, and exchangers found in cell membranes and the membranes of intracellular calcium-storage organelles, such as the endoplasmic reticulum. Many proteins sense and bind to elevated Ca^{++}, leading to the modulation of pumps and channels to regulate the Ca^{++} [107]. Calmodulin is one of the sensor proteins that may detect and bind Ca^{++} by undergoing a conformational change. It may trigger calcium pumps such as the Plasma Membrane Calcium ATPase (PMCA) and the Sarco/Endoplasmic Reticulum Calcium ATPase (SERCA) to decrease intracellular Ca^{++} concentrations. PMCA actively removes excess Ca^{++} by actively

pumping calcium ions out of the cell using ATP hydrolysis. SERCA on the membrane of the endoplasmic reticulum (ER)(in non-muscle cells) functions as a calcium pump that prevents excess cytosolic Ca^{++} accumulation by transporting calcium into the ER. Additionally, Na^{+}/Ca^{++} exchanger (NCX) rapidly reduces Ca^{++} levels by extruding Ca^{++} out of the cell in exchange of Na^{+} ions [108, 109].

4.1.2 Mechanisms of Ca^{++} entry

Different cellular stimuli, including membrane depolarization, extracellular signalling molecules, or intracellular messengers, lead to a rise in Ca^{++} from 100 nM to 1 μM or higher. Calcium ions (Ca^{++}) enter cells via voltage-gated calcium channels (VGCCs) and ligand-gated channels (LGC) [110, 111]. For example, VGCCs (e.g. T-type channel) activate and open by conformational changes when the membrane depolarises, permitting the influx of Ca^{++} ions in the cell [112]. Ligand-gated channels become active when excitatory neurotransmitters, such as glutamate, engage with them during neurotransmission. For instance, N-methyl-D-aspartate receptors (NADARs) are a type of LGC that respond to glutamate binding, which facilitates the entry of Ca^{++} into the cell, leading to a regulated increase of intracellular Ca^{++}, essential for neuronal signalling within the mammalian CNS. [108, 111]. Additionally, the release of Ca^{++} from internal stores like the endoplasmic reticulum through intracellular channels plays a role in increasing the levels of cytosolic Ca^{++} [110].

Store-operated calcium channels (SOCCs) are plasma membrane channels that serve as a significant route for Ca^{++} entry into the cytoplasm. SOCCs activate during store-operated calcium entry (SOCE) when there is a calcium depletion in the endoplasmic reticulum. STIM proteins act as sensors for Ca^{++} ions in the ER, while Orai proteins function as SOCCs, together enabling SOCE. When calcium levels in the ER decrease, STIM proteins move to the junctions between the ER and the plasma membrane, where they engage and activate Orai channels located in the plasma membrane, initiating calcium influx to restore the balance of intracellular calcium [109, 113].

Transient receptor potential (TRP) channels are cation channels permeable to calcium and involved in various sensory responses such as changes in temperature and pH. There are multiple ways TRPs may affect cellular calcium signalling. These channels can directly trigger cellular calcium signals in response to various stimuli. Additionally, as nonselective cation channels, the activation of TRP channels results in membrane depolarization, which affects Ca^{++} influx through VGCCs and SOCCs. Lastly, Ca^{++} affects the activity of most TRP channels, enabling them to act as molecular effectors in response to intracellular Ca^{++} signals [109, 114].

Intracellular (Ca^{++}) stores also contribute to increased levels of intercellular calcium. Cells release Ca^{++} from the endoplasmic reticulum through inositol 1,4,5-trisphosphate receptors (IP3Rs). These receptors are ligand-gated calcium channels that allow Ca^{++} to flow from

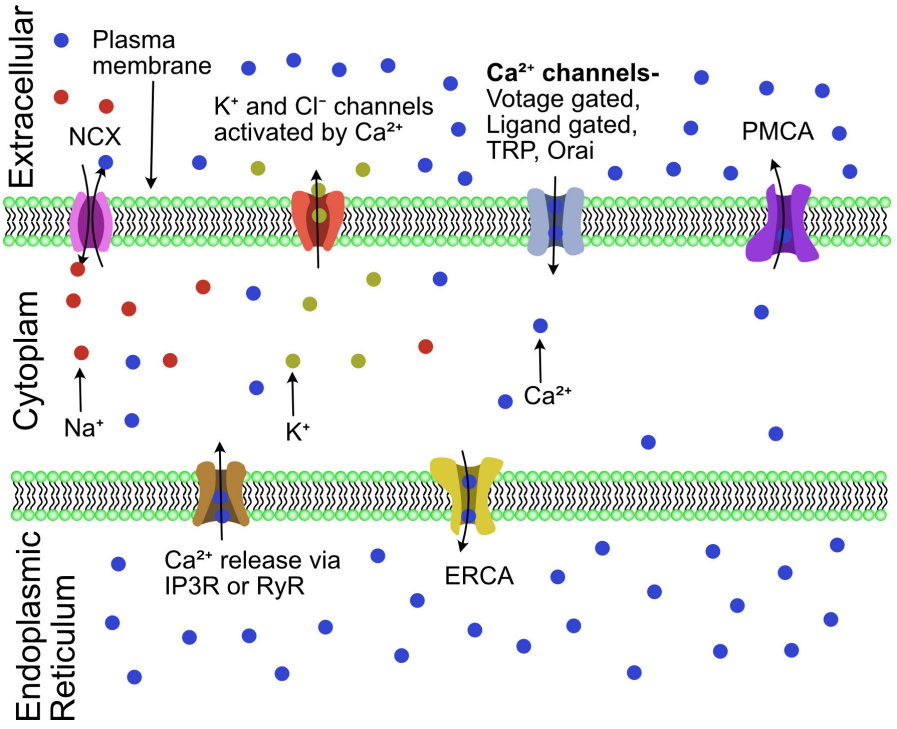

FIGURE 4.1: **Schematic of Ca^{++} regulation and signalling in cells**. At rest, cytoplasmic Ca^{++} is maintained at ∼nM levels by active expulsion via the Na^{+}/Ca^{++} exchanger (NCX) and plasma membrane Ca^{++} ATPase (PMCA), and by sequestration into the endoplasmic reticulum (ER) via the endoplasmic reticulum Ca^{++} ATPase (ERCA). Elevated intracellular Ca^{++} activates K^{+} channels and, in some cells, Cl^{-} channels, leading to hyperpolarisation. Excitatory Ca^{++} signalling is triggered by voltage changes or ligand binding, activating plasma membrane channels. Initial Ca^{++} influx can induce further release from ER stores via CCa^{++}-sensitive RyRs) and IP3Rs.

internal stores into the cytoplasm when IP3 (the ligand) binds to them. [109, 115]. The schematic of Ca^{++} release from the extracellular space and intracellular stores is shown in the figure 4.1.

Stretch-activated calcium channels (SACs) - These are mechanosensitive ion channels that mediate Ca^{++} entry in response to a diverse range of mechanical stimuli such as stretch, shear stress, or osmotic changes [116]. Piezo1 and Piezo2 are the two main SACs found in neurons that can be activated by mechanical deformation of lipid

bilayer or interaction with cytoskeletal elements leading to the sudden influx of Ca^{++} into the cell [117, 118]. The biophysical properties of SACs are characterised using patch-clamp electrophysiology, showing that ionic (inward) currents induced by mechanical stimuli (negative pressure (suction)) and substrate indentation were blocked by SAC subtype-specific inhibitors, including GsMTx4 and Gadolinium (Gd^{3+}) to distinguish SACs from voltage-gated calcium channels (VGCCs) [116, 119, 120]. Genetic knockout (KO) models provide experimental support for the involvement of SACs, as mechanosensitive Ca^{++} currents are lost in Piezo2 KO neurons, demonstrating that Piezo channels are critical sensory neuron mechanotransducers [118]. Moreover, calcium imaging studies using fluorescent molecules such as Fura-2 or genetically encoded calcium indicator (GECI) proteins are used to measure the activity of mechanically activated cation channels [116]. For example, applying fluid shear stress to MDCK cells increases Ca^{++} influx into the cytoplasm [121]. Piezo1 is crucial for the Ca^{++} influx induced by mechanical force in red blood cells. Selective removal of Piezo1 from red blood cells in adult mice leads to increased fragility [122]. These results together provide strong evidence that SACs function as a major pathway for mechanosensitive Ca^{++} entry.

Several models explain the mechanism of cation entry into cells. The force-from-lipid model proposes that piezo channels can detect tension across the lipid bilayer, while mechanical deformation causes the channel to open up through stretching of the membrane. In

this model, piezo channels can function independently of the cytoskeleton, indicating the lipid bilayer primarily drives force sensing. The force-from-tether model, on the other hand, suggests that piezo channels could be attached to cytoskeletal components or extracellular matrix structures via tether protein. In this model, external forces pass through these tethers, influencing the conformation of the channel and resulting in its activation. These models are reviewed in [123].

4.1.3 Calcium stores and sequestration

Calcium, which plays a crucial role in intracellular signalling, is sequestered in organelles such as the endoplasmic reticulum (ER) and the mitochondria. These Ca^{++} stores are tightly regulated by organelle efflux and uptake. The outer mitochondrial membrane (OMM) allows Ca^{++} to pass through via voltage-dependent anion channels (VDACs) known as mitochondrial porins. The mitochondrial calcium uniporter (MCU) in the inner membrane enables rapid uptake of Ca^{++} driven by the mitochondrial membrane potential. In intact neurons, MCU activation is strongly influenced by cytosolic Ca^{++} levels, with uptake occurring at concentrations as low as 200–300 nM [124–126].

The neuronal endoplasmic reticulum contains sarcoplasmic/endoplasmic reticulum Ca^{++}-ATPase (SERCA) pumps responsible for sequestering Ca^{++} into the ER. ER also contain high levels of calcium-binding proteins like calreticulin and calbindin for calcium storage, preventing harmful accumulation in the cytoplasm. Neurons also have calcium channels, including inositol 1,4,5-trisphosphate receptors (IP3Rs) and ryanodine receptors (RyRs), which control the release of Ca^{++} from the ER to the cytosol [127].

Ca^{++} stores act as both buffers and sources of Ca^{++}, with their function depending on their filling state. When empty, they absorb Ca^{++}, which limits stimulus-evoked transients; when filled, they release Ca^{++}, thereby enhancing intracellular signals [127].

4.1.4 Calcium induced calcium release (CICR), waves, oscillations

CICR

Calcium-induced calcium release is an amplifying mechanism where calcium influx into the cytoplasm stimulates additional calcium release from internal stores (ER and mitochondria), enhancing the signal [127]. For instance, the entry of Ca^{++} during action potentials has been demonstrated to initiate calcium release from ryanodine-sensitive stores through CICR [128].

Ca^{++} release from the endoplasmic reticulum in response to extracellular stimuli, mainly involves two families of intracellular channels.

The first one is ryanodine receptors (RyR), and the other one is inositol 1,4,5-trisphosphate receptors (IP3Rs). Both of these channels respond to Ca^{++}, and the CICR mechanism plays a role in the quick increase of Ca^{++} concentrations [108].

In IP3Rs, the main factors involved are IP3 molecule and Ca^{++}. IP3 binds to receptors, causing a conformational change and enhancing their sensitivity to calcium. This effect exhibits biphasic behaviour (it stimulates at low concentrations but becomes inhibitory at the higher levels that arise following Ca^{++} release). The regulation of Ca^{++} takes place through both the direct interaction of Ca^{++} with the receptor and indirectly through calmodulin (CaM), which can activate or inhibit the response. A calcium-binding protein (CaBP) was also shown to initiate Ca^{++} release even without IP3 [108, 129–131].

Along with IP3Rs, RYRs respond to Ca^{++} triggering further intracellular Ca^{++} release and amplifying signals in neurons, similar to cardiac muscle excitation-contraction coupling. These receptors are activated through interactions with voltage-gated Ca^{++} channels (e.g. L-type) in the plasma membrane or by Ca^{++} itself, particularly during depolarization. The signal amplification varies among neuron types, including DRG, Purkinje, and hippocampal neurons, influenced by cytosolic Ca^{++} levels and neurotransmitters like glutamate and caffeine. Moreover, calmodulin (CaM) in both its Ca^{++} -bound and Ca^{++}-free forms regulate RyR2 activity, ensuring precise

control of intracellular Ca^{++} signalling in muscle contraction, neurotransmission, and other physiological processes. [106, 108, 129]

Ca^{++} oscillations

Calcium enters the intracellular space from the extracellular environment or internal stores, elevating it. This causes a rapid rise in intracellular calcium levels, followed by decay, forming a cycle of calcium oscillations. These oscillations are regulated by feedback mechanisms that ensure synchronised activation and quick deactivation of calcium channels. This oscillation is shown by both IP3 and RY receptors [115]. IP3Rs respond in a biphasic manner to cytosolic Ca^{++}, where low concentrations stimulate Ca^{++} release, while higher levels inhibit it. Activating IP3Rs releases Ca^{++}, initially limited but rising through CICR as cytosolic Ca^{++} levels increase. When Ca^{++} reaches an inhibitory level, IP3Rs close, and the cell returns to resting conditions by moving Ca^{++} back into stores via SERCA or out of the cell via PMCA. Additionally, extracellular Ca^{++} entry helps restore intracellular stores and directly affects the frequency of oscillations, emphasising the importance of intracellular Ca^{++} in maintaining these cycles [132]. Moreover, RyRs activate and inhibit at micromolar and millimolar ranges of cytosolic calcium, respectively, facilitating Ca^{++} oscillations [108, 115].

The process of calcium oscillation for transferring information within cells offers several advantages. Sustaining elevated levels of cytosolic Ca^{++} demands significant energy to manage calcium transport

mechanisms within the cell, and excessively high Ca^{++} levels can be detrimental. Consequently, calcium oscillations is thought to provide a more energy-efficient and controlled method of signalling [132].

Ca^{++} waves

In contrast to oscillations that are local and recurring, calcium waves travel throughout the cell. The waves are spread through the cytoplasm by the sequential release and diffusion of Ca^{++} from the clusters of IP3Rs or RyRs located on the ER. The clusters of IP3Rs generate localized Ca^{++} puffs, while RyRs typically organize into clusters of four to six channels, resulting in the generation of Ca^{++} sparks. Both of these events cause short, localized rises in cytosolic calcium concentrations (about 50–600 nM), which extend over distances of 2–6 µm and last for less than one second [108, 133].

The Ca^{++} that is released from a cluster can diffuse to adjacent sites and cause further activation. This propagation mechanism enables local Ca^{++} signals to propagate to become global Ca^{++} waves and impact other cellular processes. In case of low stimulation, Ca^{++} puffs are localized. However, with increased stimulation, Ca^{++} released from one cluster can activate neighbouring clusters through a 'fire-diffuse-fire'[1] [134] mechanism, resulting in widespread Ca^{++} waves [132].

[1]The fire-diffuse-fire (FDF) mechanism explains the spread of intracellular Ca^{++} signals through localized release, diffusion, and reactivation. Ca^{++} release channels like IP3Rs or RyRs create localized bursts called puffs or sparks. The released Ca^{++} diffuses to increase local concentration, activating nearby receptors and triggering more Ca^{++} release, allowing waves to spread throughout the cell.

IP3Rs and RyRs are found throughout the ER, but their distribution is not uniform. While IP3Rs and RyRs tend to cluster independently, they can also form mixed clusters. In these mixed clusters, IP3R-mediated Ca^{++} release activates adjacent RyRs, further enhancing Ca^{++} signalling and facilitating effective intracellular communication [133].

4.1.5 Effects of Excess Calcium: Activation of Enzymes and Breakdown of the Cytoskeleton

The regulation of calcium signalling is important for the proper functioning of cells, while excess calcium may cause damage. Increased levels of intracellular Ca^{++} are a common characteristic of injury and neurodegeneration [135, 136]. Excess calcium triggers harmful downstream processes, such as oxidative stress, mitochondrial dysfunction, and the activation of calcium-dependent proteases. These proteases can be seen as the agents responsible for causing cellular damage. While many proteases can contribute to cell degradation, calpains are the most directly activated by elevated calcium levels [136].

Calpains are a group of intracellular cysteine proteases that become active in response to increased calcium levels within the cell. While numerous isoforms of calpain have been identified, most research has focused on two main types: μ-calpain (calpain-1) and m-calpain (calpain-2). μ-Calpain has a relatively high affinity for Ca^{++} found

in the cytosol or near the membrane, activating at micromolar concentrations. In contrast, m-calpain has a lower affinity for Ca^{++} and is located at the membrane, requiring millimolar Ca^{++} levels for activation in vitro [137]. So when intracellular Ca^{++} elevates, it may trigger calpains and degrade a wide range of functional and structural proteins, contributing to pathological changes associated with neurodegenerative disorders and injury [101, 137]. Neuronal calpain activation has been observed within minutes to hours after either contusive or diffuse brain trauma in animals, suggesting that calpains are an early mediator of neuronal damage [138]. Additionally, m-Calpain mediates the proteolytic cleavage of actin into smaller fragments in lens cells [139].

Calpain plays a crucial role in axonal dysfunction and pathology following mechanical deformation or transection by targeting the axonal cytoskeleton. Composed primarily of neurofilaments and microtubules, the cytoskeletal structure is highly susceptible to calpain-mediated proteolysis, leading to its disruption and contributing to axonal damage [140].

In vitro study with microtubules examines the proteolysis of tubulin and microtubule-associated proteins (MAPs) 1 and 2 by calpain I and II, highlighting differences in their susceptibility based on microtubule assembly. It finds that disassembled tubulin and MAPs are more prone to degradation by calpain than those within assembled microtubules. These results indicate that microtubule stability

impacts sensitivity to calpain-mediated proteolysis, with potential implications for cytoskeletal regulation in various conditions [141].

Another in vitro study examines a calcium-activated neutral protease (CANP) or calpain in the peripheral nerve, which is activated by micromolar Ca^{++} and selectively degrades neurofilament proteins. The findings suggest CANP contributes to axonal degeneration and structural instability under calcium dysregulation [142, 143]. Moreover, neurofilament degradation under calcium-activated proteolysis is shown using immunoblotting [144].

Moreover, in vitro calcium-induced microtubule disassembly is reported, showing that even low Ca^{++} levels disrupt tubulin-tubulin interactions, leading to depolymerization. It also highlights the role of calmodulin[2] in enhancing this effect by interacting with microtubule-associated proteins (MAPs) and reducing their stabilizing function. These findings indicate that calcium and calmodulin pathways both may regulate microtubule stability [147, 148].

It has been shown that calmodulin enhances the calpain-mediated breakdown of brain spectrin, a vital cytoskeletal protein for neuronal structure. It likely interacts with calpain by modulating calcium binding, facilitating spectrin proteolysis [146].

Another study examines the role of calpain in pyroptosis, a type of inflammatory cell death. It explores that calpain cleaves vimentin,

[2]Calmodulin is a calcium-binding protein activated by increased intracellular calcium levels [145]. It can directly bind to calpain and enhance its proteolytic activity. [146]

an essential intermediate filament protein, resulting in cytoskeletal disassembly and subsequent cell rupture in macrophages [149].

Weisenberg et al demonstrated that Ca^{++} alone directly affects microtubule assembly in vitro and is highly dependent on calcium concentration. Low calcium concentrations (≤ 0.1 μM) promote tubulin polymerization, while increased calcium levels (≥ 1 μM) inhibit microtubule assembly by destabilizing tubulin interactions [147].

It can be concluded that elevated intracellular calcium leads to the activation of proteases, resulting in the degradation of cytoskeletal proteins and causing the disruption of neuronal structures via multiple and not fully understood mechanisms.

4.1.6 Axonal injury/disease

Axonal damage and neurodegenerative diseases are closely linked to impaired Ca^{++} regulation. In the case of traumatic brain injury (TBI), stroke, or neurodegenerative diseases like amyotrophic lateral sclerosis (ALS) and Alzheimer's disease (AD), a rapid increase of intracellular Ca^{++} may initiate a series of harmful consequences [137, 150].

The cells maintain their Ca^{++} level within the physiological range when unperturbed. However, when cells are perturbed, such as stretching, transection, or crush/compression, the Ca^{++} level rises

from the normal range. The sudden rise of axonal Ca^{++} level beyond the typical range after axonal injury is demonstrated in axotomy studies in cultured Aplysia neurons [151]. This increase in Ca^{++} levels can trigger axonal degeneration, as demonstrated using the calcium ionophores that elevate Ca^{++} and cause axonal damage within hours. Conversely, this process can be prevented by inhibiting voltage-gated calcium channels (VGCCs) [5]. The axonal injury in Ca^{++}-free media shows no rise in Ca^{++}. However, substituting the Ca^{++}-free media with Ca^{++}-rich media post-injury results in an increase in intra-axonal Ca^{++} levels [152]. The intracellular and extracellular Ca^{++} chelation also prevents axonal degeneration. The present perspective is that the rise in axonal Ca^{++} from the extracellular environment following axotomy triggers calpains, contributing to axonal disintegration [153]. Additionally, following an ischemic injury, the early suppression of calcium release from internal stores hinders the loss of axonal activity [154]. There could be multiple ways in which axonal calcium could be engaged in axonal degeneration processes.

However, the signal or driving force that promotes Ca^{++} entry into the injured axon is less well defined. Several reports suggest that decreased activity of Na^{+}/K^{+} ATPase due to energy failure (shortage of ATP production) or mechanical disruption of surface membrane from nerve injuries leads to initial Na^{+} influx through tetrodotoxin (TTX)-sensitive Na^{+} channels. This then depolarises the membrane to open voltage-gated Ca^{++} channels as well as reverses the normal

direction of Na^+/Ca^{++} exchanger activity to collectively drive Ca^{++} influx [155]. However, the addition of TTX, which blocks the inward Na^+ current and attenuates intra-axonal Ca^{++} levels, fails to delay significant axon degeneration after axotomy [5, 152]. Moreover, a decrease in intra-axonal K^+ is reported to precede the rise of Ca^{++} and Na^+ levels in transected sciatic nerves, raising the possibility that loss of intra-axonal K^+ potential may provide a more critical electrochemical driving force for Ca^{++} influx after nerve injuries [156].

Axonal damage in a Ca^{++}-free extracellular milieu results in no change in intracellular Ca^{++} levels, suggesting the critical role of extracellular Ca^{++} in post-traumatic Ca^{++} elevation. In contrast, when axons are transected in a Ca^{++}-rich environment, intracellular Ca^{++} increases due to a combination of influx through membrane pores, activation of VGCCs [5], and CICR from internal stores [157]. Ca^{++} released from the ER via IP3Rs and RyRs contributes to mitochondrial Ca^{++} overload, leading to energy loss, elevated reactive oxygen species (ROS), reduced ATP production, and ultimately axon fragmentation [152, 153]. This energy deficit disrupts axonal transport, destabilises the cytoskeleton, and compromises membrane integrity. Moreover, elevated Ca^{++} also activates proteases such as calpains, which degrade cytoskeletal components. Notably, m-calpain requires intracellular Ca^{++} concentrations $\geq$200 μM to induce axonal degeneration [5]. Ultrastructural studies of white matter anoxia further support this, showing that prolonged high Ca^{++} levels are associated

with neurofilament and microtubule breakdown [158]. Dysregulated Ca^{++} signalling also contributes to neurodegenerative diseases such as Alzheimer's disease (AD), where excessive ER Ca^{++} release increases amyloid-β toxicity and tau hyperphosphorylation [150].

4.2 Methods to study Ca^{++} elevation

The investigation of calcium dynamics within cells depends on various calcium indicators, calcium channel blockers, receptor blockers and inhibitors. There are some of them listed here.

4.2.1 Fluorescent calcium indicators

Fluo-4: These dyes, which utilize a single wavelength, are used to track intracellular calcium concentrations in living cells. They increase fluorescence intensity upon binding to calcium, with an excitation peak around 488 nm.

Fura-2: This dye is a ratiometric calcium indicator dye that measures intracellular calcium concentration by changing its excitation peak from 380 nm (free) to 340 nm (calcium-bound) with an emission at approximately 500 nm. It thus makes precise measurements of calcium by comparing two-wavelength fluorescence. Moreover, ratiometric analysis measures calcium levels in cells by comparing two fluorescence signals—one that increases and one that decreases with changes in calcium. Using the ratio of these signals helps eliminate

errors from uneven dye amounts and signal fading, improving measurement accuracy [159].

4.2.2 Calcium channel blockers

Gadolinium: A non-selective blocker of calcium channels that are activated by mechanical stimuli and stretching.

Nifedipine: A dihydropyridine calcium channel blocker that inhibits L-type voltage-gated calcium channels and is commonly used in studies of cardiac and neuronal calcium dynamics.

4.2.3 Calcium chelators

BAPTA-AM: It is a cell-permeable calcium chelator used to reduce intracellular calcium levels. The AM ester form allows it to cross the cell membrane easily. Inside the cell, esterases remove the AM groups, converting them to active BAPTA, which binds free calcium ions with high affinity.

EGTA: It is a cell membrane-impermeable calcium chelator that binds to calcium ions with high affinity, making it ideal for selectively lowering extracellular calcium levels. It aids in the investigation of the contributions of both intracellular and extracellular calcium to cellular processes.

4.2.4 Protease Inhibitors

Numerous calpain inhibitors are used to prevent calpain-driven proteolysis in studies investigating calcium-triggered cytoskeletal breakdown. However, MDL-28170 and Calpeptin are two calpain inhibitors targeting calpain 1 and calpain 2.

4.2.5 Intracellular receptor blocker

To inhibit the release of calcium from the endoplasmic reticulum (ER), the two receptors (IP3R and RyR) can be targeted.

IP3R inhibitor: It can be inhibited using either xestospongin C, a direct IP3R blocker, or U73122, a phospholipase C (PLC) inhibitor that indirectly prevents IP3R activation by reducing IP3 production.

RyR inhibitor: Dantrolene works by directly inhibiting the release of calcium from the endoplasmic reticulum (ER) by stabilizing the closed state of ryanodine receptors (RyRs). In contrast, ryanodine can modulate these receptors in two ways: at low concentrations, it keeps the channel open, while at higher concentrations, it blocks the receptor's activity. Ruthenium red is also a widely used blocker of (RyR) [160].

Along with all the inhibitors listed above, bepridil is used to block the sodium-calcium exchanger, while ω-conotoxin MVIIC is used to block VGCCs.

4.3 Experimental Insights of calcium in axons following partial ablation

Building on our understanding of the pathways governing calcium elevation and clearance, we next sought to experimentally verify how intracellular calcium levels change in response to partial laser ablation. To do this, we employed live-cell fluorescence imaging using calcium-sensitive dyes, enabling real-time visualisation of calcium transients in axons immediately after injury. These observations were further complemented by calcium chelation experiments using EGTA to suppress extracellular calcium influx. Together, these approaches will allow direct assessment of the magnitude of calcium levels before and after ablation, as well as the temporal evolution of calcium elevation.

4.3.1 Laser-ablation causes Ca^{++} elevation in axons

In order to explore the possible role of free calcium in driving axonal retraction after ablation, we imaged intracellular free Ca^{++} levels using Fluo4-AM dye. This dye binds to free intracellular Ca^{++} and exhibits increased fluorescence upon binding, allowing us to monitor changes in calcium concentration in real time. As shown in Figure 4.2a, there is a sudden and significant increase in the intracellular Ca^{++} level when the axon is ablated. To identify the mechanisms of calcium elevation, we pretreated neurons with either EGTA (5 mM), a calcium chelator that selectively binds extracellular Ca^{++},

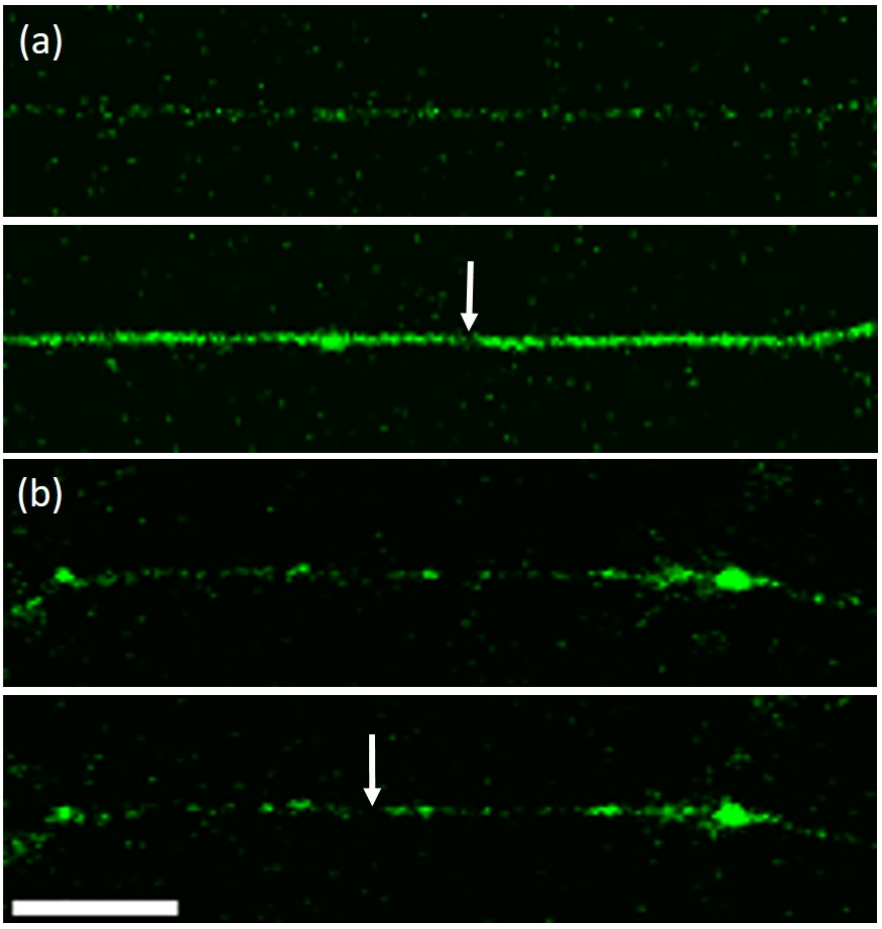

FIGURE 4.2: **Partial ablation causes Ca^{++} elevation in axons. (a)** Images of an axon labeled with the Ca^{++} indicator Fluo4-AM taken before ablation (above) and immediately after ablation (below). A sudden increase in fluorescence intensity is seen in every ablated axon. The white arrow marks the point of ablation and the scale bar is 20 μm. **(b)** Images of an axon pretreated with the calcium chelator EGTA and ablated as before. No significant increase in fluorescence is seen in this case.

or BAPTA-AM (10 μM), a membrane-permeable chelator that sequesters intracellular Ca^{++}. Both treatments were effective in significantly suppressing the calcium influx observed after ablation. In particular, as shown in Figure 4.2b, axons treated with EGTA exhibited a noticeably reduced fluorescence response post-ablation. The quantitative comparisons of fluorescence intensity changes across conditions for full and partial ablation are summarised in Figure 4.3 and 4.4, respectively. These data suggest that the elevation in Ca^{++} is

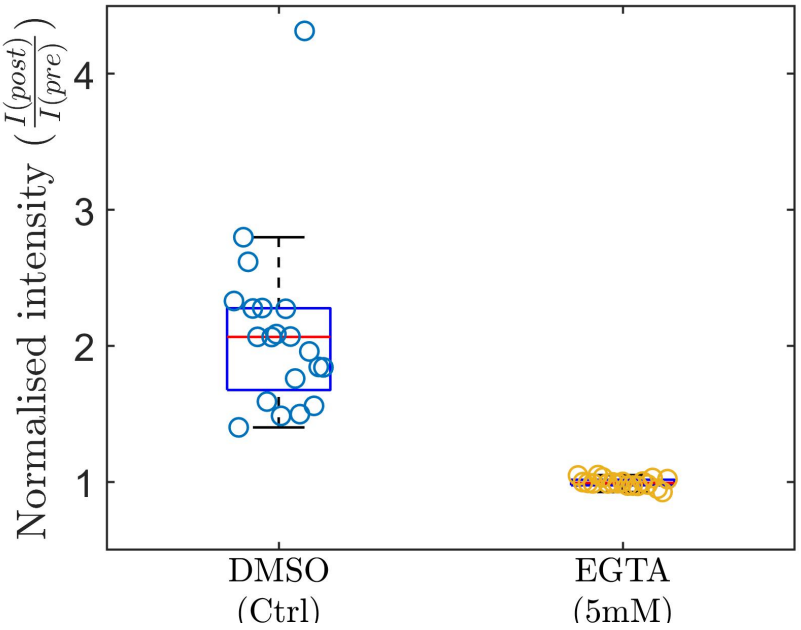

FIGURE 4.3: **Measurement of Ca^{++} influx following full ablation.** Normalised fluorescence intensity (I(post)/ I(pre)) following full ablation is shown for control axons (n = 20) and axons in EGTA-containing medium (n = 19). I(pre) and I(post) represent the fluorescence intensities measured just before and immediately after ablation, respectively. The concentrations used are indicated in the plot. Error bars represent the standard error of the mean.

triggered by entry of extracellular Ca^{++}, possibly at the ablation point. Quantification of intensity as a function of time can be performed for partial ablation, as the axon remains almost straight. Measurement of the Fluo4-AM fluorescence intensity shows that the Ca^{++} elevation post-ablation is sudden and reaches peak intensity within a few seconds. This is followed by an exponential decay of free calcium levels as can be seen from the inset of Fig. 4.4. This could indicate the activation of calcium clearance mechanisms that buffer intracellular calcium levels. The calcium level seems to decay to a value that is higher than the pre-ablation value, but this could be because of the limited observation time in our experiments, which

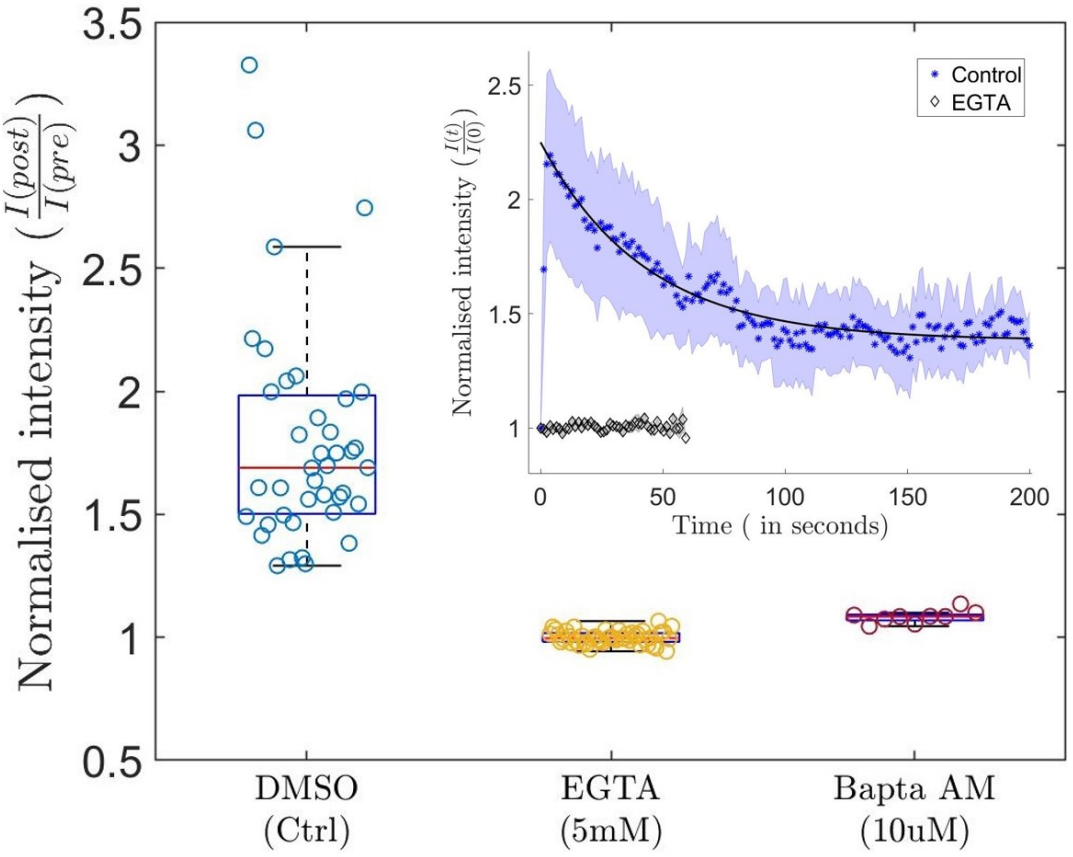

FIGURE 4.4: **Quantification of Ca^{++} elevation after partial ablation** Data showing the normalised fluorescence intensity (I(post)/ I(pre)) after partial ablation for control axons (n = 40), axons grown in medium containing EGTA (n = 47) and for axons treated with BAPTA AM (n = 9). I(pre) and I(post) are the intensities before and just after ablation, respectively. The concentrations used are indicated in the plot. The error bars are standard errors of the mean. **(Inset)** Plots showing the time evolution of intracellular free calcium for control axons and for axons in medium containing EGTA. Ablation was performed at time t = 0 s. The data points are the averages and the shaded regions are standard errors of the mean for control axons (n = 5) and EGTA-treated axons (n = 7). A sharp increase in Ca^{++} followed by a decay can be seen for the control axon, whereas the EGTA treated axon show a nearly constant base value of intensity. For control axons, a fit to an exponential function is shown using a solid black line, which yields a Ca^{++} decay time of $\tau = 42.7$ sec.

did not capture longer-term recovery dynamics. An alternative possibility is that the residual elevation represents a new steady-state level of intracellular Ca^{++}.

In neurons, cytoskeletal architecture and Ca^{++} handling are developmentally tuned for growth and plasticity: in immature neurons,

microtubules are highly dynamic (high tyrosination/ low acetylation) and the axonal actin-spectrin periodic scaffold is still maturing, together favouring viscoelastic recoil and rapid post-injury remodelling [16, 19, 161]. By contrast, adult axons exhibit stabilised, acetylated microtubule bundles and a robust spectrin lattice. With maturation, endogenous Ca^{++} buffers (e.g., calbindin/parvalbumin) and extrusion systems (PMCA, NCX, SERCA, mitochondrial uptake) increase, so mature axons clear Ca^{++} faster, whereas immature axons show larger, slower Ca^{++} transients, i.e., they take longer to buffer [162, 163]. In our experiments, we used neurons from E8 and E9 chick embryos cultured for 4 DIV. At this stage, the actin–spectrin skeleton is already well developed, while microtubule acetylation and other maturation-associated changes continue to progress, allowing us to capture the properties of developing axons.

4.3.2 Chelation of Ca^{++} allows for axonal recovery post ablation

After confirming that calcium levels rise in calcium-rich media but not in calcium-free media following ablation, we next performed ablation in calcium-rich conditions to study the retraction responses. Although both full and partial ablation induce elevation, full ablation poses challenges for studying retraction over extended periods due to the segment drifting out of focus. Therefore, partial ablation serves as a better model system to explore both short-term and long-term dynamics. In this case, the partially ablated axons

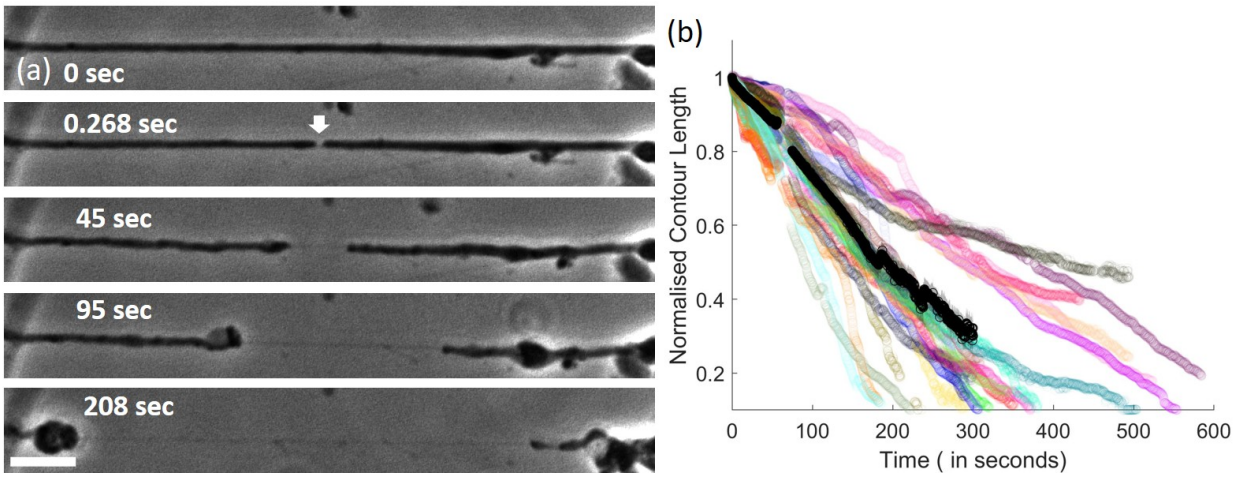

FIGURE 4.5: **Axonal response to partial laser ablation in calcium-rich media. (a)** Sequence of phase contrast images showing the response of an axon to partial laser ablation in calcium-rich media. The white arrow indicates the point of ablation and the ablation was performed at time t = 0 s. Post ablation, the axon exhibits two retraction fronts–one propagating towards the soma and the other towards the growth-cone. A thin membrane tube spans the region between these two fronts. The scale bar is 10 μm. **(b)** Plots showing the time evolution of the normalised contour lengths of the retracting segments (length of each retracting segment divided by its initial length). Data for individual segments are shown in faded colors and the average of all segments is shown using black circles. Note that the average gets skewed beyond t $\approx$ 200 s as faster retraction events end early. The gap in the data at around t = 56 s is due to the switching of the recording speed from 15 fps to 6 fps.

retracted continuously until all axonal material was absorbed into either the soma or the growth cone. This behaviour is quantified by analysing the normalised length of each segment over time, as shown in Fig. 4.5. All axons (n = 23 axonal segments) showed retraction under control conditions. Although a control set of experiments was performed earlier (mentioned in chapter 3), we repeated them under identical conditions for comparison with the calcium-free ablation experiments.

A very different morphological response is observed when axons are partially ablated in a medium free of extracellular Ca^{++}. Specifically,

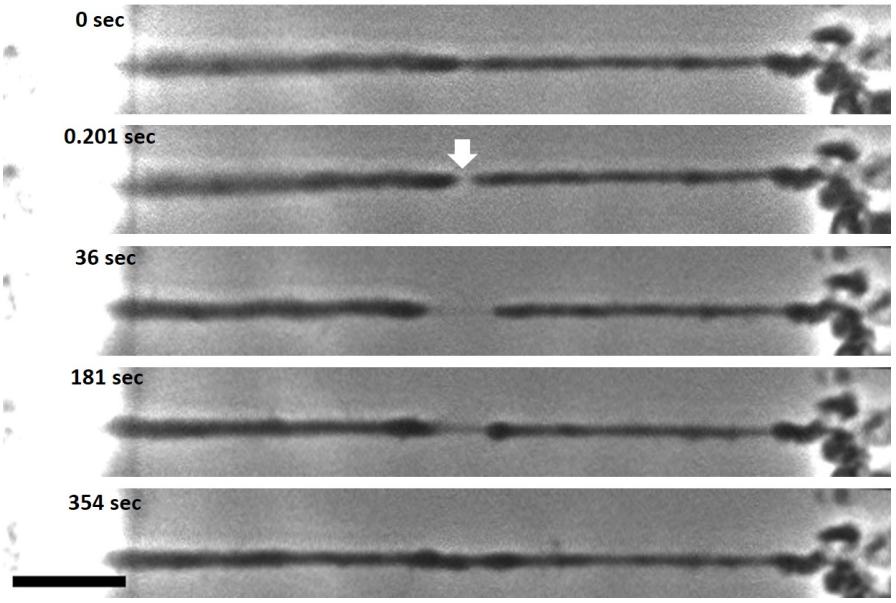

FIGURE 4.6: **Recovery of damage seen in Ca^{++} chelated medium. (a)** A sequence of phase contrast images showing the development of a damaged region and subsequent axonal resealing. The white arrow indicates the point of ablation. It can be seen that the initial retraction and the later recovery occur more or less symmetrically from both sides of the ablation point. The scale bar is 10 μm.

when extracellular Ca^{++} is chelated using EGTA (5 mM), the extent of axonal retraction is significantly reduced compared to control conditions. More remarkably, a subset of axons (10/20 axons) recovered their diameter subsequent to an initial thinning down of their mid-section (see Fig. 4.6). To quantitatively assess these changes, we calculated the contour length of each segment over time. The corresponding data for both proximal and distal segments are presented in Fig 4.7, showing the initial retraction phase and the later recovery phase. Notably, this initial retraction and subsequent morphological recovery occurred from both the proximal and distal segments of the axon (4/10 axons) relative to the ablation site. In contrast, a subset

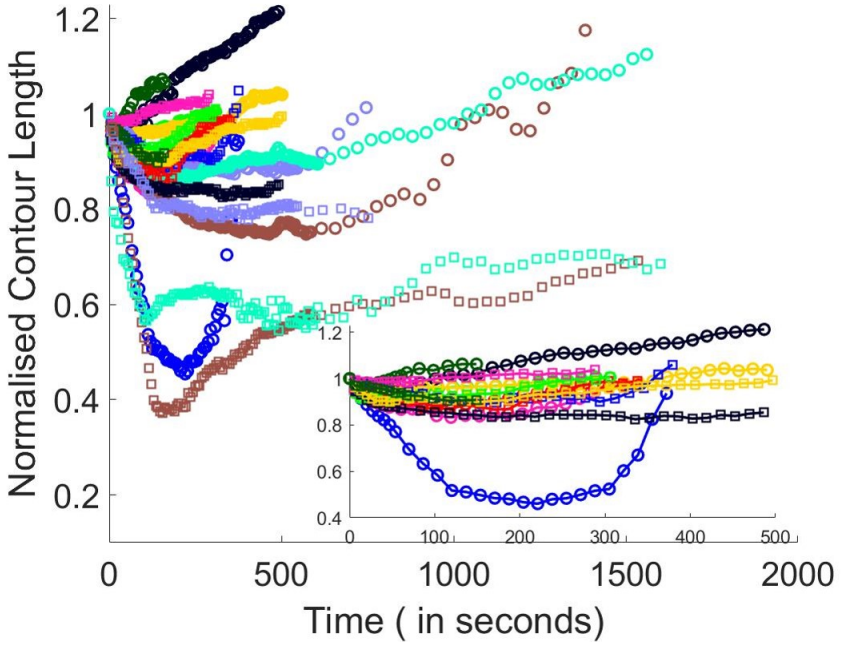

FIGURE 4.7: **Quantification of damage recovery in Ca^{++} chelated medium.** The normalised contour length versus time plot for the axonal segments shows the retraction and recovery for individual segments. The cell body side is shown using circles and the growth-cone side using squares. Segments from the same neuron are shown using the same colour. The inset shows the data for those axons that reseal within 500 sec and is a subset of the main plot.

of axons exhibited partial retraction without any detectable recovery during the imaging period, which lasted up to 600 seconds post-ablation. Representative images and population data are shown in Fig 4.8 and 4.9, respectively. Furthermore, we compared the average retraction curve of axons under EGTA-treated versus control conditions. The results show that axons in calcium-free medium retracted more slowly than their counterparts in normal medium as displayed in Fig. 4.5. For quantification, we fitted the axonal retraction behaviour in both control and EGTA-treated conditions. The initial 10 seconds of each retraction curve were fitted using a combination of exponential and linear functions of the form $y(t) = Ae^{-t/\tau} + Bt + C$, allowing estimation of the relaxation time scale and initial velocity

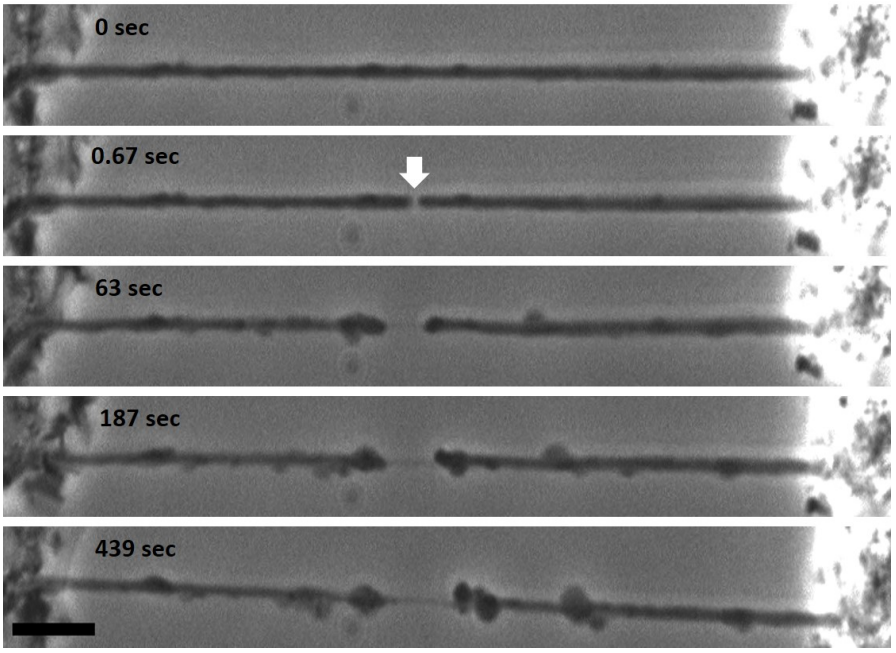

FIGURE 4.8: **Partial retraction (No recovery) of ablated axons in Ca^{++} chelated medium.** Phase contrast images of an axon which was partially ablated in Ca^{++} chelated medium. In this case, the axon has retracted only partially even after about 400 sec.

(shown in Fig. 4.10). The fitted time scales were 0.64 s and 0.68 sec, and the corresponding velocities were 0.0025 and 0.0030 μm/s for the control and EGTA-treated cases, respectively (Fig. 4.10a,c). For the later time regime, a linear fit of the form $y(t) = mt + c$ was applied. Which provided a better estimation of retraction velocities, yielding values of 0.0027 μm/s and 0.0013 μm/s for control and EGTA-treated axons, respectively (Fig. 4.10b,d). The reduction in retraction rate upon EGTA treatment emphasises the critical role of extracellular calcium influx in mediating the morphological responses of axons to partial ablation.

To examine the dynamics of axonal retraction and recovery following

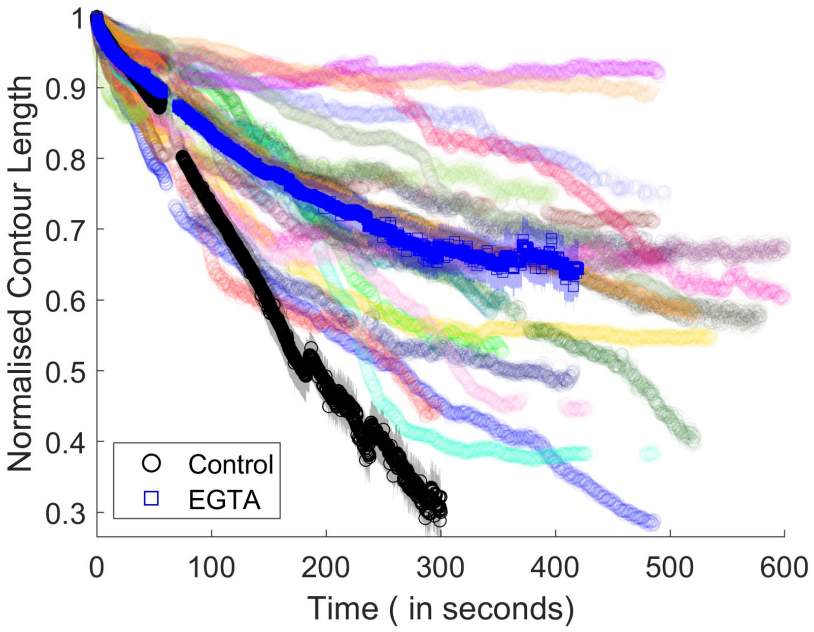

FIGURE 4.9: **Quantification of partial retraction of ablated axons in Ca^{++} chelated medium.** Normalised contour length for axons ablated in medium containing 5 mM EGTA. As can be seen from the data, these axons retract only partially, and the extent of retraction is significantly less than that observed in control axons. The blue squares show the averaged data and the black circles are the averaged data obtained for control axons. The gap in the data at around t = 57 sec is due to the switching of the recording speed from 15 fps to 6 fps.

partial ablation, we generated kymographs from phase contrast time-lapse images. These kymographs show that, in calcium-depleted conditions, recovery most frequently initiates from the cell body side of the axon (Fig. 4.11 and 4.12). Retraction typically begins shortly after ablation and is followed by a regrowth toward the site of injury. Interestingly, while the cell body side predominantly drives the resealing response, a few axons also exhibit some recovery initiated from the growth cone side, shown in Fig. 4.12.

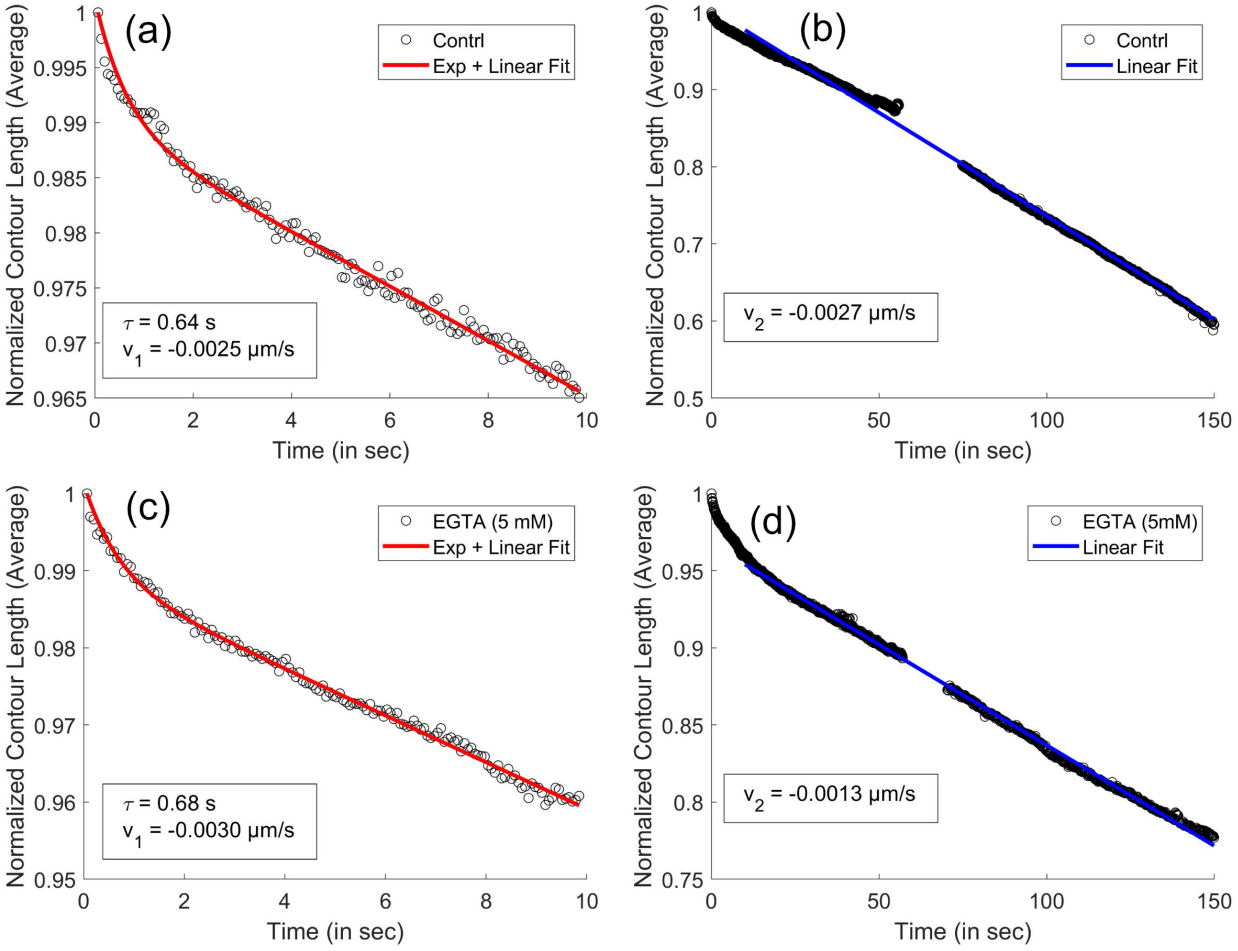

FIGURE 4.10: **Fitting of axonal retraction data in Ca^{++}-rich and Ca^{++}-free media.** In Ca^{++}-rich medium (control), **(a)** a combined exponential and linear fit was applied up to 10 seconds, followed by **(b)** a linear fit for the subsequent time points. Similarly, in Ca^{++}-free medium, **(c)** the initial 10 seconds were fitted with a combined exponential and linear model, and **(d)** the later phase was fitted using a linear fit. The values for the relaxation time constant and retraction velocities are mentioned in the figure.

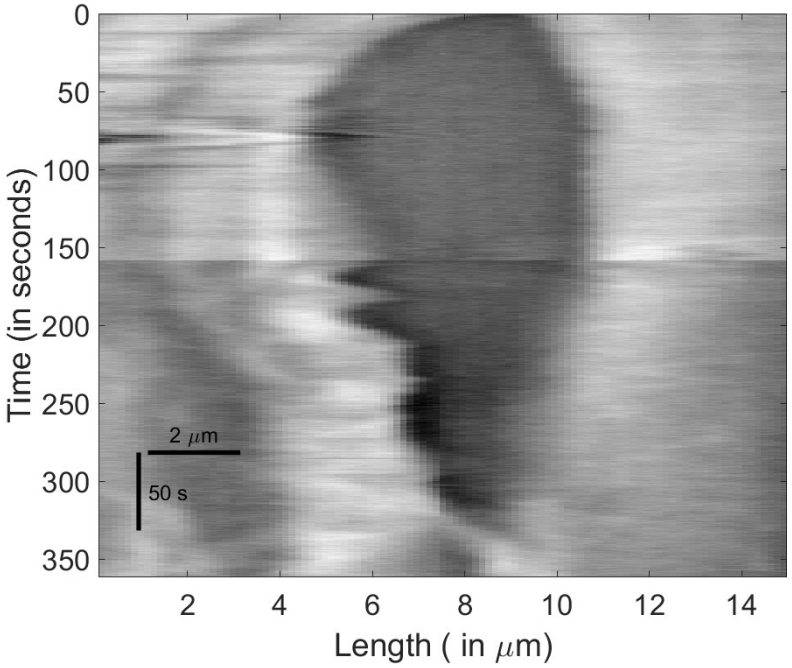

FIGURE 4.11: Kymograph of phase contrast images of partially ablated axon in Ca^{++}-chelated medium shows recovery initiating from the cell body side, which is positioned on the left side. Retraction and subsequent advancement during the recovery process can be observed on the left side. Although the right side corresponds to the growth cone, there appears to be some diffusive activity there as well. The horizontal line around 150 seconds results from a change in imaging frame rate, from 15 fps to 6 fps.

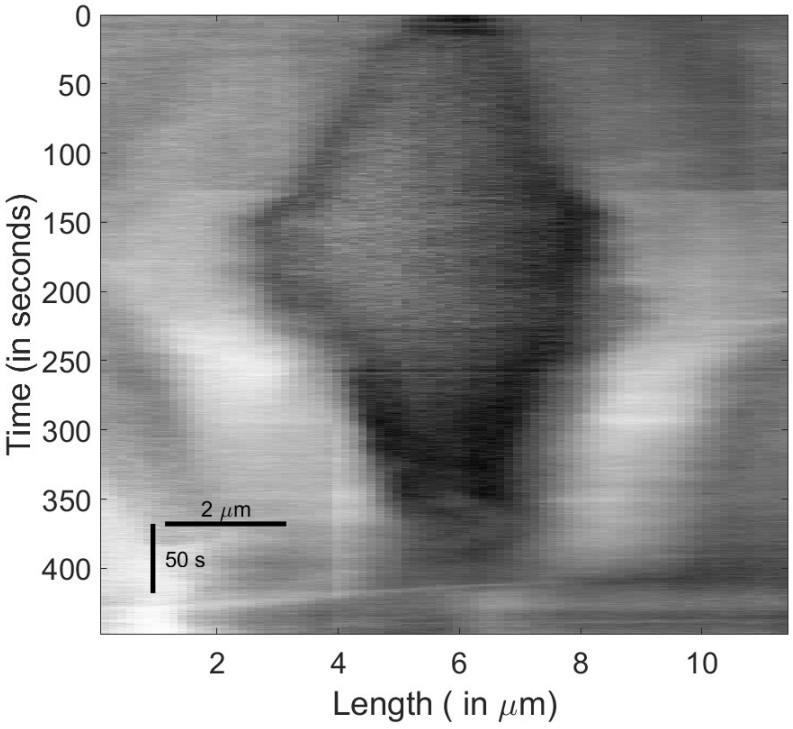

FIGURE 4.12: Kymograph of phase contrast images of partially ablated axons in Ca^{++}-chelated medium show recovery initiating from both the cell body and growth cone sides (with the cell body on the left and the growth cone on the right). Retraction followed by subsequent advancement during the recovery process can be observed on both sides.

4.3.3 Axonal microtubules regrow and reseal after ablation in Ca^{++}-free medium

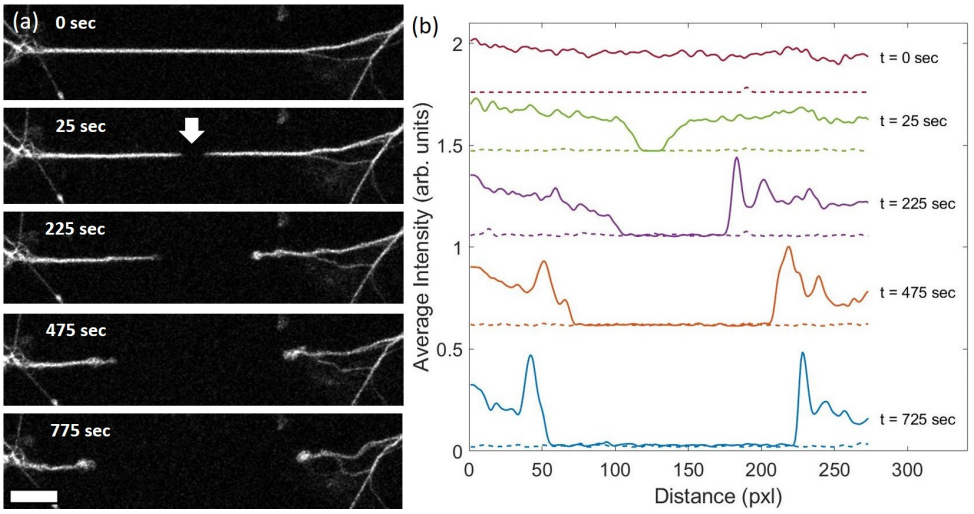

FIGURE 4.13: **Microtubule dynamics in partially ablated axons in Ca^{++}-rich medium . (a)** Sequence of fluorescence images of an axon labeled with the membrane permeable SPY tubulin 555 dye and partially ablated at the point shown by the white arrow. The dye labels only microtubules and not tubulin dimers. Microtubule intensity retracts along with the retraction front seen in phase contrast images. No detectable intensity could be seen in the thinned down mid section of the axon. **(b)** Plots of the microtubule fluorescence intensity corresponding to the images shown in (a). The dotted line shows the zero intensity baseline for each image. Slight accumulation of microtubules can be seen at the retraction fronts. The scale bar is 20 μm. Here, the raw intensity data were smoothed with a Gaussian filter ($\sigma = 1.4$) in MATLAB and then integrated along the axonal thickness before constructing the intensity plots.

The resealing behavior observed in calcium-chelated medium raises important questions about how the axonal cytoskeleton responds under such conditions. Given the structural importance of microtubules, which are highly abundant in axons, we examined their contribution in retraction and resealing processes following partial ablation. To visualize polymerized microtubules, we used the live-cell dye SPY555-tubulin, which specifically labels polymerized tubulin. In control neurons maintained in calcium-containing medium,

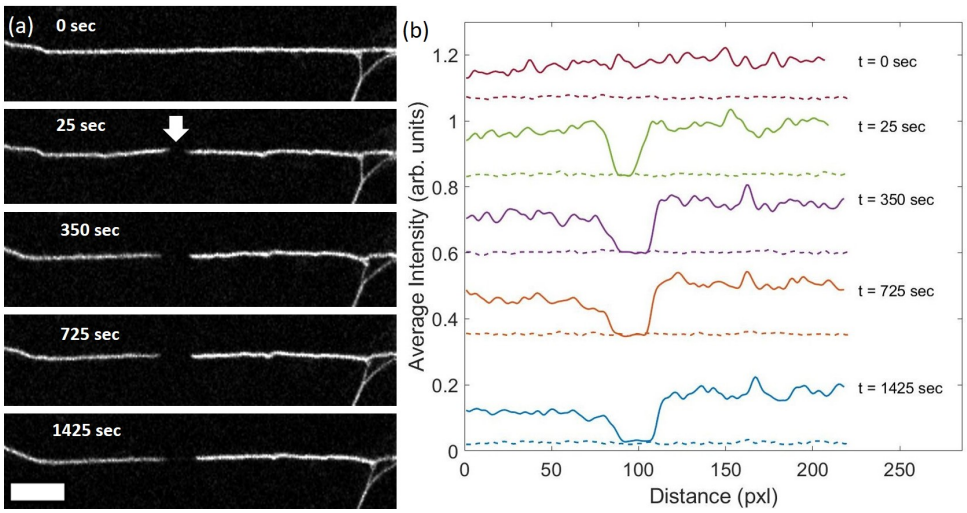

FIGURE 4.14: **(a)** Fluorescence images showing the microtubule retraction in an ablated axon where calcium in the medium was chelated using 5 mM EGTA. In this case, microtubules retract only partially and then remain static for about 25 min (observation time). **(b)** Plots showing the time evolution of the intensity reduction in the thinned-out regions for the axon shown in (a). The dotted line represents the baseline of zero intensity for each image. The scale bar is 20 μm. In this analysis, the raw intensity data were first smoothed using a Gaussian filter ($\sigma = 1.4$) in MATLAB, and subsequently integrated across the axonal width to generate the intensity profiles.

partial ablation led to a clear recession of microtubule intensity from the ablation site in both directions, all the way to the two extremities of partially ablated axons (Fig. 4.13a). This decline in fluorescence closely mirrored retraction observed in phase contrast images. No detectable fluorescence intensity is seen in the thinned down region suggesting complete depolymerization of microtubules (Fig. 4.13b), while this region expands with time. A slight increase in intensity is observed at the boundaries of the retracting segments. This increase may be due to the accumulation of small microtubule fragments at the retracting front.

In contrast, we explored how microtubules behave when extracellular Ca^{++} is chelated. The neurons grown in EGTA (5 mM)-containing

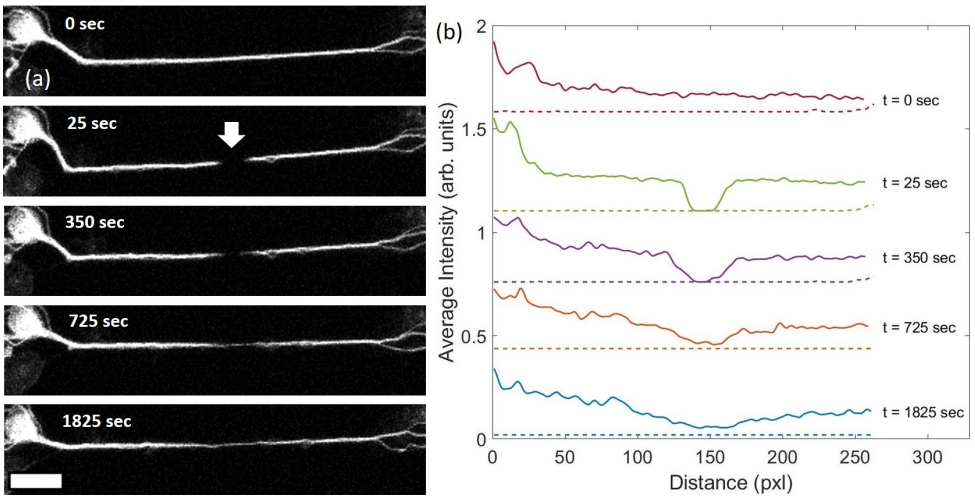

FIGURE 4.15: **(a)** The fluorescent Image sequence for an axon that exhibited only partial recovery of microtubules when ablated in Ca chelated medium. The corresponding intensity plots are shown in (b). A dotted line indicates the zero-intensity level in each image. The scale bar is 20 μm. The raw intensity data were processed by applying a Gaussian filter ($\sigma = 1.4$) in MATLAB for smoothing, followed by integration across the thickness of the axon to create the intensity plots.

calcium-free medium showed different and more diverse microtubule responses. We observed three kinds of responses after partial ablation. Some axons showed an initial retraction of microtubule intensity after which the intensity evolution stops and remains stable for the rest of the observation time of about 25 min (see Fig. 4.14a,b). This may suggest that microtubule depolymerisation was halted in Ca^{++} free media. Comparison of phase contrast and fluorescence images shows that the regions devoid of microtubules appear thin while the parts where intensity is unaffected have normal caliber. Remarkably, in some cases, the intensity initially recedes, then stops receding, starts to recover, and eventually recovers either partially (Fig. 4.15a,b) or completely (Fig. 4.16a,b). The extent of microtubule recovery for complete resealing can be seen from the plot shown in Fig. 4.16b. The time evolutions of microtubule intensity

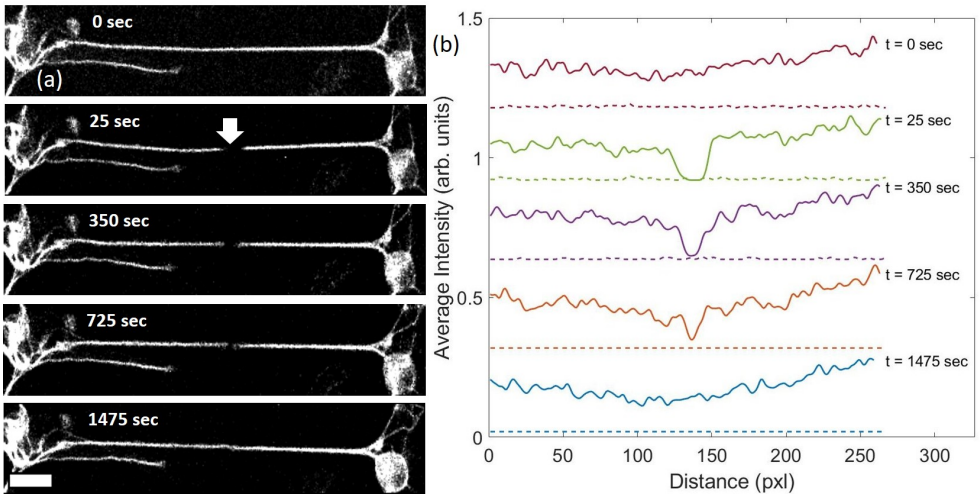

FIGURE 4.16: **(a,b)** Fluorescence images and intensity plots for an axon that showed complete recovery of microtubule intensity subsequent to an initial retraction phase when ablated in Ca chelated medium. Each image includes a dotted line marking the zero intensity reference. The scale bar is 20 μm. Raw intensity data were smoothed using a Gaussian filter ($\sigma = 1.4$) in MATLAB and then integrated over the axonal width to generate intensity plots.

for different axons mirror the observations of diameter measured for the same axons. The absence of microtubule regrowth is associated with a lack of axonal diameter recovery, as depicted in Fig. 4.17. The partial recovery of microtubules is associated with a corresponding partial restoration of axonal diameter shown in Fig. 4.18a. In contrast, a different axon exhibits complete restoration of diameter along with full microtubule recovery after partial ablation, as shown in Fig. 4.18b. This suggests that the microtubule content in axons is directly correlated with axonal diameter.

These findings collectively may indicate that extracellular calcium influx plays a key role in promoting microtubule disassembly and driving retraction. When calcium is removed, these disassembly processes are suppressed, allowing intrinsic cytoskeletal repair mechanisms to dominate, resulting in stabilisation, partial or full recovery

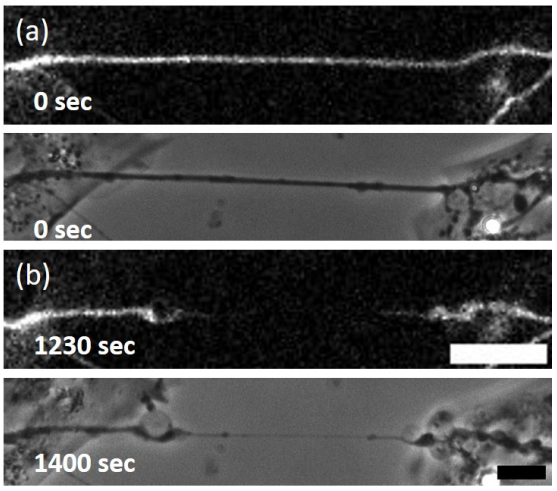

FIGURE 4.17: **Images illustrating the absence of microtubule regrowth and axonal diameter recovery following partial ablation in Ca^{++}-free medium.** Fluorescence and phase-contrast images **(a)** At 0 sec before ablation.**(b)** Corresponding images at 1230 and 1400 sec. Microtubules retract, but no microtubule regrowth and diameter recovery are observed within this time frame. Scale bars: 20 μm for fluorescence images and 10 μm for phase-contrast images.

of microtubules post ablation.

In the previous section, we generated kymographs from phase contrast images to visualise axonal recovery. We also created kymographs showing microtubule recovery. These reveal that recovery predominantly initiates from the cell body side as shown in Fig. 4.19.

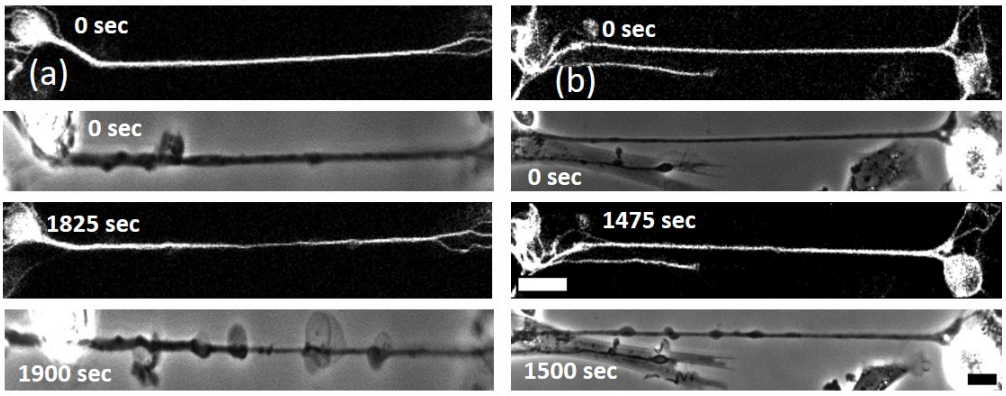

FIGURE 4.18: **Images showing correlation between microtubule recovery and axonal diameter restoration after ablation in Ca^{++}-deficient medium.** All the 0 sec images, including fluorescent and phase contrast, represent the pre-ablation state in (a & b). **(a)** An example of an axon displaying partial recovery of both microtubules and axonal diameter is shown. Imaging continued until 1825 seconds, during which only partial microtubule recovery was observed. The corresponding phase contrast image at 1900 seconds similarly shows partial diameter restoration. **(b)** Recovery of microtubule intensity and axonal diameter is observed at 1475 seconds in the fluorescent image and at 1500 seconds in the corresponding phase contrast image, respectively. The scale bar for the fluorescent image is 20 μm. The scale bar for the phase contrast image is 10 μm.

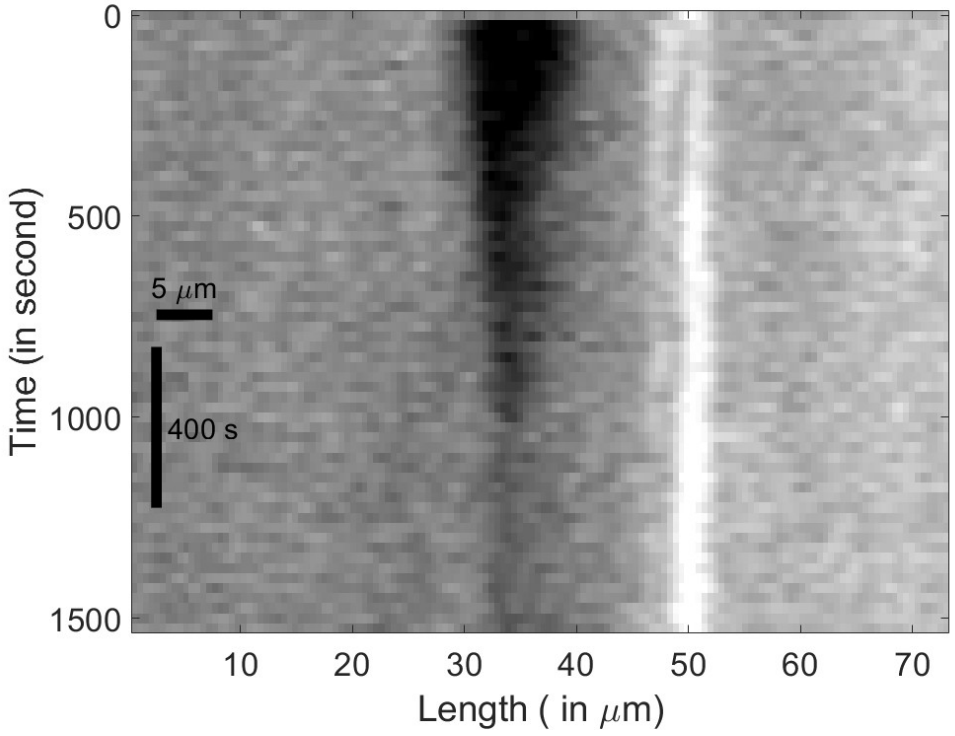

FIGURE 4.19: Kymograph of recovering microtubules in a partially ablated axon in Ca^{++}-chelated medium. Significant recovery is observed from one side, while the other side shows no substantial change.

4.3.4 EB3 dynamics during recovery in Ca^{++} chelated medium

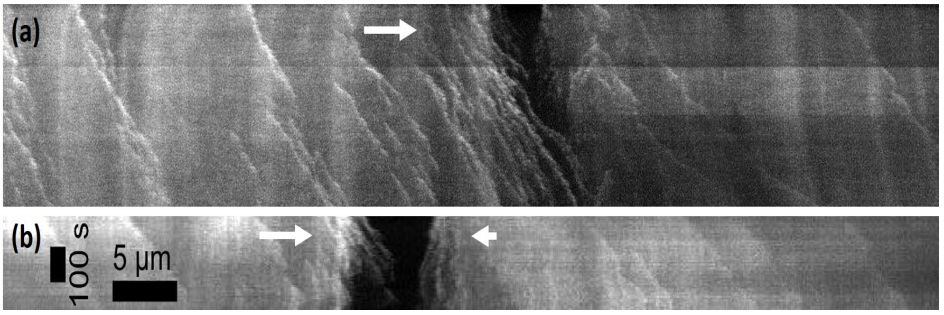

FIGURE 4.20: **Kymographs showing EB3 comet movement to check microtubule polymerisation behaviour.** A clear gap is observed, representing the retraction of axonal segments. **(a)** In this case, most EB3 comets originate from one side (cell body side). The time from retraction to recovery is approximately 905 seconds (∼15 minutes). **(b)** Here, recovery initiates, appearing to originate from both sides of the gap. However, the majority of EB3 comet activity is observed from the left side (cell body), with some comets also emerging from the opposite side. The EB3 comets move toward the retracted region. The total time from retraction to recovery is approximately 265 seconds here. The length of the arrow indicates the extent of recovery from either the cell body or the growth cone side. Length and time scale bars are shown in the figure.

While recovery from both sides was observed in some axons, as evident in the phase-contrast kymographs, microtubule imaging did not show any clear indication of resealing from both ends. To clarify this discrepancy and to further investigate the recovery of microtubules during axonal resealing in the absence of extracellular calcium, we labelled the growing tips of microtubules by transfecting axons with a GFP version of the tip-binding protein EB3. EB3 is a microtubule plus-end tracking protein (+TIPs) that binds transiently to the growing ends of microtubules and allows real-time visualisation of polymerisation dynamics [7]. In chick DRG axons, microtubules exhibit a nearly uniform polarity, with plus ends oriented toward the growth cone. The EB3 comets consistently move from the cell body toward the growth cone [48].

We performed EB3-GFP imaging on axons in calcium-chelated medium following partial laser ablation. EB3 comets were initially absent from the ablated region, which also indicates local disruption of microtubules. However, comets reappeared within the previously damaged zone over time, suggesting that microtubule polymerisation resumed even in the absence of extracellular calcium. Kymographs constructed from EB3 time-lapse sequences show distinct behaviours following ablation exhibited in Fig. 4.20a,b. Kymographs constructed from these EB3 sequences showed that, in most recovering axons, comets resumed movement into the damaged region predominantly from the cell body side, as depicted in Fig. 4.20a. Interestingly, in a few cases, comets were also seen emerging from the growth cone side and entering the ablated region shown in Fig. 4.20b.

4.3.5 Actin filaments too recover in calcium-chelated medium

Unlike microtubules, axonal actin filaments are organised in a more complex manner. In mature axons, including those from chick dorsal root ganglion (DRG) neurons cultured for four days as used in this study, actin fully develops a membrane-associated periodic skeleton, comprising regularly spaced actin rings linked by spectrin (also shown in the figure 1.4) [19, 31]. The other highly heterogeneous cortical actin structures such as actin hot spots and patches [20] are also formed in mature axons. Though less abundant compared to microtubules, these actin-based architectures significantly contribute to axonal mechanics and retraction responses [31, 33, 61, 62, 99].

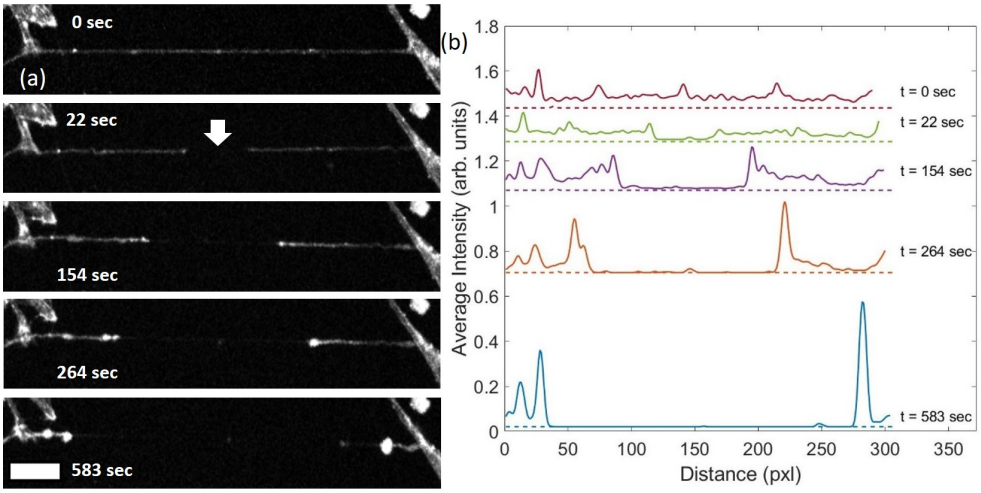

FIGURE 4.21: **Actin retraction post ablation in Ca^{++} rich medium.** **(a)** Sequence of fluorescence images of a control axon which was labeled using SPY650-FastAct dye that labels only polymerised actin and was partially ablated. The white arrow indicates the point of ablation. Post-ablation, a thin tube spans the region between the retracting edges (not visible in the fluorescence images). Actin filaments tend to accumulate at the retracting edges of each axonal segment. **(b)** Intensity plots showing the time evolution of actin fluorescence. Hardly any actin intensity is seen in the thinned out regions. The dotted lines represent the zero intensity level. The scale bar is 10 μm. To obtain intensity plots, the raw intensity data has been smoothened with a Gaussian filter ($\sigma = 1.4$) using Matlab. The intensity is then integrated across the axonal thickness.

To study the damage and possible recovery of actin filaments, we imaged actin using the cell permeable SPY650-FastAct dye which labels only polymerised actin. In control experiments, where Ca^{++} is present in the medium, partial axonal ablation leads to a complete disappearance of actin fluorescence in the ablated and retracted region, similar to what is observed for microtubules (Fig. 4.21a). Very prominent peaks of actin intensity are consistently detected at the ends of the retracting segments, suggesting that actin filaments accumulate at the retracting fronts (Fig. 4.21b). No actin filaments could be detected in the thinned central region. Furthermore, neither the actin intensity nor the axonal diameter showed any signs

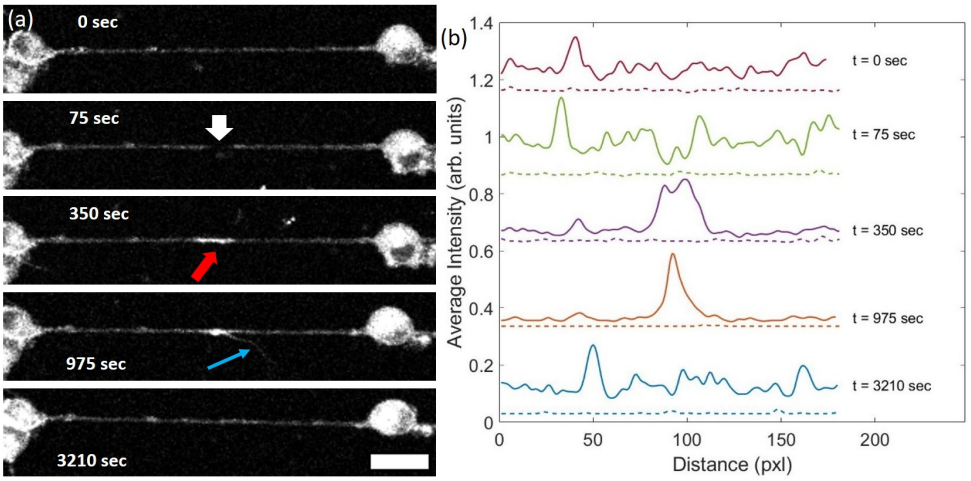

FIGURE 4.22: **Recovery of actin filaments post ablation in Ca^{++} chelated medium.** **(a)** Image sequence of an axon, when partial ablation is performed in calcium chelated medium. Actin intensity in the thin region initially decreases (t = 75 s), then recovers, often overshoots (t = 350 s), and finally redistributes (t = 3210 s). The blue arrow indicates filopodia-like structures that form at regions with enhanced actin intensity. The overshoot intensity in the recovery region is indicated by the red arrow. **(b)** Quantification of the actin fluorescence post ablation and during recovery for the images shown in (a). The overshoot is clearly visible at t = 350 & 975 s. The dotted lines indicate the zero-intensity level. To generate the intensity plots, raw intensity data were smoothed using a Gaussian filter (σ = 1.4) in Matlab, followed by integration across the width of the axon. The scale bar is 10 μm.

of recovery within the 30-minute observation time. This may indicate irreversible damage to the actin cytoskeleton in the presence of extracellular calcium.

When extracellular Ca^{++} is depleted using EGTA, a different behaviour is observed. All axons subjected to partial ablation under Ca^{++}-free conditions show an initial retraction of actin intensity, followed by varying degrees of recovery in the previously thinned midsection. This recovery is a consistent feature across all observed axons, unlike microtubules, which only recover in a subset of cases

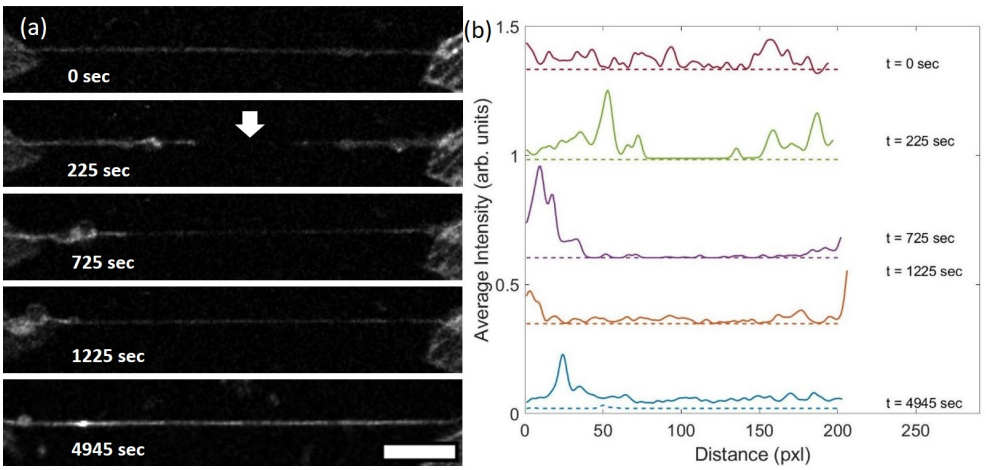

FIGURE 4.23: **Recovery of actin filaments in the membrane tube even after almost complete retraction following ablation in Ca^{++} chelated medium.** **(a,b)** An example of an axon maintained in calcium chelated medium. In this case, retraction is much more extensive making it easier to see how actin filaments recover in the region between the retraction fronts. Unlike microtubules, recovery of actin intensity is seen all along the thinned out segment (t = 725 & 1225 s). A slight overshoot can be seen in this case too (t = 4945 s). The corresponding intensity plots are shown in (b). All intensity plots were generated by smoothing the raw data with a Gaussian filter ($\sigma = 1.4$) in MATLAB, followed by integration across the axonal thickness. The scale bar represents 10 μm.

under the same conditions. Furthermore, in many of these recovering axons, the actin intensity not only returns to baseline but often overshoots, reaching levels higher than the pre-ablation baseline (Figs. 4.22a,b). This excess actin eventually redistributes. This may suggest dynamic remodelling of the cytoskeleton during the recovery phase.

The pattern of actin recovery differs from that of microtubules. While microtubule regrowth often proceeds from the ends of the severed segments and shows a directional pattern, actin recovery tends to be more spatially distributed. No distinct or clearly defined growth fronts are seen in the actin channel. The recovery appears more homogeneous and occurs throughout the retracted region

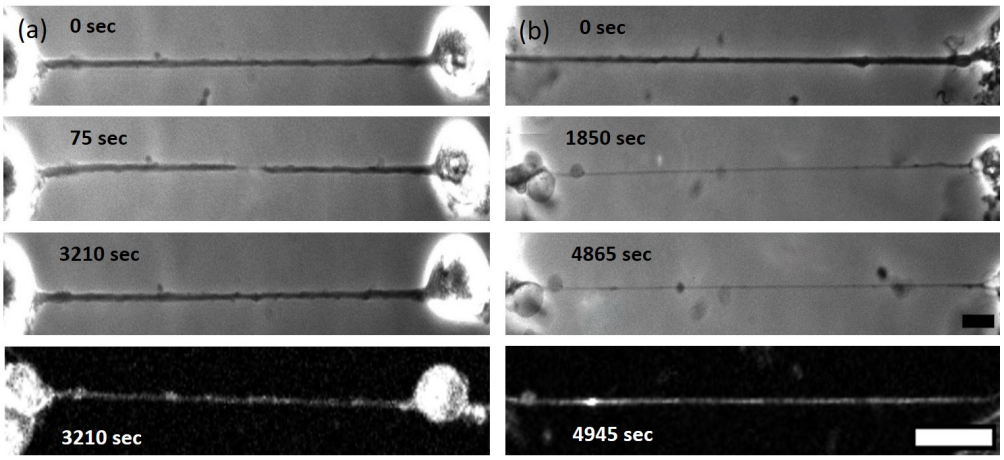

FIGURE 4.24: **Images showing actin and axonal diameter recovery in Ca^{++}-depleted medium.(a,b)** While all axons showed recovery of actin filament intensity, the recovery of actin filaments may or may not be correlated with recover of axonal diameter. In (a), we show the example of an axon which exhibited diameter recovery as well as actin recovery. Whereas, in (b), one can see that there is no recovery in diameter even though actin intensity has recovered all along the axon. The scale bar for the phase contrast image is 10 μm. The scale bar in the fluorescent image represents 20 μm.

(Fig. 4.23a,b).

Another important distinction lies in the relationship between cytoskeletal recovery and morphological restoration. Microtubule recovery often correlates well with the recovery of normal axonal diameter. However, in the case of actin recovery, the axonal diameter does not always return to its initial value. In Fig. 4.24a, we show an example of an axon which has fully recovered its diameter as well as actin filament intensity. However, in Fig. 4.24b, one can see a case where actin intensity has recovered fully, but the diameter failed to recover within the same time span. This indicates that actin alone may not be sufficient to restore axonal diameter, and microtubules are required for complete recovery, as discussed earlier. However, the role of neurofilaments, which may also contribute to axonal diameter restoration, was not explored in this study. These findings highlight

that extracellular calcium may cause the actin filament disassembly during retraction.

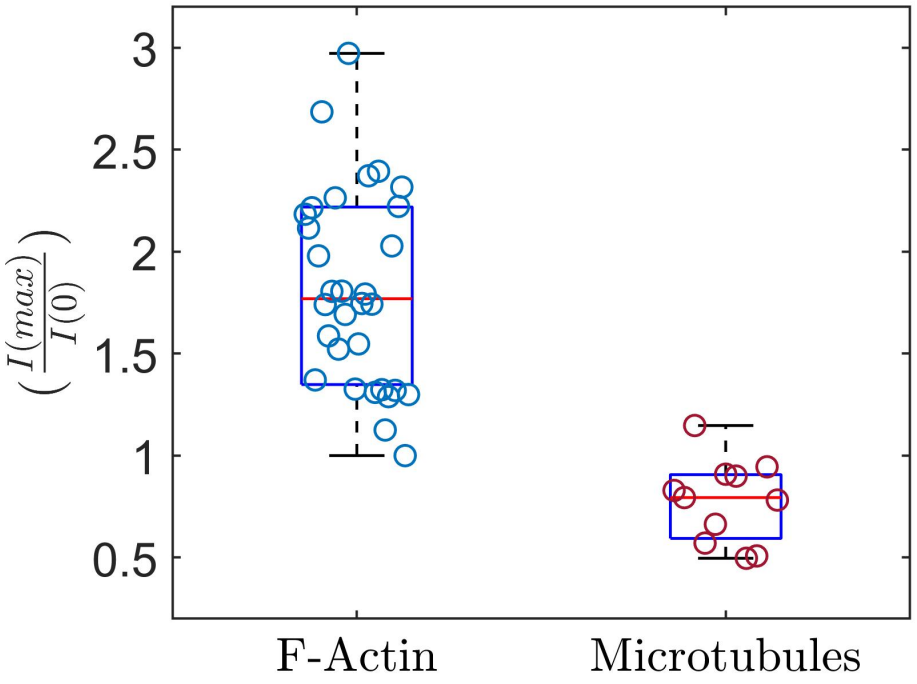

FIGURE 4.25: **Comparison of post-ablation intensity of microtubules and actin filaments.** The data show the ratio of pre-ablation intensity per unit axonal length I(max) to the maximum post-ablation intensity per unit length observed in the initially thinned out region I(0).

As mentioned earlier, one key difference between the recovery behaviour of microtubules and actin filaments following partial axonal ablation lies in the nature of their intensity profiles during recovery. Specifically, actin filaments tend to exhibit an overshoot in fluorescence intensity surpassing their pre-ablation levels. The microtubule recovery typically returns to baseline or remains slightly below it. This difference is quantitatively represented in Fig. 4.25, where the ratio of maximum post-ablation intensity to the pre-ablation intensity is plotted for both cytoskeletal components (filamentous actin and microtubules). The region analysed corresponds to the initially

thinned or damaged portion of the axon that subsequently underwent recovery.

4.4 Discussion and possible explanation

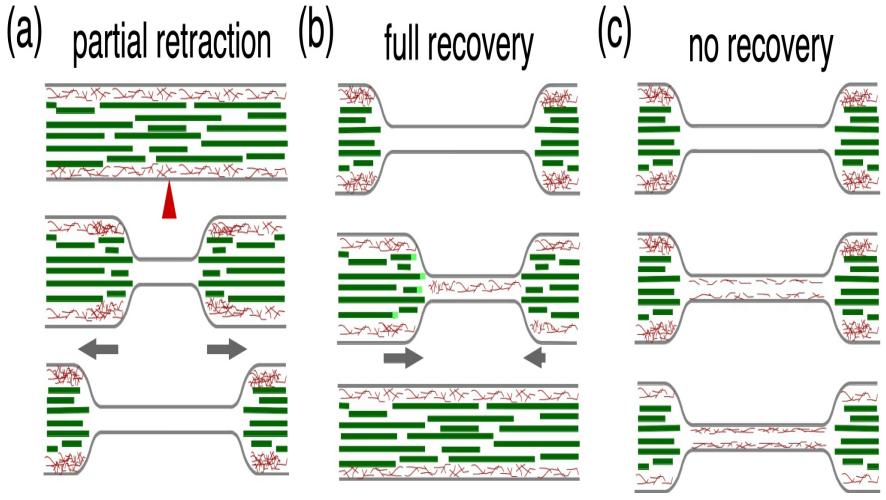

FIGURE 4.26: **Schematic of cytoskeletal retraction and recovery in Ca^{++} free medium.** **(a)** Diagrams showing the receding of microtubules (green) and actin filaments (red) post ablation. The red arrowhead indicates the point of ablation. Actin rings, seen commonly in axons, are not shown. **(b)** Schematic of a case where microtubules and actin filaments recover in calcium chelated medium. Growing, regrowing microtubule tips are marked in light green. **(c)** A case where only actin filaments reform in the thin section. In such cases, there is no recovery of diameter.

In this chapter, we explored the responses of axonal retraction following partial ablation under both calcium-rich and calcium-deficient conditions. We investigated the roles of microtubules and actin in retraction in both environments. In calcium-rich conditions, both cytoskeletal components underwent complete retraction. However, in calcium-deficient conditions, recovery of both microtubules and actin was observed. Additionally, the recovery of axonal diameter

appeared to be associated with microtubule recovery, but not with actin.

Partial ablation typically leads to the formation of a thin, membrane segment at the site of injury. This membrane thinning expands in both directions along the axon, generating two retraction fronts that advance toward the cell body and growth cone ends, respectively. These two retraction fronts can be easily tracked using phase-contrast imaging. Fluorescence imaging obtained using dyes that bind to filaments only shows that microtubules and actin filaments dissociate progressively from the ablation point in both the proximal and distal segments (schematically shown in Fig. 4.26a). This continues till the entire segment becomes atrophied. The dissociation of microtubules occurs as a sharp front, whereas actin filaments show significant accumulation at the retracting edges, as shown in Figs. 4.13a, 4.21a, and schematic 4.26a. Together, these results may validate partial laser ablation as a controlled and insightful approach to dissect axonal injury and cytoskeletal remodelling. This method offers valuable insights into both the damaging processes initiated by calcium influx and the protective responses that emerge in its absence.

The above observations suggest that microtubule depolymerisation occurs at the retracting front–analogous to the shortening of a burning pyrotechnic fuse. This phenomenon is surprising, as it is well established that axonal microtubules contain labile and stable populations, and the stable fraction remains unaffected for long periods

under the treatment with microtubule-disrupting drugs like Nocodazole [99, 164]. Moreover, it is also known that microtubule stability exhibits a radial dependence due to post-translational modifications, with microtubules in the outer part of the bundle being less stable compared to those in the inner core [165]. Consistent with this, treatment with nocodazole causes the axonal microtubule bundle to thin down, leaving behind a stable core along the length of the axon [99]. In our experiments involving partial laser ablation, however, we have not seen any signatures of thinning down of the microtubule bundle. The fluorescence intensity of the microtubule remains uniform behind the retracting front. This is particularly surprising considering the fact that Ca^{++} elevation spreads across the axon much faster than the retraction speed. Moreover, since individual microtubules are short (typically about 10 microns [166]), compared to axon length (100–200 microns), complete retraction of the microtubule bundle in control axons indicates depolymerisation of microtubules that are not directly affected by the laser. Therefore, how the microtubule bundle shortens from one end instead of losing the more dynamic, labile fraction first is to be explored in future research.

Here, we speculate that the observed phenomenon may be driven by collective effects arising from microtubule–microtubule interactions, which are mediated by microtubule-associated proteins (MAPs) such as tau [16, 167]. These MAPs not only stabilise microtubules but also serve to physically link them, promoting structural integrity across the microtubule bundle [17]. When a laser transects microtubules

across an axonal cross-section, the affected microtubules are left with unstabilized ends, leading to rapid depolymerisation (Fig. 4.27). The collapse of these microtubules leads to a reduction in the number of MAP-bound neighbours for microtubules which are away from the ablation point, but were overlapping with the ones damaged by the laser. This leads to the depolymerisation of these microtubules as well. This process may be due to reduced stability arising from loss of MAPs or due to the action of severing enzymes like spastin and katanin, which can now gain easy access to these neighborless microtubules at the end of the bundle. Such mechanisms generate a cascading effect leading to a progressive and catastrophic collapse of the bundle as depicted in Fig. 4.27.

We also observe that laser-induced axonal injury triggers transient elevation of cytosolic calcium levels, which propagates bidirectionally from the damage point. When axons are partially ablated using a laser, Ca^{++} from the extracellular environment may enter through the injury site and via voltage-gated calcium channels [5]. This influx of calcium can trigger the release of additional calcium from internal stores via a process called calcium-induced calcium release [157]. Taken together, these show that both extracellular influx and intracellular release can be important. To more directly assess the role of internal calcium stores, experiments can be performed by depleting the ER Ca^{++} with thapsigargin and by blocking IP3 and ryanodine receptors, alongside appropriate controls.

Elevated Ca^{++} levels may activate the calpain proteases, as well as

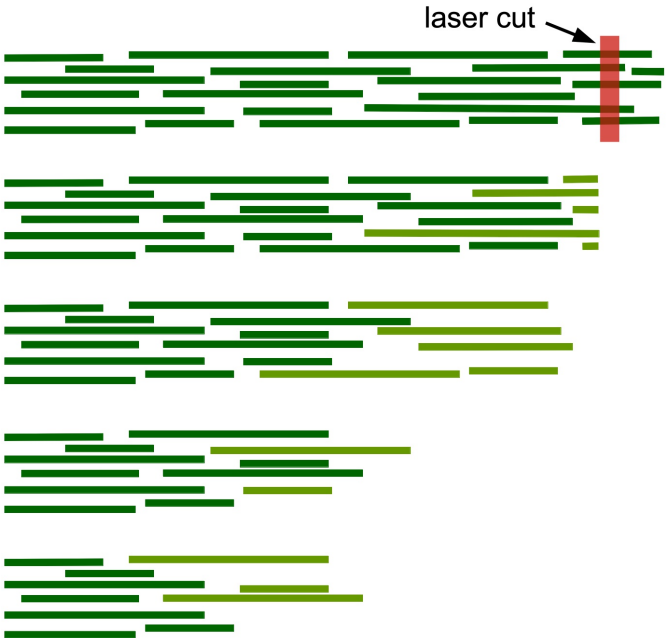

FIGURE 4.27: **Proposed microtubule bundle instability mechanism**. Schematic showing a possible mechanism for the loss of microtubules within the bundle in the form of a retracting front. Microtubules with compromised stability are shown in light green. Microtubule-associated proteins that interlink microtubules are not shown. Microtubules that are directly cut by the laser become unstable and depolymerise. This leads to a reduction in the number of neighbours for adjacent microtubules, making them unstable–either due to MAP unbinding or due to severing enzymes like spastin and katanin gaining access to loosely packed tubules. This causes a cascade effect leading to a depolymerising front.

the actomyosin contraction (AMC) [101]. The activation of proteases can result in the breakdown of cytoskeletal components (microtubules and neurofilaments), reducing the opposing elements of retraction [153, 158]. The subsequent reduction in opposing elements, combined with the activation of the AMC, may lead to the retraction of axonal segments.

Chelation of extracellular calcium using EGTA or intracellular free calcium using BAPTA-AM suppresses Ca^{++} elevation. Preventing Ca^{++} elevation using EGTA reduces the speed (-0.0027 μm/s for control axons and -0.0013 μm/s for EGTA-treated axons) of axonal

retraction and prevents complete retraction of both the distal and proximal segments. Hence, it is likely that microtubule depolymerisation is driven at least partly by calcium-induced mechanisms like calpain-mediated disassembly [141, 168]. Moreover, if there is no intracellular Ca^{++} influx, then there would not be any activation of calpain and AMC. If AMC is not activated to the extent typically seen in cases with high calcium levels leading to cell retraction, then there will be no significant axonal retraction. Also, there will be no significant degradation of cytoskeletal components caused by calpain due to its inactive state resulting from the absence of intracellular calcium. As a result, opposing forces may counteract AMC, and there will be little to no significant or slow retraction following ablation.

Remarkably, a fraction of axons show recovery of normal calibre. Imaging of microtubules shows that in such axons microtubules also recover completely (see Fig. 4.16a,b and the schematic 4.26(b)). When axotomy is performed in calcium media, the calpain-mediated cleavage of microtubule-associated proteins (MAPs) may destabilise the microtubules. Therefore, ablation in Ca^{++} free media may not significantly impact microtubule stabilisation. Moreover, neuronal microtubules are believed to be more stable compared to those found in dividing cells [23]. Therefore, this microtubule stabilisation may promote the regeneration of microtubules, as reported in a study following spinal cord injury [169]. The tubulin pool available near the site of transection may assist in the polymerisation process.

Time-lapse imaging using EB3 comets shows that microtubule regrowth predominantly initiates from the proximal segment, with far fewer comets observed emerging from the distal end. The maintenance of microtubule polarity during this regrowth indicates that microtubule recovery is most likely via regrowth of existing filaments and not through *de novo* nucleation of new tubules.

Actin filaments also recover after the initial disruption when extracellular calcium is chelated. Unlike the case of microtubules, actin filament reformation occurs along the entire length of the thinned axonal regions and, in several instances, even exceeds their original levels (see Fig. 4.23a,b). However, this recovery alone is not sufficient to restore axonal calibre. In contrast to microtubules, the restoration of actin filaments does not necessarily lead to structural recovery of the axon, as evidenced in Fig. 4.24b and the schematic in Fig. 4.26c.This recovery is reminiscent of the recovery of actin filaments in cellular blebs, where fresh nucleation of filaments occurs from a free membrane soon after expansion of a bleb, mediated by membrane-bound actin nucleator proteins [170]. A similar mechanism may be at play here, with actin filaments nucleating directly from the exposed axonal membrane in the absence of microtubule scaffolding. A comparison of phase-contrast images and microtubule fluorescence further reveals that axonal calibre is closely correlated with microtubule content, rather than with actin filament density as depicted in Fig. 4.26b,c. Specifically, we observe a sharp transition

in axonal diameter that aligns with the front of microtubule depolymerisation. These findings support the conclusion that microtubule recovery, but not actin, plays the dominant role in restoring axonal structure. Thus, microtubule recovery is a key determinant of axonal recovery following injury.

Chapter 5

Conclusion

5.1 Summary of axonal retraction and resealing responses

In summary, the thesis presents the construction and characterisation of a cost-effective laser ablation setup for performing laser ablation on axons. The aim of this project was to understand how the different cytoskeletal components react when the axonal continuity is perturbed. In particular, we wanted to delineate passive viscoelastic responses, active contractile responses, and cytoskeleton depolymerisation responses in such axons.

In the previous two chapters, we have presented results on retraction

dynamics exhibited by axons under various injury-mimicking conditions. These were complete ablation, partial ablation and trypsin-mediated growth-cone deadhesion. These experiments were also conducted using axons treated with cytoskeletal stabilisers or destabilisers and a myosin-II inhibitor.

These results show that axons are under pretension, which is released via a short-time viscoelastic-like strain relaxation immediately after complete ablation. We show that active contractility too contributes to the retraction, especially at longer times, as the relaxation after applying myosin-II blocker or actin filament disruption is slower. Stabilising drugs have a dramatic effect on the response—axons exhibit a highly diminished viscoelastic-like region and show a very slow retraction with a constant velocity, with Taxol showing a greater stabilisation. This suggests some slow depolymerisation process, possibly dominated by microtubules.

The viscoelastic-like short-time response is also diminished in partially ablated axons. This could be because of high friction between the retracting cytoskeletal composite and the membrane. Besides this, when compared to complete transection, we observe very different responses for axons treated with actin filament stabiliser or for axons treated with a microtubule-disrupting agent. These experiments were verified with two different batches of drugs to rule out issues with drug efficacy (the drugs were also tested on fibroblasts for known effects). Whether these differences can be accounted for by

considering frictional effects or contractility of the two cytoskeletal systems is not yet clear.

Imaging of free calcium ions within the axon post-ablation revealed a sudden elevation in its concentration. Further studies conducted using chelators show that calcium elevation is triggered by the entry of extracellular calcium and the release from stores. Such studies also show that calcium aids in the degradation of actin filaments and microtubules, and in the case of partial ablation, chelating calcium can lead to recovery of these skeletons. More remarkably, we see that actin filaments always recover, whereas microtubule recovery occurs in only a subset of axons. We also see that microtubule recovery leads to a complete recovery of the axonal diameter. To our knowledge, this healing of axons has not been demonstrated before, and provides important clues towards alleviating crush injuries to nerves where damage may be limited to the cytoskeleton without affecting membrane topology.

A comparison of the retraction process for control axons perturbed in three different ways is shown in figure 5.1. When axons are destabilised by detaching their growth cones with trypsin, the resulting retraction is much slower than that seen after full ablation. Even though we did not perform calcium experiments in this case, we speculate that the main cause for this diminished rate could be that no calcium wave is triggered in this case. However, the retraction speed of partially ablated axons, where calcium elevation is observed, is

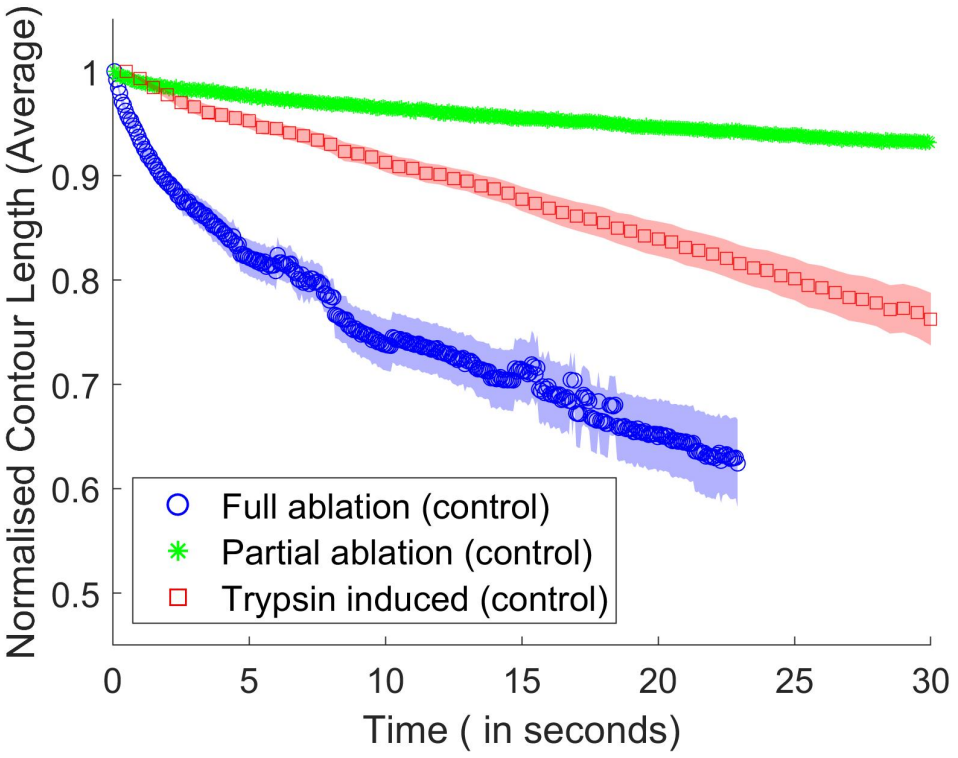

FIGURE 5.1: Comparison of full ablation, partial ablation, and trypsin-induced axonal retraction in control conditions.

even slower than the trypsin deadhesion case (Figure 5.1). Although calcium elevation occurs following partial ablation, the extent of retraction may be restricted by high cytoskeleton-membrane friction.

The different retraction responses seen in the above-mentioned studies, including the recovery dynamics, provide several clues on the mechanisms of axonal retraction after injury. Many more studies are required to clearly understand the contributions coming from the different mechanisms mentioned above and to separate out contributions from actin and tubulin structures. Some of these are discussed below.

5.2 Future directions

During axonal retraction, it remains unclear whether strain relaxes uniformly along the axon and how individual cytoskeletal components, such as actin and microtubules, respond under these conditions. Fluorescent dyes that label cytoskeletal elements, combined with photobleaching experiments, can be used to assess these dynamics along the axonal length (shown in Fig 5.2).

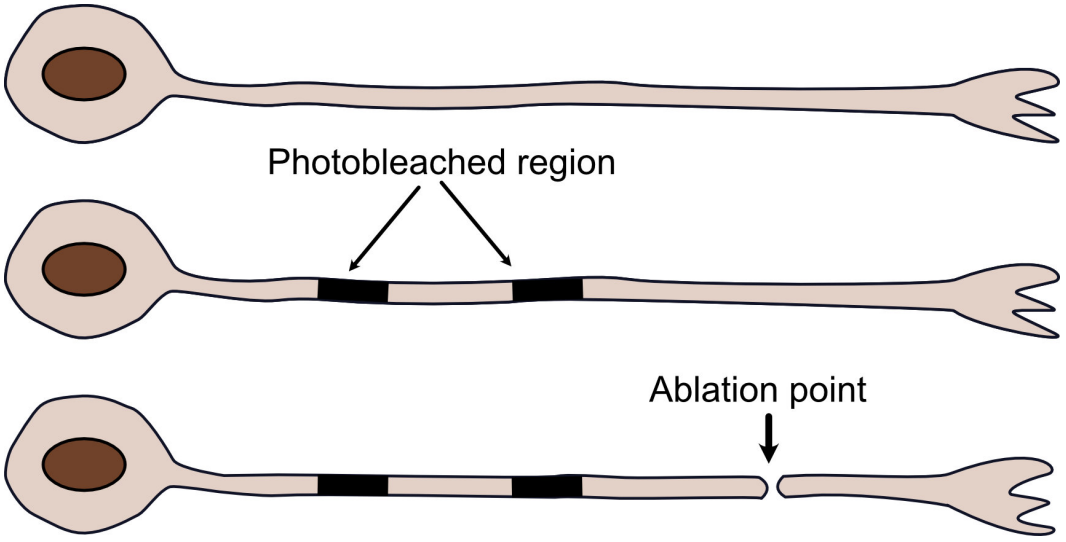

FIGURE 5.2: The pre- and post-ablation axonal images are shown here. The axon with the photobleached patch after photobleaching is also displayed.

Given the presence of the membrane periodic skeleton (MPS) in axons, partial ablation followed by chemical fixation could provide insights into how MPS behaves during retraction. Axons that are attached to the surface can be ablated, as performing super-resolution microscopy on floating axons is challenging due to the limited working distance. By doing this, we can gain insight into how these rings evolve during retraction.

Axons often exhibit twisting after ablation, which may indicate the presence of stored torsional stress. Investigating the helicity of these twisted segments could offer valuable information about the underlying structural organisation. The number of rotations and the specific contributions of different cytoskeletal components to this torsional behaviour could be studied using fluorescently labelled markers and cytoskeletal drugs.

The role of neurofilaments in the resealing phase remains poorly understood. While BAPTA treatment suppresses calcium elevation, it is unclear whether it has the same impact on axonal retraction as EGTA. We hypothesise that microtubule-severing proteins—such as spastin and katanin—as well as calcium-activated proteases contribute to retraction. This could be tested using calpain inhibitors. Furthermore, combining protease inhibitors with microtubule-targeting agents may offer a more comprehensive understanding of the mechanisms driving axonal retraction.

Interestingly, actin recovery has been observed even in calcium-deficient conditions, where axonal calibre does not fully recover. This may serve as a useful model system to investigate actin ring formation within the axonal tube.

Appendix A

Materials and Methods

A.1 Cell culture medium

L-15 medium (21083–027, Thermo Fisher Scientific) was made viscous using autoclaved methylcellulose (H7509-100 g; Sigma-Aldrich, Darmstadt, Germany) at a ratio of 100 ml to 0.6 g by stirring overnight at 4 °C. This was then supplemented with 10% (v/v) heat-inactivated fetal bovine serum (10100; Gibco), 2% (v/v) 33.3 mM glucose (G6152; Sigma-Aldrich, St. Louis, MO), 20 ng per ml Nerve Growth Factor (13290-010; Invitrogen, Carlsbad, CA) and 10 µl/ml Penicillin-streptomycin-glutamine (10378-016, Gibco).

A.2 Neuronal cell culture

Fertilised Giriraja-2 chicken eggs were acquired from the Karnataka Veterinary, Animal and Fisheries Sciences University, Bangalore, India. Eggs were incubated at 37 °C for 8-9 days and dissected in HBSS

buffer (14025-092, Gibco) under a stereomicroscope to isolate Dorsal Root Ganglia (DRGs). After extraction, DRGs were rinsed in the HBSS buffer lacking Ca^{++} or Mg^{++} (14025-092, Gibco) (14175-095, Gibco), incubated at 37 °C with 0.5% Trypsin-EDTA (15400-054, Gibco) for 10 min, and then dissociated by gentle pipetting. The cells were seeded on a clean, uncoated glass coverslips. Cells were incubated at 37 °C for 96 hr to allow for growth. It is known that by this stage the membrane associated periodic skeleton is fully developed [31]. Before performing ablation experiments, neurons were incubated for 30 min in L-15 medium lacking methylcellulose but containing all the other supplements mentioned above. The data were obtained from experiments conducted on multiple embryos to ensure reproducibility and account for biological variability.

A.3 Calcium imaging and chelation

To detect any elevation of calcium levels, cells were preloaded with Fluo-4 AM (F14217, Invitrogen) at 0.5 µM concentration and 20 min of incubation. Chelation of extracellular or intracellular calcium was done using EGTA (03777-10G, Sigma-Aldrich) at 5 mM or BAPTA AM (B6769, Invitrogen) at 10 µM, respectively. The EGTA stock solution was prepared in Millipore deionised water at a concentration of 100 mM. The working concentration of 5 mM was prepared in L15 medium lacking methylcellulose. The pH of the working solution was adjusted to within 7.2–7.3 by adding either NaOH or HCl and

measured using a pH meter. BAPTA was prepared using DMSO as a solvent. The control experiment for Ca^{++} imaging was done using DMSO as a vehicle. Images were acquired using a Leica TCS SP8 confocal system, keeping all the imaging parameters exactly the same before and after ablation.

A.4 Visualisation of cytoskeletal dynamics

SPY555-Tubulin dye (SC203, Spirochrome, Switzerland) and SPY650-FastAct dye (SC505, Spirochrome, Switzerland) were used to stain microtubules and actin filaments, respectively. These dyes are specific to these biopolymers and do not label tubulin or actin unless they are in polymerised form. The neurons were incubated with the dye using L15 media lacking methylcellulose at a concentration of 1:1000 v/v for 30 min to 1 hour before starting the ablation experiments. To visualise microtubule dynamics, cells were transfected with EB3-GFP by electroporation using an electroporator (NEPA21 Type II, NEPA GENE). The electroporation voltage was set to 125 V, and the construct used was EB3-mNeon. Imaging was performed 96 hours post-transfection.

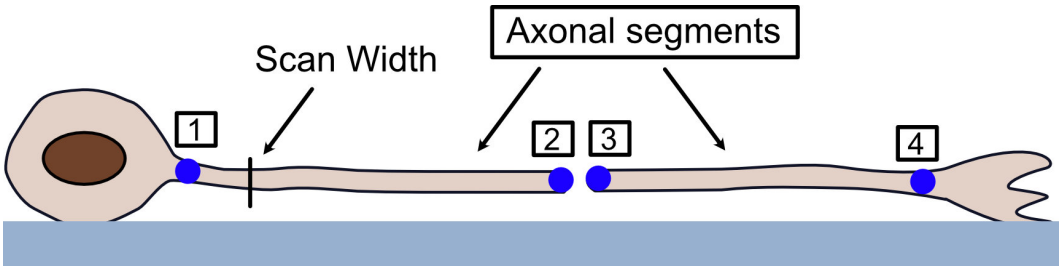

FIGURE A.1: The axonal segments are shown here. The four blue points indicate manually selected positions. The scan width was taken along the axonal diameter from point 1 to 2 and from point 4 to 3 to obtain the y-values after taking the weight average.

A.5 Image and contour length analysis

The contour length analysis was performed using a custom MATLAB program (The MathWorks, Natick, MA) on phase-contrast time-lapse image sequences. For the first frame, which is just after ablation and contains two axonal segments, four points—two for each segment—were manually selected to define the segments (shown in the figure A.1). After preprocessing the images, the local vertical intensity profile was extracted at each x-coordinate between the selected points, and the corresponding y-position was determined using an intensity-weighted average (centre of mass).

$$\bar{y} = \frac{\sum_i w_i y_i}{\sum_i w_i}$$

- $\bar{y}$ is the weighted average of the values y_i,
- y_i represents the individual data values (e.g., pixel positions),
- w_i represents the weights corresponding to each y_i (e.g., image intensity at pixel i),

- The numerator $\sum_i w_i y_i$ calculates the total contribution of all values, scaled by their weights,
- The denominator $\sum_i w_i$ normalizes the result by the sum of all weights, ensuring the average is scaled appropriately.

This process was automated and repeated across all frames. The resulting y-values for both retracting segments were saved as matrices in a text file. After obtaining the y-values, the contour length was calculated by summing the lengths of line segments between consecutive points using the distance formula (discrete Euclidean formula).

$$L = \sum_{i=1}^{n-1} \sqrt{(x_{i+1} - x_i)^2 + (y_{i+1} - y_i)^2}$$

where (x_i, y_i) and (x_{i+1}, y_{i+1}) are coordinates of consecutive points along the axonal segment. The flowchart below illustrates the algorithm sequence.

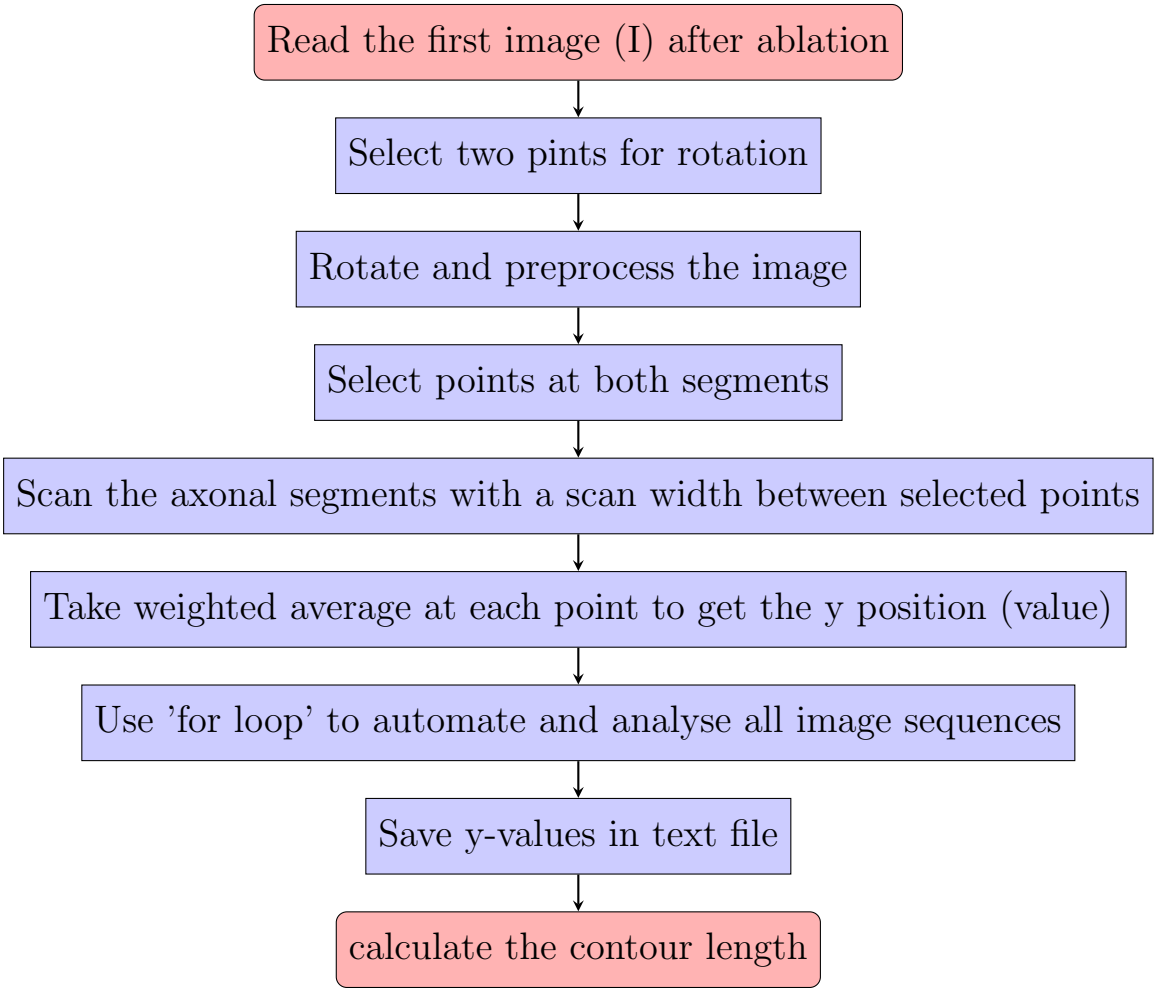
Read the first image (I) after ablation
Select two pints for rotation
Rotate and preprocess the image
Select points at both segments
Scan the axonal segments with a scan width between selected points
Take weighted average at each point to get the y position (value)
Use 'for loop' to automate and analyse all image sequences
Save y-values in text file
calculate the contour length

Bibliography

[1] Alberts B, Bray D, Lewis J, Raff M, Roberts K, Watson JD, et al. Molecular biology of the cell. vol. 3. Garland New York; 1994.

[2] Fletcher DA, Mullins RD. Cell mechanics and the cytoskeleton. Nature. 2010;463(7280):485-92.

[3] Gallo G. Myosin II activity is required for severing-induced axon retraction in vitro. Experimental neurology. 2004;189(1):112-21.

[4] Shao X, You R, Hui TH, Fang C, Gong Z, Yan Z, et al. Tension- and adhesion-regulated retraction of injured axons. Biophysical journal. 2019;117(2):193-202.

[5] George EB, Glass JD, Griffin JW. Axotomy-induced axonal degeneration is mediated by calcium influx through ion-specific channels. Journal of Neuroscience. 1995;15(10):6445-52.

[6] Vargas ME, Yamagishi Y, Tessier-Lavigne M, Sagasti A. Live imaging of calcium dynamics during axon degeneration reveals

two functionally distinct phases of calcium influx. Journal of Neuroscience. 2015;35(45):15026-38.

[7] Stepanova T, Slemmer J, Hoogenraad CC, Lansbergen G, Dortland B, De Zeeuw CI, et al. Visualization of microtubule growth in cultured neurons via the use of EB3-GFP (end-binding protein 3-green fluorescent protein). Journal of Neuroscience. 2003;23(7):2655-64.

[8] Shors TJ, Anderson ML, Curlik Ii D, Nokia MS. Use it or lose it: how neurogenesis keeps the brain fit for learning. Behavioural brain research. 2012;227(2):450-8.

[9] Phillips JB, Smit X, Zoysa ND, Afoke A, Brown RA. Peripheral nerves in the rat exhibit localized heterogeneity of tensile properties during limb movement. The Journal of physiology. 2004;557(3):879-87.

[10] Vitriol EA, Zheng JQ. Growth cone travel in space and time: the cellular ensemble of cytoskeleton, adhesion, and membrane. Neuron. 2012;73(6):1068-81.

[11] Angevine Jr JB. Nervous system, organization of. 2002.

[12] Kevenaar JT, Hoogenraad CC. The axonal cytoskeleton: from organization to function. Frontiers in molecular neuroscience. 2015;8:44.

[13] Prokop A. Cytoskeletal organization of axons in vertebrates and invertebrates. Journal of Cell Biology. 2020;219(7):e201912081.

[14] Hirokawa N. Cross-linker system between neurofilaments, microtubules and membranous organelles in frog axons revealed by the quick-freeze, deep-etching method. Journal of Cell Biology. 1982;94(1):129-42.

[15] Yuan A, Rao MV, Veeranna n, Nixon RA. Neurofilaments at a glance. Journal of cell science. 2012;125(14):3257-63.

[16] Conde C, Cáceres A. Microtubule assembly, organization and dynamics in axons and dendrites. Nature Reviews Neuroscience. 2009;10(5):319-32.

[17] Kapitein LC, Hoogenraad CC. Building the neuronal microtubule cytoskeleton. Neuron. 2015;87(3):492-506.

[18] Letourneau PC. Actin in axons: stable scaffolds and dynamic filaments. Cell Biology of the Axon. 2009:265-90.

[19] Xu K, Zhong G, Zhuang X. Actin, spectrin, and associated proteins form a periodic cytoskeletal structure in axons. Science. 2013;339(6118):452-6.

[20] Leterrier C, Dubey P, Roy S. The nano-architecture of the axonal cytoskeleton. Nature Reviews Neuroscience. 2017;18(12):713-26.

[21] Mehrbod M, Mofrad MR. On the significance of microtubule flexural behavior in cytoskeletal mechanics. PLoS one. 2011;6(10):e25627.

[22] Baas PW. Microtubule stability in the axon: new answers to an old mystery. Neuron. 2013;78(1):3-5.

[23] Baas PW, Rao AN, Matamoros AJ, Leo L. Stability properties of neuronal microtubules. Cytoskeleton. 2016;73(9):442-60.

[24] Tang-Schomer MD, Patel AR, Baas PW, Smith DH. Mechanical breaking of microtubules in axons during dynamic stretch injury underlies delayed elasticity, microtubule disassembly, and axon degeneration. The FASEB Journal. 2010;24(5):1401.

[25] Ding EA, Kumar S. Neurofilament biophysics: From structure to biomechanics. Molecular Biology of the Cell. 2024;35(5):re1.

[26] Kornreich M, Malka-Gibor E, Laser-Azogui A, Doron O, Herrmann H, Beck R. Composite bottlebrush mechanics: α-internexin fine-tunes neurofilament network properties. Soft Matter. 2015;11(29):5839-49.

[27] Al-Chalabi A, Miller CC. Neurofilaments and neurological disease. Bioessays. 2003;25(4):346-55.

[28] Franze K, Guck J. The biophysics of neuronal growth. Reports on Progress in Physics. 2010;73(9):094601.

[29] Gallo G. The Axonal Actin Filament Cytoskeleton: Structure, Function, and Relevance to Injury and Degeneration. Molecular Neurobiology. 2024;61(8):5646-64.

[30] Vassilopoulos S, Gibaud S, Jimenez A, Caillol G, Leterrier C. Ultrastructure of the axonal periodic scaffold reveals a braid-like organization of actin rings. Nature Communications. 2019;10(1):5803.

[31] Dubey S, Bhembre N, Bodas S, Veer S, Ghose A, Callan-Jones A, et al. The axonal actin-spectrin lattice acts as a tension buffering shock absorber. Elife. 2020;9:e51772.

[32] Fan A, Tofangchi A, Kandel M, Popescu G, Saif T. Coupled circumferential and axial tension driven by actin and myosin influences in vivo axon diameter. Scientific reports. 2017;7(1):14188.

[33] Costa AR, Sousa SC, Pinto-Costa R, Mateus JC, Lopes CD, Costa AC, et al. The membrane periodic skeleton is an actomyosin network that regulates axonal diameter and conduction. Elife. 2020;9:e55471.

[34] Ganguly A, Tang Y, Wang L, Ladt K, Loi J, Dargent B, et al. A dynamic formin-dependent deep F-actin network in axons. Journal of Cell Biology. 2015;210(3):401-17.

[35] Ruthel G, Banker G. Actin-dependent anterograde movement of growth-cone-like structures along growing hippocampal axons: A novel form of axonal transport? Cell motility and the cytoskeleton. 1998;40(2):160-73.

[36] Inagaki N, Katsuno H. Actin waves: origin of cell polarization and migration? Trends in cell biology. 2017;27(7):515-26.

[37] Smith DH. Stretch growth of integrated axon tracts: extremes and exploitations. Progress in neurobiology. 2009;89(3):231-9.

[38] Maday S, Twelvetrees AE, Moughamian AJ, Holzbaur EL. Axonal transport: cargo-specific mechanisms of motility and regulation. Neuron. 2014;84(2):292-309.

[39] Howard J. Mechanics of motor proteins. In: Physics of biomolecules and cells. Physique des biomolécules et des cellules: session LXXV. 2–27 July 2001. Springer; 2002. p. 69-94.

[40] Vershinin M, Carter BC, Razafsky DS, King SJ, Gross SP. Multiple-motor based transport and its regulation by Tau. Proceedings of the National Academy of Sciences. 2007;104(1):87-92.

[41] Janke C, Magiera MM. The tubulin code and its role in controlling microtubule properties and functions. Nature Reviews Molecular Cell Biology. 2020;21(6):307-26.

[42] Kapitein LC, Hoogenraad CC. Which way to go? Cytoskeletal organization and polarized transport in neurons. Molecular and Cellular Neuroscience. 2011;46(1):9-20.

[43] Roy S. Seeing the unseen: the hidden world of slow axonal transport. The Neuroscientist. 2014;20(1):71-81.

[44] Arikkath J. Mechanisms of axon polarization in pyramidal neurons. Molecular and Cellular Neuroscience. 2020;107:103522.

[45] Horton AC, Ehlers MD. Neuronal polarity and trafficking. Neuron. 2003;40(2):277-95.

[46] Tahirovic S, Bradke F. Neuronal polarity. Cold Spring Harbor perspectives in biology. 2009;1(3):a001644.

[47] Li R, Gundersen GG. Beyond polymer polarity: how the cytoskeleton builds a polarized cell. Nature reviews Molecular cell biology. 2008;9(11):860-73.

[48] Baas PW, Lin S. Hooks and comets: the story of microtubule polarity orientation in the neuron. Developmental neurobiology. 2011;71(6):403-18.

[49] Rao AN, Patil A, Black MM, Craig EM, Myers KA, Yeung HT, et al. Cytoplasmic dynein transports axonal microtubules in a polarity-sorting manner. Cell reports. 2017;19(11):2210-9.

[50] Rao AN, Baas PW. Polarity sorting of microtubules in the axon. Trends in neurosciences. 2018;41(2):77-88.

[51] Ghose A, Pullarkat P. The role of mechanics in axonal stability and development. In: Seminars in cell & developmental biology. vol. 140. Elsevier; 2023. p. 22-34.

[52] Athamneh AI, He Y, Lamoureux P, Fix L, Suter DM, Miller KE. Neurite elongation is highly correlated with

bulk forward translocation of microtubules. Scientific reports. 2017;7(1):7292.

[53] Baas PW, Ahmad FJ. Force generation by cytoskeletal motor proteins as a regulator of axonal elongation and retraction. Trends in cell biology. 2001;11(6):244-9.

[54] Gallo G, Yee Jr HF, Letourneau PC. Actin turnover is required to prevent axon retraction driven by endogenous actomyosin contractility. The Journal of cell biology. 2002;158(7):1219-28.

[55] Franze K. Integrating chemistry and mechanics: the forces driving axon growth. Annual review of cell and developmental biology. 2020;36(1):61-83.

[56] Bray D. Axonal growth in response to experimentally applied mechanical tension. Developmental biology. 1984;102(2):379-89.

[57] Dennerll T, Joshi H, Steel V, Buxbaum R, Heidemann S. Tension and compression in the cytoskeleton of PC-12 neurites. II: Quantitative measurements. Journal of Cell Biology. 1988;107(2):665-74.

[58] Dennerll TJ, Lamoureux P, Buxbaum RE, Heidemann SR. The cytomechanics of axonal elongation and retraction. Journal of Cell Biology. 1989;109(6):3073-83.

[59] Rajagopalan J, Tofangchi A, Saif MTA. Drosophila neurons actively regulate axonal tension in vivo. Biophysical journal. 2010;99(10):3208-15.

[60] Krieg M, Dunn AR, Goodman MB. Mechanical control of the sense of touch by β-spectrin. Nature cell biology. 2014;16(3):224-33.

[61] Mutalik SP, Joseph J, Pullarkat PA, Ghose A. Cytoskeletal mechanisms of axonal contractility. Biophysical journal. 2018;115(4):713-24.

[62] Fan A, Joy MSH, Saif T. A connected cytoskeleton network generates axonal tension in embryonic Drosophila. Lab on a Chip. 2019;19(18):3133-9.

[63] Bernal R, Pullarkat PA, Melo F. Mechanical properties of axons. Physical review letters. 2007;99(1):018301.

[64] Bernal R, Melo F, Pullarkat PA. Drag force as a tool to test the active mechanical response of PC12 neurites. Biophysical journal. 2010;98(4):515-23.

[65] O'Toole M, Lamoureux P, Miller KE. A physical model of axonal elongation: force, viscosity, and adhesions govern the mode of outgrowth. Biophysical journal. 2008;94(7):2610-20.

[66] O'Toole M, Lamoureux P, Miller KE. Measurement of subcellular force generation in neurons. Biophysical journal. 2015;108(5):1027-37.

[67] Deepak J, Anirudh R, Sundar SS. Applications of lasers in industries and laser welding: A review. Materials Today: Proceedings. 2023.

[68] Addanki S, Amiri IS, Yupapin P. Review of optical fibers-introduction and applications in fiber lasers. Results in Physics. 2018;10:743-50.

[69] Legres LG, Chamot C, Varna M, Janin A. The laser technology: new trends in biology and medicine. Journal of Modern Physics. 2014;5(5):267-79.

[70] Azadgoli B, Baker RY. Laser applications in surgery. Annals of translational medicine. 2016;4(23):452.

[71] Beard P. Biomedical photoacoustic imaging. Interface focus. 2011;1(4):602-31.

[72] Lenton IC, Scott EK, Rubinsztein-Dunlop H, Favre-Bulle IA. Optical tweezers exploring neuroscience. Frontiers in Bioengineering and Biotechnology. 2020;8:602797.

[73] Hu L, Zhang X, Miller P, Ozkan M, Ozkan C, Wang J. Cell adhesion measurement by laser-induced stress waves. Journal of Applied Physics. 2006;100(8).

[74] Sada T, Fujigaya T, Niidome Y, Nakazawa K, Nakashima N. Near-IR laser-triggered target cell collection using a carbon nanotube-based cell-cultured substrate. ACS nano. 2011;5(6):4414-21.

[75] Kumar S, Maxwell IZ, Heisterkamp A, Polte TR, Lele TP, Salanga M, et al. Viscoelastic retraction of single living stress fibers and its impact on cell shape, cytoskeletal organization, and extracellular matrix mechanics. Biophysical journal. 2006;90(10):3762-73.

[76] Kunik D, Dion C, Ozaki T, Levin LA, Costantino S. Laser-based single-axon transection for high-content axon injury and regeneration studies. PLoS One. 2011;6(11):e26832.

[77] Rauzi M, Verant P, Lecuit T, Lenne PF. Nature and anisotropy of cortical forces orienting Drosophila tissue morphogenesis. Nature cell biology. 2008;10(12):1401-10.

[78] Yanik MF, Cinar H, Cinar HN, Chisholm AD, Jin Y, Ben-Yakar A. Functional regeneration after laser axotomy. Nature. 2004;432(7019):822-2.

[79] Vogel A, Venugopalan V. Mechanisms of pulsed laser ablation of biological tissues. Chemical reviews. 2003;103(2):577-644.

[80] Niemz MH, et al. Laser-tissue interactions. vol. 322. Springer; 2007.

[81] Lin Z, Hong M. Femtosecond laser precision engineering: from micron, submicron, to nanoscale. Ultrafast Science. 2021.

[82] Mehta D, Pullarkat P. Investigation of Axonal Beading Induced by Photo-oxidation. bioRxiv. 2025:2025-02.

[83] Tang J, Bai Z, Zhang D, Qi Y, Ding J, Wang Y, et al. Advances in all-solid-state passively Q-switched lasers based on Cr4+: YAG saturable absorber. In: Photonics. vol. 8. Multidisciplinary Digital Publishing Institute; 2021. p. 93.

[84] Koechner W. Solid-state laser engineering. vol. 1. springer; 2013.

[85] Svelto O, Hanna DC, et al. Principles of lasers. vol. 1. Springer; 2010.

[86] Sankar P, Philip R. Nonlinear optical properties of nanomaterials. In: Characterization of nanomaterials. Elsevier; 2018. p. 301-34.

[87] Powers PE, Haus JW. Fundamentals of nonlinear optics. CRC press; 2017.

[88] Hutson MS, Tokutake Y, Chang MS, Bloor JW, Venakides S, Kiehart DP, et al. Forces for morphogenesis investigated with laser microsurgery and quantitative modeling. Science. 2003;300(5616):145-9.

[89] Fernandez-Gonzalez R, de Matos Simoes S, Röper JC, Eaton S, Zallen JA. Myosin II dynamics are regulated by tension in intercalating cells. Developmental cell. 2009;17(5):736-43.

[90] Khodjakov A, Cole RW, McEwen BF, Buttle KF, Rieder CL. Chromosome fragments possessing only one kinetochore can

congress to the spindle equator. Journal of Cell Biology. 1997;136(2):229-40.

[91] Saha A, Nishikawa M, Behrndt M, Heisenberg CP, Jülicher F, Grill SW. Determining physical properties of the cell cortex. Biophysical journal. 2016;110(6):1421-9.

[92] Botvinick E, Venugopalan V, Shah J, Liaw L, Berns M. Controlled ablation of microtubules using a picosecond laser. Biophysical journal. 2004;87(6):4203-12.

[93] Bird MM. Microsurgical transection of small nerve fibre bundles in vitro: Effects on axons, growth cones and glial cells. Cell and Tissue Research. 1978;190:525-38.

[94] Kerschensteiner M, Schwab ME, Lichtman JW, Misgeld T. In vivo imaging of axonal degeneration and regeneration in the injured spinal cord. Nature medicine. 2005;11(5):572-7.

[95] Shao X, Sørensen MH, Xia X, Fang C, Hui TH, Chang RCC, et al. Beading of injured axons driven by tension-and adhesion-regulated membrane shape instability. Journal of the Royal Society Interface. 2020;17(168):20200331.

[96] Franze K, Gerdelmann J, Weick M, Betz T, Pawlizak S, Lakadamyali M, et al. Neurite branch retraction is caused by a threshold-dependent mechanical impact. Biophysical journal. 2009;97(7):1883-90.

[97] He Y, Yu W, Baas PW. Microtubule reconfiguration during axonal retraction induced by nitric oxide. Journal of Neuroscience. 2002;22(14):5982-91.

[98] Qu Y, Hahn I, Webb SE, Pearce SP, Prokop A. Periodic actin structures in neuronal axons are required to maintain microtubules. Molecular biology of the cell. 2017;28(2):296-308.

[99] Datar A, Ameeramja J, Bhat A, Srivastava R, Mishra A, Bernal R, et al. The roles of microtubules and membrane tension in axonal beading, retraction, and atrophy. Biophysical journal. 2019;117(5):880-91.

[100] Pannese E, Ledda M, Arcidiacono G, Rigamonti L, Procacci P. A comparison of the density of microtubules in the central and peripheral axonal branches of the pseudounipolar neurons of lizard spinal ganglia. The Anatomical Record. 1984;208(4):595-605.

[101] Aydın MŞ, Bay S, Yiğit EN, Özgül C, Oğuz EK, Konuk EY, et al. Active shrinkage protects neurons following axonal transection. Iscience. 2023;26(10).

[102] Tymanskyj SR, Ma L. MAP7 prevents axonal branch retraction by creating a stable microtubule boundary to rescue polymerization. Journal of Neuroscience. 2019;39(36):7118-31.

[103] Li Y, Black MM. Microtubule assembly and turnover in growing axons. The Journal of neuroscience. 1996;16(2):531.

[104] Gomez TM, Letourneau PC. Actin dynamics in growth cone motility and navigation. Journal of neurochemistry. 2014;129(2):221-34.

[105] Schelski M, Bradke F. Microtubule retrograde flow retains neuronal polarization in a fluctuating state. Science advances. 2022;8(44):eabo2336.

[106] Berridge MJ. Neuronal calcium signaling. Neuron. 1998;21(1):13-26.

[107] Wayman GA, Lee YS, Tokumitsu H, Silva A, Soderling TR. Calmodulin-kinases: modulators of neuronal development and plasticity. Neuron. 2008;59(6):914-31.

[108] Berridge MJ, Bootman MD, Roderick HL. Calcium signalling: dynamics, homeostasis and remodelling. Nature reviews Molecular cell biology. 2003;4(7):517-29.

[109] Clapham DE. Calcium signaling. Cell. 2007;131(6):1047-58.

[110] Brini M, Calì T, Ottolini D, Carafoli E. Neuronal calcium signaling: function and dysfunction. Cellular and molecular life sciences. 2014;71:2787-814.

[111] Burnashev N. Calcium permeability of ligand-gated channels. Cell calcium. 1998;24(5-6):325-32.

[112] Simms BA, Zamponi GW. Neuronal voltage-gated calcium channels: structure, function, and dysfunction. Neuron. 2014;82(1):24-45.

[113] Prakriya M, Lewis RS. Store-operated calcium channels. Physiological reviews. 2015.

[114] Vangeel L, Voets T. Transient receptor potential channels and calcium signaling. Cold Spring Harbor perspectives in biology. 2019;11(6):a035048.

[115] Bagur R, Hajnóczky G. Intracellular Ca2+ sensing: its role in calcium homeostasis and signaling. Molecular cell. 2017;66(6):780-8.

[116] Ranade SS, Syeda R, Patapoutian A. Mechanically activated ion channels. Neuron. 2015;87(6):1162-79.

[117] Coste B, Mathur J, Schmidt M, Earley TJ, Ranade S, Petrus MJ, et al. Piezo1 and Piezo2 are essential components of distinct mechanically activated cation channels. Science. 2010;330(6000):55-60.

[118] Wu J, Lewis AH, Grandl J. Touch, tension, and transduction–the function and regulation of Piezo ion channels. Trends in biochemical sciences. 2017;42(1):57-71.

[119] Bhattacharya MR, Bautista DM, Wu K, Haeberle H, Lumpkin EA, Julius D. Radial stretch reveals distinct populations of mechanosensitive mammalian somatosensory neurons. Proceedings of the National Academy of Sciences. 2008;105(50):20015-20.

[120] Poole K, Herget R, Lapatsina L, Ngo HD, Lewin GR. Tuning Piezo ion channels to detect molecular-scale movements relevant for fine touch. Nature communications. 2014;5(1):3520.

[121] Rodat-Despoix L, Hao J, Dandonneau M, Delmas P. Shear stress-induced Ca2+ mobilization in MDCK cells is ATP dependent, no matter the primary cilium. Cell calcium. 2013;53(5-6):327-37.

[122] Cahalan SM, Lukacs V, Ranade SS, Chien S, Bandell M, Patapoutian A. Piezo1 links mechanical forces to red blood cell volume. elife. 2015;4:e07370.

[123] Young M, Lewis AH, Grandl J. Physics of mechanotransduction by Piezo ion channels. Journal of General Physiology. 2022;154(7):e202113044.

[124] Verkhratsky A. Physiology and pathophysiology of the calcium store in the endoplasmic reticulum of neurons. Physiological reviews. 2005;85(1):201-79.

[125] Pivovarova NB, Andrews SB. Calcium-dependent mitochondrial function and dysfunction in neurons. The FEBS journal. 2010;277(18):3622-36.

[126] Walters GC, Usachev YM. Mitochondrial calcium cycling in neuronal function and neurodegeneration. Frontiers in cell and developmental biology. 2023;11:1094356.

[127] Verkhratsky AJ, Petersen OH. Neuronal calcium stores. Cell calcium. 1998;24(5-6):333-43.

[128] Narita K, Akita T, Hachisuka J, Huang SM, Ochi K, Kuba K. Functional coupling of Ca2+ channels to ryanodine receptors at presynaptic terminalsamplification of exocytosis and plasticity. Journal of General Physiology. 2000;115(4):519-32.

[129] Bezprozvanny l, Watras J, Ehrlich BE. Bell-shaped calcium-response curves of lns (l, 4, 5) P3-and calcium-gated channels from endoplasmic reticulum of cerebellum. Nature. 1991;351(6329):751-4.

[130] Taylor CW, Tovey SC. IP3 receptors: toward understanding their activation. Cold Spring Harbor perspectives in biology. 2010;2(12):a004010.

[131] Yang J, McBride S, Mak DOD, Vardi N, Palczewski K, Haeseleer F, et al. Identification of a family of calcium sensors as protein ligands of inositol trisphosphate receptor Ca2+ release channels. Proceedings of the National Academy of Sciences. 2002;99(11):7711-6.

[132] Bootman MD, Bultynck G. Fundamentals of cellular calcium signaling: a primer. Cold Spring Harbor perspectives in biology. 2020;12(1):a038802.

[133] Leybaert L, Sanderson MJ. Intercellular Ca2+ waves: mechanisms and function. Physiological reviews. 2012;92(3):1359-92.

[134] Thul R, Smith G, Coombes S. A bidomain threshold model of propagating calcium waves. Journal of mathematical biology. 2008;56:435-63.

[135] Wang JT, Medress ZA, Barres BA. Axon degeneration: molecular mechanisms of a self-destruction pathway. Journal of Cell Biology. 2012;196(1):7-18.

[136] Artal-Sanz M, Tavernarakis N. Proteolytic mechanisms in necrotic cell death and neurodegeneration. FEBS letters. 2005;579(15):3287-96.

[137] Vosler P, Brennan C, Chen J. Calpain-mediated signaling mechanisms in neuronal injury and neurodegeneration. Molecular neurobiology. 2008;38(1):78-100.

[138] Saatman KE, Creed J, Raghupathi R. Calpain as a therapeutic target in traumatic brain injury. Neurotherapeutics. 2010;7:31-42.

[139] Wang KK. Calpain and caspase: can you tell the difference? Trends in neurosciences. 2000;23(1):20-6.

[140] Ma M. Role of calpains in the injury-induced dysfunction and degeneration of the mammalian axon. Neurobiology of disease. 2013;60:61-79.

[141] Billger M, Wallin M, Karlsson JO. Proteolysis of tubulin and microtubule-associated proteins 1 and 2 by calpain I and II.

Difference in sensitivity of assembled and disassembled microtubules. Cell calcium. 1988;9(1):33-44.

[142] Kamakura K, Ishiura S, Sugita H, Toyokura Y. Identification of Ca2+-activated neutral protease in the peripheral nerve and its effects on neurofilament degeneration. Journal of Neurochemistry. 1983;40(4):908-13.

[143] Kamakura K, Ishiura S, Suzuki K, Sugita H, Toyokura Y. Calcium-Activated neutral protease in the peripheral nerve, which requires μM order Ca2+, and its effect on the neurofilament triplet. Journal of neuroscience research. 1985;13(3):391-403.

[144] Schlaepfer W, Lee C, Lee VY, Zimmerman UJ. An immunoblot study of neurofilament degradation in situ and during calcium-activated proteolysis. Journal of neurochemistry. 1985;44(2):502-9.

[145] Hahn K, DeBiasio R, Taylor DL. Patterns of elevated free calcium and calmodulin activation in living cells. Nature. 1992;359(6397):736-8.

[146] Seubert P, Baudry M, Dudek S, Lynch G. Calmodulin stimulates the degradation of brain spectrin by calpain. Synapse. 1987;1(1):20-4.

[147] Weisenberg RC, Deery WJ. The mechanism of calcium-induced microtubule disassembly. Biochemical and biophysical research communications. 1981;102(3):924-31.

[148] Schliwa M, Euteneuer U, Bulinski JC, Izant JG. Calcium lability of cytoplasmic microtubules and its modulation by microtubule-associated proteins. Proceedings of the National Academy of Sciences. 1981;78(2):1037-41.

[149] Davis MA, Fairgrieve MR, Den Hartigh A, Yakovenko O, Duvvuri B, Lood C, et al. Calpain drives pyroptotic vimentin cleavage, intermediate filament loss, and cell rupture that mediates immunostimulation. Proceedings of the National Academy of Sciences. 2019;116(11):5061-70.

[150] Pchitskaya E, Popugaeva E, Bezprozvanny I. Calcium signaling and molecular mechanisms underlying neurodegenerative diseases. Cell calcium. 2018;70:87-94.

[151] Ziv NE, Spira ME. Axotomy induces a transient and localized elevation of the free intracellular calcium concentration to the millimolar range. Journal of neurophysiology. 1995;74(6):2625-37.

[152] Wolf JA, Stys PK, Lusardi T, Meaney D, Smith DH. Traumatic axonal injury induces calcium influx modulated by tetrodotoxin-sensitive sodium channels. Journal of Neuroscience. 2001;21(6):1923-30.

[153] Villegas R, Martinez NW, Lillo J, Pihan P, Hernandez D, Twiss JL, et al. Calcium release from intra-axonal endoplasmic reticulum leads to axon degeneration through mitochondrial dysfunction. Journal of Neuroscience. 2014;34(21):7179-89.

[154] Stys PK. General mechanisms of axonal damage and its prevention. Journal of the neurological sciences. 2005;233(1-2):3-13.

[155] Stirling DP, Stys PK. Mechanisms of axonal injury: internodal nanocomplexes and calcium deregulation. Trends in molecular medicine. 2010;16(4):160-70.

[156] LoPachin Jr RM, LoPachin VR, Saubermann AJ. Effects of axotomy on distribution and concentration of elements in rat sciatic nerve. Journal of neurochemistry. 1990;54(1):320-32.

[157] Ziv NE, Spira ME. Spatiotemporal distribution of Ca2+ following axotomy and throughout the recovery process of cultured Aplysia neurons. European Journal of Neuroscience. 1993;5(6):657-68.

[158] Waxman SG, Black JA, Ransom BR, Stys PK. Anoxic injury of rat optic nerve: ultrastructural evidence for coupling between Na+ influx and Ca2+-mediated injury in myelinated CNS axons. Brain research. 1994;644(2):197-204.

[159] Wendt ER, Ferry H, Greaves DR, Keshav S. Ratiometric analysis of fura red by flow cytometry: a technique for monitoring intracellular calcium flux in primary cell subsets. PloS one. 2015;10(4):e0119532.

[160] Betzenhauser MJ, Marks AR. Ryanodine receptor channelopathies. Pflügers Archiv-European Journal of Physiology. 2010;460:467-80.

[161] Zhong G, He J, Zhou R, Lorenzo D, Babcock HP, Bennett V, et al. Developmental mechanism of the periodic membrane skeleton in axons. Elife. 2014;3:e04581.

[162] Stocca G, Schmidt-Hieber C, Bischofberger J. Differential dendritic Ca2+ signalling in young and mature hippocampal granule cells. Wiley Online Library; 2008.

[163] Fierro L, DiPolo R, Llano I. Intracellular calcium clearance in Purkinje cell somata from rat cerebellar slices. The Journal of physiology. 1998;510(2):499-512.

[164] Baas PW, Black MM. Individual microtubules in the axon consist of domains that differ in both composition and stability. Journal of Cell Biology. 1990;111(2):495-509.

[165] Katrukha EA, Jurriens D, Pastene DMS, Kapitein LC. Quantitative mapping of dense microtubule arrays in mammalian neurons. Elife. 2021;10:e67925.

[166] Guha S, Patil A, Muralidharan H, Baas PW. Mini-review: Microtubule sliding in neurons. Neuroscience letters. 2021;753:135867.

[167] Goodson HV, Jonasson EM. Microtubules and microtubule-associated proteins. Cold Spring Harbor perspectives in biology. 2018;10(6):a022608.

[168] Fischer I, Romano-Clarke G, Grynspan F. Calpain-mediated proteolysis of microtubule associated proteins MAP1B and

MAP2 in developing brain. Neurochemical research. 1991;16:891-8.

[169] Hellal F, Hurtado A, Ruschel J, Flynn KC, Laskowski CJ, Umlauf M, et al. Microtubule stabilization reduces scarring and causes axon regeneration after spinal cord injury. Science. 2011;331(6019):928-31.

[170] Charras GT, Hu CK, Coughlin M, Mitchison TJ. Reassembly of contractile actin cortex in cell blebs. The Journal of cell biology. 2006;175(3):477-90.